Micro-Computed Tomography Assessment of Skeletal Structure in a Mucopolysaccharidosis IX Mouse Model

By

Ramya Vinith

A thesis submitted to the Faculty of Graduate Studies of
The University of Manitoba
in partial fulfilment of the requirements for the degree of

MASTER OF SCIENCE

Department of Biochemistry and Medical Genetics
Faculty of Health Science
University of Manitoba
Winnipeg

Abstract

Mucopolysaccharidosis (MPS) IX is a lysosomal storage disorder caused by a deficiency of hyaluronidase 1 (HYAL1). With few patients described, to extend our understanding of the skeletal phenotype in MPS IX, we performed micro-computed tomography on HYAL1 knockout (*Hyal1*$^{-/-}$) and control mice at 6 months and 1 year of age. Images were examined for changes in the bone shape, microarchitecture, and density. No abnormalities in the shape of the bones of *Hyal1*$^{-/-}$ mice were detected. However, images of the distal femur of the knee joint showed abnormal periosteal bone in male *Hyal1*$^{-/-}$ mice. This was also complemented by a significant increase in the periosteal perimeter and periosteal volume. The density of the trabecular and cortical bone did not differ significantly between the two groups. Periosteal bone formation is a pathology shared with other MPSs and indicates that this model may be valuable in understanding the skeletal manifestations of all MPSs.

Acknowledgements

First and foremost, I would like to thank my supervisor, Dr. Barbara Triggs-Raine for giving me the opportunity to work in her lab. Dr. Triggs-Raine is the best teacher I have ever come across who has inspired me in every sense during my Master's program. She has guided me not only in research but also taught me how to stay positive, motivated and give my best towards everything. I cannot thank her enough for the time and guidance she has given me while writing my thesis for which I am very grateful. I consider myself extremely lucky to have worked in her lab. I will carry all the skills and virtues I have acquired in my future endeavours.

I would like to take this opportunity to thank my committee members. A big thanks to my internal committee member, Dr. Mark Nachtigal for all his advice and feedback. Thank you very much for all the valuable discussions related to my thesis project. Those discussions have always encouraged me to read more on the topics I would have missed otherwise. My gratitude and appreciation goes to the external examiner Dr. Jason Peeler, for agreeing to be in my committee at a short notice. I also thank my previous external committee member, Dr. Virginie Pollet for all her feedbacks.

I want to thank Dr. Mike Jackson, the co-ordinator of the imaging facility. I am really grateful for all his help with the micro-CT scanning and analysis, and training.

Next, I would like to take the opportunity to thank each member of my lab, past and present, including Dr. Rick Hemming, Dr. Joy Armistead, Biswajit Chowdhury and Naderah Altaleb. I would like to thank Rick for all his help in handling and dissection of mice and for his training on various techniques, especially PCR and DNA isolation. I really appreciate the minute technical details that he would tell me while training. I would like to thank Joy for all her feedback and troubleshooting advices that she has provided on various occasions. I would like to

thank Jit for all his help and suggestions especially for histological experiments. Lastly, I want to thank Naderah for the friendship that we share.

Next I want to thank my family, my dad, Mr. P. K. Venugopal and my mom, Mrs. Rani Venugopal for all the foundation that they have provided me. It is their unconditional love, support and appreciation that had always kept me going. I also want to thank my sister, Divya Venugopal who fills me with immense energy and spirit each time I talk to her. I cannot forget our weekend talks that would recharge me for the rest of the week. I would also like to show my gratitude towards my parents-in-law, Mr. Yathindranath Narayanan and Mrs. Jalaja Yathindranath for all the support and happiness they have shown even on my small accomplishments.

Lastly, I would like to thank my husband, Dr. Vinith Yathindranath for all his love and support throughout my studies. He has been an honest critic and has always pushed me to do my best. He has helped me to realize my full potential whenever I fail to see. He has instilled in me the quality of exploring the science behind everything. Finally, I greatly appreciate Vinith's help in formatting my thesis.

Dedicated to my husband, Vinith

Contents

List of Tables

List of Figures

Figure 2.2: Image processing. Panel A: Image reconstruction, shows the image of the knee joint reconstructed using NRecon software. Panel B: Region of interest (ROI) and volume of interest (VOI) selection, the left image is an 8 bit grayscale view of the knee joint obtained after reconstruction of TIFF images. The top image on the right side highlights the ROI for cortical bone from the femoral diaphysis defined in the CTAnalyser software using the ROI tool. A set of ROIs from several consecutive cross sections were used to make a VOI for cortical bones from which measurements were made. The middle image on the right side highlights the ROI for trabecular bone from the femoral metaphysis defined by the CTAnalyser software using ROI tool. A set of ROIs from several consecutive cross sections were used to make a VOI for trabecular bones from which measurements were made. The bottom image on the right side shows the cross section of growth plate, which was considered as a reference point for defining metaphysis and diaphysis in order to select VOIs for trabecular and cortical bone respectively. Panel C: Segmentation, shows the segmented cortical image with mineralized bone in white and non-mineralized bone in black. 2-54

Figure 3.1. **Representative 3-D images of the skeleton of a Hyal1$^{-/-}$ and Hyal1$^{+/+}$ male mouse:** Images of the mouse skeleton were obtained by micro-CT scanning at 35 µm resolution, and reconstructed using NRecon software. CTVox software was used to generate the colour-coded 3-D reconstruction. Colour-coding was chosen to provide a clear view of any outgrowths, if present. Comparison between Hyal1$^{-/-}$ and Hyal1$^{+/+}$ mice: (A) A ventral view of the whole mouse skeleton (B) A dorsal view of the skull (C) A dorsal view of the spine showing the odontoid process. (D) A ventral view of the pelvis including the hip joint and (E) A ventral view of the ribs. (F) An anterior view of the hind

limb showing tarsals (Ta), metatarsals (MT) and phalangeal (Ph) joints. (G) An anterior view of the paw indicating carpal and metacarpal joints. (H) A dorsal view of elbow joint. (I) A ventral view of spine. Arrows indicate features that were examined and compared in these images of Hyal1$^{+/+}$ and Hyal1$^{-/-}$ mice, S= Skull, O= Odontoid process, Z= zygomatic arches, R= Ribcage, R'= Ribs, C= Clavicles, S'= Spine, H= Hip, P'= Pelvis, F= Femur, T= Tibia, P=Paws, F'= Feet, E = Elbow, Ta= Tarsals, MT= Metatarsals, Ph= Phalanges, C= Carpals, MC= Metacarpals. No obvious abnormality was seen in the structure and shape of the bones in the Hyal1$^{-/-}$ mice compared to controls. This is a representative image of 5 pairs of male mice aging both 6 months (n=2) and 1 year (n=3). These images are not to scale. 3-66

Figure 3.2. Representative 3-D grayscale images of the skeleton of a Hyal1$^{-/-}$ and Hyal1$^{+/+}$ mouse: Images of the mouse skeleton were obtained from micro-CT scanning at 35 µm resolution, reconstructed using NRecon software, and manipulated in CTVox software to generate the 8 bit grayscale 3-D image**.** The darkest shade is black, which has a value of 0 and represents total transmission of X-rays obtained from soft tissues. The lightest shade is white, with a value of 255, and represents total absorption obtained from dense tissues like bone. Comparison between Hyal1$^{-/-}$ and Hyal1$^{+/+}$ (A) A ventral view of the whole mouse skeleton, (B) A ventral view of the skull, (C) A ventral view of the ribs, (D) A dorsal view of the spine (E) A ventral view of the pelvis including hip joint, (E) A dorsal view of the feet and (F) A dorsal view of the spine. Arrows indicate features that were examined in these images S= Radiodensity of skull, Z= Thickness of zygomatic arches, R= Thickness of ribcage, C= Thickness of clavicles, S'= Spinal sclerosis, H= Hip sclerosis, F= Thickness and sclerosis of the femur, T= Thickness and sclerosis of the

Figure 3.6. Representative high resolution colour-coded 3-D images of the skeleton of 1 year old female Hyal1$^{-/-}$ and Hyal1$^{+/+}$ control mice: Images of the mouse skeleton were obtained from micro-CT scanning at 9 µm resolution and reconstructed using NRecon software, followed by CTVox software to generate the colour-coded 3-D reconstruction. Colour-coding was selected to provide clear view of any outgrowths, if present. Comparison between Hyal1$^{-/-}$ and Hyal1$^{+/+}$ controls mice: **(**A) A dorsal view of the skull. (B) A dorsal view of the cervical vertebrae (odontoid process). (C) A ventral view of the ribcage. (D) An anterior view of the hind feet showing tarsals (T), metatarsals (MT) and phalanges (P). (E) A ventral view of pelvis showing hip joint (H). Arrows indicate features that were examined in these images. High resolution scans of different joints didn't show any abnormalities in the Hyal1$^{-/-}$ mice compared to controls. Z= Zygomatic arches, O= Odontoid process, H= Hip, Ta=Tarsal joints, MT=Metatarsals, P=Phalanges. These are representative of 3 sets of mice. Images are not to scale……. 3-79

Figure 3.7. Representative high resolution colour-coded 3-D micro-CT images of different joints of a 6 weeks old female Hyal1$^{-/-}$ and Hyal1$^{+/+}$ mouse: Images of the mouse skeleton were obtained from micro-CT scanning at 9 µm resolution and reconstructed using NRecon software, followed by manipulation using CTVox software to generate the colour-coded 3-D reconstruction. Colour-coding was chosen to provide clear view of any outgrowths, if present. Comparison between Hyal1$^{-/-}$ and Hyal1$^{+/+}$: **(**A) A ventral view of the knee joint at midway fexion. (B) A lateral view of the knee joint at midway flexion. (C) A ventral view of the pelvis including hip joint. (D) An anterior view of the hind paw showing tarsal and metatarsal joint. (E) An anterior view of the fore limb showing carpal and metacarpal joint. (F) An anterior view of elbow joint (G) A

comparison in the endosteal perimeter between Hyal1$^{-/-}$ and controls. Panel D shows comparison in the endosteal volume of Hyal1$^{-/-}$ compared to controls. Panel E shows a comparison in the cortical thickness of Hyal1$^{-/-}$ and controls. Panel F shows a red bar in the diaphysis region of the knee joint indicates the region from which measurements were made. Panel G highlights the region of interest (ROI) for cortical bone from the femoral diaphysis defined by the CTAnalyser software ROI tool. A set of ROIs from several consecutive cross sections were used to make a volume of interest (VOI) for cortical bones from which morphometric parameters were measured. Bar graphs show mean±SD (Error bars= SD), *p < 0.05 between Hyal1$^{-/-}$ and control mice. (n = 6). Abbrevations: Pe.Pm, Periosteal perimeter; Pe.V, Periosteal volume; En.Pm, Endosteal perimeter; En.V, Endosteal volume; Cr.Th, Cortical thickness. Please note that both female and male mice were included in this calculation..... 4-105

Figure 4.7. Comparison of morphometric parameters of trabecular bone in Hyal1$^{-/-}$ mice and controls (Hyal1$^{+/-}$ or Hyal1$^{+/-}$) at one year of age: Micro-CT images from high resolution scans were analyzed in CTAn as described in 2.4.3 from the metaphysis of femur**.** Panel A shows a comparison of trabecular thickness. Panel B shows a comparison of trabecular number. Panel C shows a comparison of trabecular separation. Panel D shows comparison of trabecular pattern factor. Panel E shows a comparison of bone volume fraction. Panel F shows a comparison of connectivity density. Panel G shows a red bar in the metaphysis region of the femur indicating the area from where all the trabecular measurements were made. Panel H highlights the region of interest (ROI) for trabecular bone from the femoral metaphysis defined by the CTAnalyser software ROI tool. Bar graphs show mean±SD (Error bars= SD), *p < 0.05 between Hyal1$^{-/-}$ and

List of Symbols & Abbreviations

α	alpha
β	beta
%	percent
©	copyright
bp	basepairs
°C	degree Celsius
g'	relative centrifugal force
g	gram
kV	kilovolts
M	molar
mM	millimolar
mm	millimeter
min	minutes
ml	milliliter
nm	nanometer
ng	nanogram
rpm	revolutions per minute
sec	seconds
V	volts
µg	microgram
µl	microliter
µm	micrometer
2-D	2-dimension
3-D	3-dimension
ALP	alkaline phosphatase
BBB	blood brain barrier
BMD	bone mineral density
BMP	bitmap
BV/TV	bone volume/tissue volume
CaHA	calcium hydroxyapatite
CD14	cluster of differentiation
Conn.D	connectivity density
CRP	C-reactive protein
CS	chondroitin sulphate
CTS	carpel tunnel syndrome
CT	computed tomography
Ct.Th	cortical thickness
CXCR4	C-X-C chemokine receptor-4
dATP	2’- deoxyadenosine 5’- triphosphate

dCTP	2’- deoxycytidine 5’- triphosphate
dGTP	2’- deoxyguanosine 5’- triphosphate
DNA	deoxyribonucleic acid
dNTP	2’- deoxyribonucleotide 5’- triphosphate
DS	dermatan sulphate
dTTP	2’- deoxythymidine 5’- triphosphate
ECM	extracellular matrix
EDTA	ethylenediamine tetraacetic acid
En.Pm	endosteal perimeter
En.V	endosteal volume
ERT	enzyme replacement therapy
ESR	erythrocyte sedimentation rate
FDA	food and drug administration
GAG	glycosaminoglycans
GlcA	D-glucuronic acid
GlcNAc	N-acetyl-D-glucosamine
GM2	ganglioside monosialic-2
GPI	glycosylphosphatidylinositol
HA	hyaluronan
HABP	hyaluronan binding protein
HARE	hyaluronan receptor for endocytosis
HAS	hyaluronan synthase
HEX	hexosaminidase
HS	heparin sulphate
HSCT	hematopoietic stem cell therapy
Hyal	hyaluronidase
IL	interleukin
JIA	juvenile idiopathic arthritis
KO	knockout
KS	keratan sulphate
LBP	lipopolysaccharide binding protein
LPS	lipopolysaccharide
LSD	lysosomal storage disorder
LVYE	lymphatic vessel endothelial receptor
MCP	metacarpophalangeal
$MgCl_2$	magnesium chloride
MMP	matrix metalloproteinase
MMP9	matrix metalloproteinase 9
MPS	mucopolysaccharidosis
M6P	mannose-6-phosphate receptor
MyD88	myeloid differentiation primary response protein-88
NaCl	sodium chloride
Neo	neomycin resistance cassette
NO	nitric oxide
NSAID	non-steroidal anti-inflammatory drug
OMIM	online Mendelian inheritance of man
PBS	phosphate buffered saline
PCR	polymerase chain reaction
Pe.Pm	periosteal perimeter
Pe.V	periosteal volume
PG	proteoglycan

PIP	proximal interphalangeal
PLP	paraformaldehyde lysine periodate
PTH	parathyroid hormone
RA	rheumatic arthritis
rhASB	recombinant human N-acetyl-galactosamine-4-sulphatase
rhIDUA	recombinant human alpha-L-iduronidase
rhI2S	recombinant human-2-sulphatase
ROI	region of interest
SD	standard deviation
SDS	sodium dodecyl sulphate
SPAM	sperm adhesion molecule
TAE	tris acetate EDTA
Tb.N	trabecular number
Tb.Pf	trabecular pattern factor
Tb.Sp	trabecular separation
Tb.Th	trabecular thickness
TIFF	tagged image file format
TKO	triple knockout
TLR4	toll like receptor-4
TMD	tissue mineral density
TNF	tumor necrosis factor
TRAP	tartrate-resistant acid phosphatase
Tris	2-amino-2-hydroxymethyl-propane-1,3-diol
VOI	volume of interest
WT	wild type

List of Appendices

Chapter 1

Introduction

1.1 Lysosomal storage disorders (LSDs)

Lysosomes are intracellular organelles containing hydrolytic enzymes that can degrade macromolecules like proteins, carbohydrates, lipids and nucleic acids, thus acting as the digestive body of the cell. Mutations in genes encoding these catabolic enzymes often lead to their deficiency, or defects in the function of another lysosomal protein, causing an accumulation of partially or undegraded macromolecules in lysosomes. This accumulation eventually leads to dysfunction of the cell, resulting in a lysosomal storage disorder (LSD) [1,2,3].

LSDs are rare genetic disorders having a prevalence between 1 in 7100 to 7700 live births[2]. They are highly heterogeneous and the organ(s) which is most affected depends upon the nature of the macromolecule which accumulates, its cellular location, tissue distribution, and turnover rate in specific tissues. More accumulation is found in tissues where the substrate is abundant. The organs frequently affected in LSDs are the brain, heart, eye, muscle, bone, joint and the reticuloendothelial system (involving bone marrow, spleen and blood vessels). The symptoms of LSDs range from mild to severe, and patients with mild symptoms are often undiagnosed, misdiagnosed or their diagnosis is delayed, leading to significant morbidity. Rheumatic features are the most common symptoms of the attenuated subtypes while severe forms display progressive multiple organ dysfunction. Some examples of LSDs with significant musculoskeletal symptoms are the MPSs (mucopolysaccharidoses), Fabry disease, Gaucher disease, mucolipidosis and Pompe disease (sphingolipidoses) [2, 3].

1.2 Mucopolysaccharidoses (MPSs)

1.2.1 Introduction

The mucopolysaccharidoses (MPSs) are rare genetic disorders caused by deficiencies of specific lysosomal enzymes required for the degradation of glycosaminoglycans (GAGs) or mucopolysaccharides [4]. They are characterized by the accumulation of specific GAGs in cellular lysosomes, and reach their highest levels in tissues where the GAG is most abundant, resulting in cell, tissue or organ dysfunction. So far, seven different types of MPSs (I, II, III, IV, VI, VII and IX) have been clinically differentiated, and are caused by deficiency of eleven different enzymes, each inherited in an autosomal recessive manner except MPS II which follows X-linked recessive inheritance [2, 3]. The major types of MPSs are summarized in Table 1.1 [2–5]**.** Together, these disorders have an incidence of 1 in 22,000 live births representing 35% of all LSDs [2].

The clinical manifestations are progressive, heterogeneous and multisystemic involving visceral, skeletal and sometimes even neurological systems. Some of the common clinical symptoms are described in the Table 1.2 [2–5].

Table 1.1. Types of Mucopolysaccharidoses (MPS)

Type	Eponym	Deficient Enzyme	GAG Accumulated	Gene locus	Incidence
MPS I	Hurler/Scheie	α- L-iduronidase	dermatan sulphate/heparan sulphate	4p16.3	1:100 000
MPS II	Hunter	iduronate-2-sulphatase	dermatan sulphate/heparan sulphate	Xq28	1:100 000
MPS IIIA	Sanfilippo A	heparan N-sulphatase	heparan sulphate	17q25.3	1:70 000
MPS IIIB	Sanfilippo B	α- N-acetylglucosaminidase	heparan sulphate	17q21	
MPS IIIC	Sanfilippo C	acetyl-CoA:α-glucosaminide N-acetyltransferase	heparan sulphate	8p11.1	
MPS IIID	Sanfilippo D	N-acetylglucosamine-6-sulphatase	heparan sulphate	12q14	
MPS IVA	Morquio A	galactosamine-6-sulphatase	keratan sulphate, chondrointin sulphate	16q24.3	1:200 000
MPS IVB	Morquio B	β- galactosidase	keratan sulphate	3p21.33	
MPS VI	Maroteaux-Lamy	arylsulphatase B	dermatan sulphate/chondroitin sulphate	5q11-q13	1;250 000-600 000
MPS VII	Sly	B-glucuronidase	dermatan sulphate/heparan sulphate/chondroitin sulphate	7q21.11	< 1: 250 000
MPS IX	hyaluronidase deficiency	Hyaluronidase	hyaluronan	3p21.3-p21.2	4 cases reported

Table 1.2. Major clinical symptoms of MPS

System	Symptoms
Coarse facial features	• Enlarged head • Large tongue (macroglossia) • Flat bridged nose • Short neck
Ocular	• Corneal clouding
Gastrointestinal	• Bulging stomach due to enlargement of liver and spleen (hepatosplenomegaly) • Umbilical or inguinal hernia • Chronic diarrhoea
Ear	• Persistent and recurrent infection of ear (otitis media) • Conductive hearing loss
Pulmonary	• Respiratory tract infection • Upper airway obstruction and chronic bronchitis
Cardiac	• Coronary artery stenosis • Cardiac valve disease • Cardiomyopathy • Fibroelastosis • Acute heart failure
Musculoskeletal	• Thoracolumbar kyphoscoliosis (abnormal curvature of thoracic & lumbar spine in both coronal and sagittal plane) • Joint stiffness and contracture • Claw hands • Hip dysplasia • Dysostosis multiplex

1.2.2 Musculoskeletal symptoms of MPSs/ Orthopedic aspects of MPSs

Musculoskeletal manifestations are a common and prominent feature in most MPSs. In the attenuated forms, the rheumatic symptoms include bone pain, stiffness and contracture of joints that can easily be misdiagnosed. In contrast, the severe forms of the disease show early and specific symptoms affecting numerous organ systems [2, 3, 6, 7]. Joint stiffness without inflammation can be symptomatic evidence of MPS [8]. Similar to the

major manifestations of joint and bone disease found in other LSDs are disproportional short stature, bone pain, joint stiffness, osteopenia (decrease in BMD to a level which is lower than the normal but not low enough to be classified as osteoporosis), osteonecrosis (death of bone cells due to reduction in blood flow) or osteosclerosis (abnormal bone hardening that causes increased BMD which can be detected in radiographs as a region of increased opacity) [2, 3, 9]. The skeletal abnormalities associated with MPS are often more generally distributed throughout the body (diffuse) compared to the localized radiographic skeletal manifestations seen in other rheumatic diseases like erosive bone lesions, joint space narrowing or the joint effusions seen in inflammatory arthritis (e.g. Juvenile idiopathic arthritis, JIA) [1, 2, 5].

The deposition of partially degraded GAGs in the lysosomes of connective tissue cells and chondrocytes is believed to be responsible for musculoskeletal symptoms in almost all types of MPS. Some of the common skeletal symptoms found in MPSs, depending on the location of GAG deposition, are outlined below.

Dysostosis multiplex

Dysostosis multiplex refers to a group of characteristic skeletal abnormalities seen through radiographic imaging in MPS patients. They mostly involve deformities of the bones and cartilage of vertebrae, ribs and other extremities. Skeletal symptoms categorized as dysostosis multiplex are given in Table 3 [2, 3, 5]**.** They involve bone modeling-remodeling defects of the skull, thorax, spine, pelvis or hips, long bones and

distal extremities like hands, feet and knee. These manifestations sometimes give rise to secondary osteoarthritis [2, 3, 5].

Table 1.3. Dysostosis Multiplex

Bone	**Phenotype**
Skull	• Macrocephaly: enlargement of skull • Thickened calvarium or skull cap • J shaped sella turcica
Thorax	• Oar shaped or paddle shaped ribs (i.e, wide in the anterior end and narrow in the posterior end) • Short and thickened clavicles
Spine	• Odontoid hypoplasia: incomplete development of odontoid process • Thoracolumbar kyphoscoliosis • Gibbus deformity (sharp posterior curvature of spine) • Flattened vertebral bodies
Pelvis/Hips	• Flattened acetabula • Flared iliac wings: Rounding & thickening of iliac wings • Hypoplasia i.e. incomplete development of iliac bones • Coxa valga: Deformity of hip where the angle between the shaft and head-neck of femur is more than 135^{o}. • Dysplastic femoral head (abnormal formation of femur head)
Long bones	• Shortened long bones • Thickened diaphysis • Irregular metaphysis leading to hypoplastic or dysplastic femoral head and long, narrow femoral neck • Narrow and hypoplastic epiphyses
Hands/Feet	• Shortening, thickening and proximal pointing of metacarpels and metatarsels • Bullet shaped phalanges
Knees	• Genu valgum: Knock knees where knees touch but ankles do not

Some of the classic features of dysostosis multiplex, a flattened acetabulum, dysplastic femoral head, and coxa valga, lead to hip dysplasia which may progress to a complete or partial dislocation of the hip. Degenerative wear and tear of cartilage (arthrosis) of the dysplastic joint can be painful. Surgery to locate the hip is often required, but may become difficult in patients with femoral head osteonecrosis [5, 6].

Atlanto-axial instability or subluxation (disorder of atlas and axis that impairs the rotation of neck) is caused by hypoplasia of the odontoid process in the spine that along with GAG accumulation in the surrounding tissue of the spine may sometimes result in spinal cord compression. This compression may cause neurological symptoms[5]. Similarly kyphoscoliotic deformities (abnormal curvature of spine) like the gibbus deformity or thoracolumbar kyphosis leads to hunchback in patients, causing tremendous discomfort.

Though the exact pathogenesis of dysostosis multiplex is not completely understood, it is believed to result from disturbances in endochondral bone formation and membranous growth due to GAG accumulation in the articular cartilage. These may sometimes worsen with stresses that arise from the skeletal deformities [2, 7].

Joint stiffness and contractures

Joint stiffness and contractures are the most common skeletal manifestation in all MPSs but MPS IV and MPS IX. The main cause of the stiffness and contractures of joints is thought to be accumulation of GAGs in joint capsules, tendons and ligaments making them thick and therefore stiff. These three tissues are made up of similar components including collagen, PGs and water, but that differ in their functions. Tendons are non-elastic fibres that bind muscle to bones and thus help in distributing tensile loads. Ligaments are strong elastic fibres that bind bone to bone and joint capsules are sacs that enclose joints containing synovial fluids. Ligaments and joint capsules together help to prevent the loss of synovial fluid that helps in lubrication and provides stabilization by preventing excessive motion. Accumulation of GAGs hinders their function and causes stiffness and contracture. Metaphyseal and epiphyseal deformities due to defective bone

modeling may also contribute [2, 3, 5]. Very often, joint stiffness and contractures are misdiagnosed as rheumatic arthritis (RA) or JIA which also show stiffness and contracture of joints as one of its common symptoms. However there are certain features that differentiate the stiffness and contractures in MPS from that of RA and JIA. The most prominent difference is the absence of signs of inflammation. Neither local indicators (swelling, redness, warmth and tenderness) nor systemic indicators (fever, elevated erythrocyte sedimentation rate [ESR], C-reactive protein [CRP], white blood cell count) are evident[8]. Sometimes joint swelling occurs which is typically due to the underlying bony outgrowth rather than synovial inflammation. Therefore MPS patients do not respond to steroids or NSAIDs. Another difference is that unlike inflammatory arthritis, the stiffness in MPS patients is not worse in the morning, increased with long periods of rest, or relieved by increased physical activity or heat therapy. The joints most affected by stiffness in MPS include the shoulders and distal interphalangeal joints of the hands rather than proximal interphalangeal (PIP) and metacarpophalangeal (MCP) joints, leading to the characteristic claw hand deformity. However, in more severe forms of disease all joints can be affected [2, 3, 5].

Carpel tunnel syndrome (CTS) and trigger digits

CTS, a nerve compression syndrome affecting the median nerve of the hand, occurs due to thickening of the flexor retinaculum (a fibrous band of fascia at the base of the hand) and the tissues around the flexor tendon. This thickening is due to the deposition of excessive GAGs in the connective tissue of the flexor retinaculum and synovium around the tendon. CTS is a very common symptom found in MPSs but its diagnosis is often

delayed because the characteristic symptoms of numbness and pain are not reported by MPS patients. This may be because other prominent symptoms like stiffness or dysostosis multiplex hide CTS symptoms or alternatively, because of limitations in the ability of young patients to recognize and express pain. CTS is a rare symptom in children and its presence in early childhood can be a strong indicator of MPS [2, 3, 5].

CTS is often accompanied by trigger digits also called stenosing tenosynovitis which is caused by GAG accumulation in the capsular tissue of the joints or flexor tendons. This causes the digits to get stuck in a bent position, causing pain, swelling and limited motor skills [2, 3, 5].

Growth abnormalities/ Disproportional short stature

Short stature is common among MPSs. It is prominent in severe forms of MPSs, whereas it may occur as a mild symptom in attenuated forms, often staying unnoticed and giving normal or near-normal linear growth. The pathology thought to be responsible for this abnormality is disturbed endochondral ossification at the growth plate due to the deposition of GAG in the surrounding tissue. Structural abnormalities such as spinal kyphosis and genu valgum may also contribute to short stature. Axial growth, including the vertebral column, sternum, ribs and skull is found to be affected more than the appendicular growth of the bones of upper (arms, forearms, hands, shoulders) and lower (thighs, knees, legs and feet) extremities [2, 3, 5, 7].

1.2.3 Treatments

Treatments available for MPSs so far are enzyme replacement therapy (ERT) and hematopoietic stem cell transplantation (HSCT). Both are based on the principle of receptor mediated enzyme transfer known as “cross-correction”. After being synthesized in the rough endoplasmic reticulum, lysosomal enzymes are typically tagged with a mannose-6-phosphate (M6P) residue in the golgi apparatus to ensure they are targeted to lysosomes. These hydrolases are captured in the golgi apparatus by the mannose-6-phosphate receptor, and transported via budding endosomes. As the endosomes mature, the pH is lowered, leading to the dissociation of the lysosomal enzymes during the formation of mature lysosomes. Enzymes that are not captured by the receptor, are secreted by bulk transport into the extracellular space, where they can be recaptured by M6P receptor at the cell surface, and transferred to the lysosome via endocytosis. This whole process of receptor based intercellular enzyme transfer is called “cross correction” [10, 11].

In pharmacological therapy called ERT, exogenous recombinant enzymes are intravenously administered. These enzymes are taken into the cell through M6P receptors to replace defective enzymes. To date three recombinant enzymes had been approved by the FDA, laronidase (Aldurazyme) which is recombinant human alpha-L-iduronidase (rhIDUA), idursulfase (Elaprase) which is recombinant human-2-sulphatase (rhI2S) and galsulfase (Naglazyme) which is recombinant human N-acetyl-galactosamine-4-sulphatase (rhASB) for MPS I, MPS II and MPS VI respectively [1, 10]. These enzymes are effective at treating hepatosplenomegaly, pulmonary dysfunction and reduced joint

movement if given at an early age. However, major challenges with ERT are the correction of symptoms associated with the central nervous system because of the inability of the enzymes to cross the blood brain barrier (BBB) or the bones and heart valves which have limited or no vascularization [2, 10].

Another available therapy for MPS is a non-pharmacological therapy called hematopoietic stem cell transplantation (HSCT) from bone marrow or umbilical cord stem cells. Here, restoration of enzyme activity is achieved by engrafting a fully functional donor cell into the host tissue which produces and secretes the enzyme that is deficient in the host, allowing it to be taken up throughout the body via M6P receptors on the cell surface [5, 10, 11]. HSCT is found to improve cardiopulmonary function, joint mobility, hearing and vision, though its effect is still limited on bones and cornea. As the engrafted cell can cross the BBB, HSCT is thought to be promising for correcting the neurological symptoms. It is successfully used in the treatments of MPS I and MPS VI where it has shown improvement in cognitive function when given in early childhood while in other MPSs the clinical reports are still limited [2, 10]. Though HSCT provides a permanent source of enzyme that can decrease the accumulation of GAGs, skeletal manifestations still remain a challenge. Another important obstacle encountered in HSCT is the incompatibility between donor and host tissue that can result in graft versus host disease, and rejection. Given that, transplantation at a young age before there is irreversible organ and tissue damage is needed.

Combination therapy using ERT and HSCT is presumed to improve the outcome of treatment and is under investigation [1, 10]. According to the few clinical reports that are available, combination therapy was found to be safe with no severe graft versus host

rejection. Though there were reports of enzyme antibodies in some, they didn't stimulate immune mediated graft rejection. Similarly skin graft versus host disease were found in some patients but they were treatable by steroids. On the contrary, ERT facilitated GAG digestion before HSCT, and was found to create a better environment for donor engraftment [118-120]. Other advances in the treatment of MPSs include gene therapy where a new gene is inserted into the body to restore or treat the activity of a mutated gene and substrate reduction therapy where the synthesis of GAGs is inhibited. These approaches are still being evaluated in preclinical models and clinical trials.

1.2.4 Obstacles to therapy of the musculoskeletal system

The biggest challenge in the treatment of MPSs is the delivery of enzymes to the brain and the skeletal system (bones & cartilage). The skeletal system is most commonly affected in MPSs and skeletal pathologies respond poorly to the available treatments. This poor response to treatment is attributed to impaired endocytosis of enzymes by skeletal tissues due to the low number of M6P receptors present on skeletal tissues, which are required for both ERT and HSCT cross-reaction and reduced blood circulation in the cartilage which is also true for the heart valve and cornea that are also avascular tissue and thus resistant to treatments [1, 2]. Another commonly encountered hurdle in these treatments is their high cost which makes them inaccessible to patients in many parts of the world. More suitable, early and affordable treatments for skeletal deformities and other MPS symptoms are required.

1.2.5 Skeletal symptoms in mouse models of MPSs

Animal models have been an important tool not only in understanding disease pathogenesis and progression, but also in identifying and testing therapies. Murine models, because of their short reproductive cycle and lifespan as well as their ability to breed to different genetic backgrounds, are extensively used in genetic disease research. In order to understand the complete phenotype and pathogenesis of several MPSs, murine models have been generated and characterized. Similar to humans, mouse models of different types of MPSs also display a range of skeletal features which are summarized in Table 4 [12–15].

Table 1.4. Skeletal features in MPSs murine models

Type	Skeletal symptoms
MPS I	• Flattened facial profile, broadness of face, loss of tapered snout • Thickening of digits, ribs, zygomatic arches & fibulae • Anterior flaring of ribs (oar-like) • Periosteal bone formation in knee joints • Spinal stenosis • Lysosomal storage within chondrocytes of articular cartilage and trachea
MPS II	• Gibbus deformity in hind limbs • Thickened digits, skull & claw shaped paws • Tibiotarsal joint deformity causing hind limb ankyloses (stiffness in joints due to rigidity of bones of joints) • Sclerosis • Enlargement of skull bones & broadened snouts • Appendicular bone enlargement • Misalignment of calcaneous bone (heel) in tarsotibial joints • Periosteal bone formation on distal tibia • Thickened long bones in hind limbs, vertebrae, ribs • Increased whole body bone mineral density • Increased bone cross-sectional area
MPS IIIA	• Thickened calvarium • Vertebral deformation • Cartilaginous matrix proliferation into spinal canal
MPS IVA	• No obvious abnormalities

MPS VI	• Facial dysmorphism- shortened maxillae & large skull • Shortened & thickened femur and humerus • Thickened and wavy ribs • Pelvic abnormality • Persisting growth plates unlike closed growth plates of wild type animals • Vacuolated & ballooned chondrocytes • Broadened growth plates
MPS VII	• Facial dysmorphism-blunted nose, broad zygomatic arches • Narrow rib cage, broad ribs • Flared metaphysis • Sclerotic long bones • Sclerosis of calvarium • Thickening of digits • Spinal stenosis • Hobbled gait suggesting joint deformity • Growth retardation, shorter extremities, • Synovial proliferation, vacuolated synovial cells • Articular cartilage irregular and hypercellular • Widened, irregular and hypercellular growth plate • Chondrocytes enlarged and vacuolated

1.2.6 Pathogenic mechanisms responsible for musculoskeletal symptoms in MPSs

Pathogenic mechanisms responsible for cartilage destruction

Skeletal symptoms are present in almost all MPSs and have also been demonstrated to be present in murine models of these diseases. Since current treatments have only limited effectiveness in treating skeletal symptoms, understanding the pathogenesis of the bone and joint manifestations becomes crucial. Insights into new therapeutic strategies for MPSs, as well as identifying biomarkers to follow the progression of disease, are areas of intensive investigation. Several studies aimed at understanding the mechanisms

underlying joint and bone manifestations have shown inflammation as a consequence of GAG accumulation as a key factor. As a result of inflammation, chondrocytes from articular cartilage released inflammatory cytokines (IL-1β), TNF-α and nitric oxide (NO) resulting in apoptosis of chondrocytes. This was accompanied by release of matrix metalloproteinases (MMPs) especially MMP-1 and MMP-13 that degrade collagen from joints and bones, contributing to cartilage destruction [16, 17]. Apoptosis of chondrocytes was specific to those in articular cartilage, and no apoptosis was observed in chondrocytes of hyaline cartilage or other connective tissue cells despite GAG accumulation. This suggests that environmental factors, as well as GAG accumulation, contribute to the apoptosis of chondrocytes. Joint symptoms might depend on the type of GAG being accumulated, the type of inflammatory cascade triggered by the GAG, and the mechanical stress endured by the joint [16]. Studies have suggested that GAG mimics LPSs and therefore stimulates the LPS mediated inflammatory mechanism by elevating the expression of receptors like TLR4 (Toll like receptor 4), LBP (Lipopolysaccharide binding protein), CD14 and chemokine receptor CXCR4, as well as the downstream signalling molecule MyD88 (myeloid differentiation primary response protein-88). This GAG-induced inflammation cascade was stimulated both in chondrocytes and synoviocytes, ultimately causing cartilage and bone destruction [17, 18].

Pathogenic mechanisms responsible for disorganized growth plate

Studies have shown growth plate abnormalities in MPSs that are thought to be a consequence of the loss of the collagenolytic activity of cathepsin K – an osteoclastic cysteine protease. Cathepsin K completely breaks down the triple helical structure of

collagen giving space for new bone formation by osteoblasts. Accumulating GAGs, especially dermatan sulphate and heparin sulphate, form complexes with cathepsin K [19] inhibiting its collagenolytic activity, and thus resulting in decreased bone and cartilage resorption. Ultimately, inhibition of cathepsin K activity is thought to affect endochondral ossification- the process of long bone formation at the growth plate which requires recurrent replacement of cartilage. In the absence of cathepsin K activity, osteoclasts are unable to degrade collagen, contributing to skeletal abnormalities related to the growth plate such as a disorganized growth plate or shortened bones [20].

Understanding the pathogenesis of skeletal abnormalities associated with MPSs could allow the development of novel therapies through the disruption of unwanted steps in the disease progression cascade such as the GAG-cathepsin K interaction or the release of inflammatory cytokines and MMPs**.** Also it may help in establishing biomarkers for MPSs that can easily be detected and quantified, allowing severity in tissues to be predicted and responses to therapies to be quantified.

1.3 MPS IX (OMIM # 601492)

MPS IX is a rare autosomal recessive disorder caused by mutations in the hyaluronidase 1 (HYAL1) encoding gene, *HYAL1*. HYAL1 is a lysosomal endoglycosidase that degrades hyaluronan (HA) [21], a GAG that is abundant in the extracellular matrix (ECM) of loose connective tissues, including the synovial fluid of the joint, Wharton's jelly of the umbilical cord & vitreous humor of the eye [22]. HA plays an important role in

maintaining the homeostasis of the ECM and regulating cell proliferation, cell differentiation, cell-cell adhesion and migration through its interaction with matrix hyaluronan binding proteins and hyaluronan receptors on the cell surface [22, 23].

MPS IX was first described in 1996 in a 14 year old female patient with short stature, periarticular masses, occasional swelling of joints and mildly dysmorphic facial features that included a flattened nasal bridge, and submucosal cleft palate with a bifid uvula [24]. Radiographic findings showed a nodular synovium, acetabular erosions, a popliteal (Baker's) cyst and joint effusions in the knees, ankle and pelvis. The patient underwent bi-lateral hip surgeries and unilateral hip replacement before the age of 19 years. HA storage was found in lysosomes of macrophages and fibroblasts of joint masses and plasma HA levels were elevated by 38-90 fold, whereas serum hyaluronidase activity was deficient. The mutations found in *HYAL1* of this patient were a 1412G→A point mutation that causes a non-conservative amino acid substitution of Lys by Glu at position 268 and an intragenic rearrangement 1361del37ins14 (insertion/deletion mutation) that brings about a frame shift in the coding sequence forming a premature termination codon. Both the mutations together make the patient a compound heterozygote (which is the presence of two different types of mutation on each allele of the gene) [21].

Three additional cases of Saudi Arabian siblings (two males of 13 and 22 years of age respectively and an 11 year old female) from a consanguineous family were found more recently that exhibited a homozygous deletion mutation, c.104delT, in *HYAL1*, leading to the formation of a premature termination codon, p.Val35AlafsX25. They

showed chronic joint disease involving multiple joints (knee, hip and even small joints of hand) and characterized by proliferative synovitis and joint effusions. In contrast to the first case, they didn't show facial dysmorphism or short stature [25]. These patients were initially diagnosed with JIA, but that did not respond to treatment with NSAIDs. With only four patients known to date, the complete phenotype of this condition, and mechanism of its pathogenesis, is yet to be defined. Though it is expected that additional patients diagnosed with JIA actually have MPS IX; studies to identify such patients are ongoing.

A mouse model of HYAL1 deficiency was generated and characterized previously to identify the murine disease phenotype and compare it with the human condition [26]. Both male and female *Hyal1* knockout mice were found to be viable, fertile and completely normal in appearance. They didn't show organomegaly or any abnormality in tissue morphology, body size or weight. In contrast to MPS IX patients, the murine model didn't show joint tissue masses or elevated serum HA levels. The only significant difference observed in them, compared to wild types, was in the knee joints. *Hyal1* knockout mice showed loss of proteoglycans (PGs) from the surface of articular cartilage as early as 3 months of age which was progressive up to the latest time point examined of 20 months. This loss of PGs was observed as a decrease in the intensity of Safranin O and toluidine blue staining. Also a bony outgrowth called an osteophyte was observed in the tibial surface of one of the animals at 20 months of age. In addition to this, there was an increased staining of HA binding protein (HABP) on the pericellular and cytoplasmic surface of chondrocytes of articular cartilage and epiphyseal growth plate that progressed with age demonstrating deposition of HA. Non skeletal tissue didn't

show any HA accumulation suggesting the skeletal system as the major affected system in HYAL1deficiency. Overall, the MPS IX murine model is milder and doesn't recapitulate the human disease completely but shows early and progressive joint disease similar to the human condition which is predictable given the high turnover rate of HA in joints.

Similarly, human MPS IX also displays a mild phenotype compared to other MPSs that is mostly limited to the joints, despite the abundant distribution of HA in the body. Taken together, the mild phenotype of HYAL1 deficiency and the absence of accumulation of HA in non-skeletal tissues suggested that other hyaluronidases might also play a role in HA degradation. To test this redundancy, mice deficient in HYAL2, HYAL3 or all isoforms of β-hexosaminidase combined with HYAL1 (Triple knockout, TKO) were characterized [27–29]. Mice deficient in HYAL2 and HYAL3 didn't show any broadly distributed tissue HA accumulation [27, 29] but interestingly mice deficient in β-hexosaminidase and HYAL1 showed HA accumulation much higher than the mice with deficiency of either HYAL1 or β-hexosaminidase alone, suggesting a functional redundancy between the endoglycosidase HYAL1 and the exoglycosidase β-hexosaminidase. This redundancy likely explains the mild phenotype in both human and murine MPS IX [28].

1.4 Glycosaminoglycans (GAGs)

Glycosaminoglycans are large, complex, unbranched, and negatively charged polysaccharides containing repeating disaccharide units consisting of a uronic acid, either glucuronic or iduronic acid, and an amino sugar, either N-acetyl-galactosamine or N-acetyl glucosamine. Because of their viscous and lubricating nature, resembling mucous, GAGs were also termed mucopolysaccharides. Synthesis of GAGs takes place in the golgi complex or endoplasmic reticulum (except HA) where they undergo modifications of different types like sulfation and transfer to proteins. Once synthesized, they are targeted to the cell surface or the ECM of the cell where they undergo further modifications. Ultimately these modified GAGs reside mostly in the ECM and sometimes on the cell surface either as free molecules or attached to proteins as proteoglycans (PGs) [30]. On the basis of the degree of sulphation, GAGs are divided into sulphated types which include chondroitin sulphate (CS), dermatan sulphate (DS), keratan sulphate (KS) and heparin sulphate (HS) and the non-sulphated type which include hyluronan (HA). Except HA, all other GAGs exist as PGs where saccharide chains are attached to either a serine or asparagine residue of a core protein through a glycosidic bond. Some examples of proteoglycans are aggrecan (in cartilage), versican (in blood vessels, skin, and brain), syndecan (in epithelial cells & fibroblasts), decorin and biglycan (in connective tissue cells). These GAGs and PGs play important roles in various cellular process like cell signalling and development, cell surface receptor binding, angiogenesis, tumor progression, metastasis, cytokine binding and specific protein binding. The degradation

of GAGs occurs primarily in the lysosomes of the cell by various lysosomal enzymes whose deficiency causes accumulation of GAGs within lysosomes causing MPSs [30–32].

1.5 Hyaluronan

1.5.1 Structure and composition

HA is a naturally occurring linear GAG of variable size, ranging from 2500-25 000 repeating disaccharide units of *N*-acetyl- D- glucosamine (GlcNAc) (1→3-β linked) and D-glucuronic acid (GlcA) (1→4 - β linked) (Figue1.1). It is the only GAG which is not sulphated or epimerized. In solution, HA exists as a stiff and complex polymer making the solution viscoelastic [33, 34].

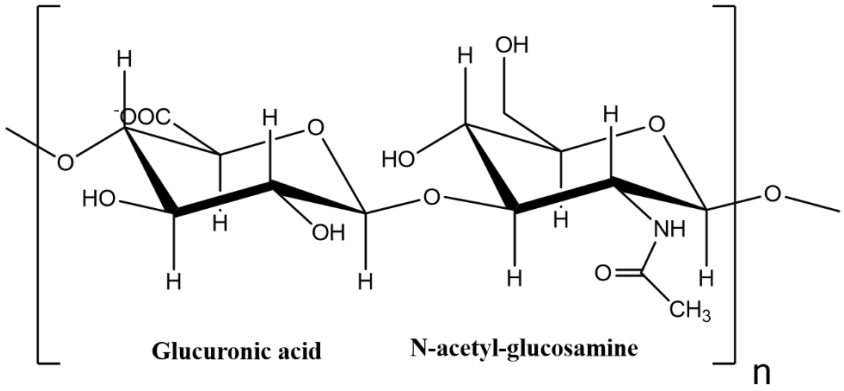

Figure 1.1. Chemical structure of hyaluronan

1.5.2 Distribution or occurrence in living organisms

HA is abundant throughout the body of vertebrates especially in loose connective tissues including skin, synovial fluid, vitreous humor of the eye, umbilical cord and Wharton's jelly where it occurs mostly in the ECM but also in the pericellular and intercellular space [22, 33]. In loose connective tissues like articular cartilage, HA exists in association with a proteoglycan called aggrecan which has chondroitin sulphate and keratan sulphate as GAGs bound through a link protein. Similarly, in the ECM of heart valves, HA is found bound to a PG called versican which together provides stabilization to ECM.

1.5.3 Biological and physiological roles of HA

The stiff and complex structure of HA in solutions help in maintaining viscoelasticity of liquid connective tissue such as vitreous humor of eye and synovial fluid of joints thus giving them shock absorbing and lubrication abilities. Its hydrophilicity serves to control water homeostasis in tissues and ECM by keeping the tissues hydrated, especially the joint cavity during articulation, and transporting water to different areas which affect cell motility, distribution and transport of plasma proteins. HA can bind to cell receptors, interact with mediators in the inflammatory pathways and accumulate around pericellular surfaces thus controlling functions like cell proliferation, differentiation, migration, inflammation, tumor development and invasion, cell-cell recognition, angiogenesis, mitosis and gene expression. Also, HA can accumulate around the cell to give protection from pathogens or extracellular molecules while providing a link between the cell and its

extracellular environment. These properties and biological functions of HA are shown to be dependent on molecular mass of HA [35].

1.5.4 HA synthesis

Cellular synthesis of HA is a highly controlled and unique process because in contrast to other GAGs which are made in the golgi complex, HA is synthesized on the inner surface of plasma membrane as a linear polymer. Unlike other GAGs which are synthesized linked to a core protein as PGs, HA is synthesized as a free polysaccharide and does not require attachment to core protein for polymerization. Nonetheless, it does bind to certain PGs like hyaluronectins (hyaluronic acid binding proteins), for example aggrecan in the cartilage. It is the enormous size of HA and the high viscosity that makes its complete synthesis impossible intracellularly and so while it is being synthesized on the inner surface of the plasma membrane, it is simultaneously pushed outside the cell where it stays in the ECM or attached to the cell surface via receptors. Synthesis of this type of molecule in the golgi complex or endoplasmic reticulum might destroy the cell [34]. In specific cases like inflammation, HA can also be retained inside the cell [36].

HA is synthesized by a class of enzymes called hyaluronan synthases (HASs) which are of three types in mammals, HAS1, HAS2 and HAS3. They are integral membrane proteins with different rates of HA synthesis. HAS1 is the least active but constitutively expressed of the hyaluronan synthases, and produces a small amount of high molecular mass HA (2 X 10^6 Da). Mice deficient in HAS1 were normal and viable until they were exposed to stressful conditions [37]. HAS2 on the other hand is involved in synthesis of very high molecular mass HA and is more active in synthesizing HA than

HAS1. HAS2 is also involved in embryogenesis, especially cardiac morphogenesis. Mice lacking HAS2 showed embryonic lethality at embryonic day 9.5 due to a failure to form the normal cardiac cushion which is essential for cardiac and vascular morphogenesis and development[27, 38]. HAS3 is the most active of all three hyaluronan synthases and produces comparatively low molecular weight HA (0.2 X 10^6 Da – 2 X 10^6 Da) but in large amounts. HAS3 null mice were also viable and fertile with a normal life span [39] but a recent study has shown altered neuronal activity in them due to reduction in the size of brain extra cellular matrix caused by HA deficiency [40]. Although the exact function of each synthase is not known clearly, it is believed that HA synthesized by HAS3 being shorter binds well with cell surface receptors and stimulates signal transduction pathways[34].

1.5.5 HA degradation

Catabolism of HA in vertebrates is a rapid and constant process. Most HA degradation is local, but some does enter systemic circulation and is taken up by the lymph nodes and other local tissues mostly liver and spleen by HA receptor mediated endocytosis. Once inside the cell, catabolism of HA takes place through enzymatic degradation by endoglycosidases (HYALs) and exoglycosidases (β-hexosaminidase and β-glucuronidase). In a normal healthy individual around one third of bodily HA (5 of 15 g) is turned over daily [22, 34].

Hyaluronidases (HYALs)

In humans, there are 6 hyaluronidase-related genes, *HYAL1*, *HYAL2*, *HYAL3*, *HYAL4*, *SPAM1* and *HYALP1* located as clusters on two chromosomes. *HYAL1*, *HYAL2* and

HYAL3 are located on chromosome 3p21.3 and code for HYAL1, HYAL2 and HYAL3 respectively. Similarly *HYAL4*, *SPAM1* and *PHYAL1* are located on chromosome 7q31.3 coding for HYAL4, PH-20 and a pseudogene which is transcribed but not translated in humans [41]. These genes show a high degree of similarity (40%) in their amino acid sequence. In mice, homologues to these genes are present, *Hyal1, Hyal2, Hyal3* located on chromosome 9F1-9F2 and *Hyal4, Ph20, pHyal1* plus an extra seventh gene called *Hyal5* located on 6A2 chromosomes [41, 42, 43].

HYAL1 is a lysosomal endoglycosidase that breaks HA fragments into oligomers as small as tetrasaccharides. It is comprised of 435 amino acids and is expressed in multiple tissues albeit highest in those involved in HA metabolism like liver, kidney and spleen and lower in heart, lungs, placenta, skin and skeletal muscle. As expected for a lysosomal enzyme, it has a pH optimum of 3.7 and shows little activity above a pH of 4 [44]. Deficiency in HYAL1 activity causes MPS IX [21, 24, 25]. Similar to human MPS IX, a mouse model deficient in HYAL1 activity showed a mild phenotype limited to joints [26].

HYAL2 is another major endoglycosidase for HA degradation in somatic tissues. It is a glycosylphosphatidylinosotol (GPI)-linked membrane protein present on the plasma membrane of the cell [45], and is presumed to initiate the degradation of high molecular mass HA into smaller fragments of approximately 20 kDa that can be internalized into the cell. It consists of 473 amino acids and has a moderately acidic optimum pH [46], but its hyaluronidase activity is weak [47]. Expression of HYAL2 is present in most tissues except brain. The role of HYAL2 in HA degradation and manifestation of its deficiency in humans is still not known. Therefore to understand it better, HYAL2 null mice were generated [27] and characterized. These *Hyal2* knockout mice showed significant

pre-weaning lethality as well as skeletal defects and cardiopulmonary dysfunction in surviving mice [27, 48] On the basis of the phenotypic evidence available from the HYAL2 deficient mouse model, the search for human patients with HYAL2 deficiency is ongoing.

HYAL3 is weakly expressed in multiple tissues including brain and testis. Although broadly expressed, the exact function of HYAL3 is not well documented. Characterization of HYAL3 KO mice didn't show any HA accumulation suggesting no role for HYAL3 in HA degradation [29]. This was consistent with the finding that *HYAL3* doesn't have hyaluronidase activity although *HYAL1* activity was significantly increased in the presence of *HYAL3* overexpression *in vitro.* This was demonstrated in Baby Hamster Kidney (BHK) cells where constitutive HYAL3 expression increased the acid active hyaluronidase activity which was not detected when HYAL3 was transfected to fibroblasts lacking HYAL1 [49].

SPAM1 (Sperm adhesion molecule 1) is a GPI-anchored hyaluronidase also known as PH-20, an enzyme with both acid and neutral pH optima [50]. Unlike other hyaluronidases it is primarily expressed on the surface of sperm [41]. It is a multifunctional enzyme that plays an important role in fertilization by facilitating the penetration of sperm into the ovum's cumulus layer which is rich in HA. It also acts as a receptor for HA and thus triggers HA mediated signalling cascades by binding to the zona pellucida and initiating the acrosome reaction [51]. Mice deficient in PH-20 are fertile and display hyaluronidase activity, suggesting the role of other hyaluronidases in fertilization along with PH-20 [52].

HYAL4 is the least understood of these enzymes. There is no evidence of HA degrading activity associated with HYAL4 in the literature. On the contrary, HYAL4 is a chondroitinase that has affinity for degrading chondroitin (Ch) and chondroitin sulphate (ChS) [53, 54].

PHYAL1 is a pseudogene which is transcribed but not translated into an active enzyme in humans due to the occurrence of an abnormal stop codon due to a frameshift resulting from a deletion. However, it is translated in other species, including mice, where it believed to encode a 57 kDa protein [34].

Hyal5 is located in a cluster along with *Hyal4, pHyal1* and *Spam1* on chromosome 6A2 of mice. It codes for the hyaluronidase enzyme HYAL5 that along with PH-20 is involved in enabling the penetration of sperm into the ovum's cumulus mass. Therefore, it compensates for PH-20 activity in *Spam1* KO mice thus explaining the retention of fertility in that model. HYAL5 has a pH optimum ranging between 5-7 [42].

Exoglycosidases

Once the internalized HA fragments are broken down by HYAL1 into oligosaccharides, degradation of HA is completed by lysosomal exoglycosidases which further degrade HA tetrasaccharides into monosaccharides. There are two known exoglycosidases, β-hexosaminidase (N-acetyl-β-glucosaminidase) and β-glucuronidase which have shown to play role in HA degradation *in vitro* by eliminating sugar subunits from the terminal ends of HA [55].

β-hexosaminidase (N-acetyl-β- glucosaminidase) is a dimer encoded by *HEXA* and *HEXB* genes where *HEXA* codes for the α-subunit of the enzyme and *HEXB* codes for the β-subunit of the enzyme. *HEXA* and *HEXB* genes in humans are located on

chromosomes 15 and 5 while in mice, they are on chromosomes 9 and 13. There are several isoforms of the enzyme named as β-hexosaminidase-S (homodimer of α-subunit, αα), β-hexosaminidase-A (a heterodimer consisting both α and β subunits, αβ) and β-hexosaminidase-B (homodimer of β-subunit, ββ). They are responsible for removing the terminal N-acetyl-glucosamine residue from GAGs including HA and GM_2 gangliosides by cleaving the β1, 4 linkage [55]. Mutation in *HEXA* or *HEXB* in humans as well as in mice, causes Tay-Sachs and Sandhoff's disease respectively. Mice deficient in both HEXA and HEXB (double knockout, DKO) displayed symptoms similar to mucopolysaccharidosis [56, 57] suggesting functional redundancy of hexosaminidases with hyaluronidases which was later confirmed in mice deficient for all three enzymes, HYAL1, HEXA and HEXB (Triple Knockout, TKO) [28].

The other exoglycosidase is β-glucuronidase which is encoded by *GUSB* located on chromosome 7 and 5 in humans and mice respectively. It is involved in removing the terminal β-glucuronic acid residue from GAGs like hyaluronic acid, dermatan sulphate, heparin sulphate and chondroitin sulphate by cleaving the β1, 3 glycosidic linkage. Deficiency in β-glucuronidase activity leads to MPS VII caused by accumulation of dermatan sulphate, heparin sulphate and chondroitin sulphate. β-glucuronidase deficient mice also show symptoms similar to human MPS VII including skeletal and joint abnormalities [58]. HA was also shown to be a substrate for β-glucuronidase digestion *in vitro* [55].

Receptors involved in cellular uptake of HA through endocytosis

Various receptors known to bind HA and involved in its cellular uptake are CD44 (Cluster of Differentiation antigen 44), HARE (Hyaluronan Receptor for Endocytosis)

and LVYE-1 (Lymphatic Vessel Endothelial Receptor-1) [59–62]. CD44 is the most widely expressed and best characterized transmembrane HA receptor present on most cell types. It is known to be involved in receptor mediated endocytosis of HA further leading to its degradation by lysosomal enzymes which may be an important factor in several biological processes like cell migration and embryogenesis [33, 62, 63]. CD44 deficient mice developed normally with a mild hematopoietic and lymphocytic defect suggesting other receptor proteins are involved in HA uptake [64].

LVYE-1 is another transmembrane HA receptor that shows sequence homology with CD44. It is tissue specific and primarily expressed in lymphatic and hepatic endothelial cells and blood vessels [60, 65]. Its exclusive expression in lymphatic vessels where the majority of HA is degraded, along with its ability to mediate HA internalization suggest it has a role in HA catabolism, although its exact role in HA turnover is still unclear and controversial [60, 66]. Also, normal lymphatic development, function and no HA accumulation in LVYE-1 null mice indicates the participation of other receptors in HA endocytosis [67].

HARE, also called stabilin-2 (Stab-2) is also a transmembrane protein which is highly expressed in sinusoidal endothelial cells of liver, lymph nodes and spleen. It mediates endocytosis of HA, heparin, and dermatan sulphate but shows no affinity for chondroitin sulphate. Thus HARE acts as a scavenging receptor for several GAGs to be endocytosed and cleared from the circulation [59, 68].

Model of HA turnover

Though the exact pathway of HA degradation is not known completely, it is believed that HA turnover is initiated by HYAL2 which catabolizes high molecular mass HA (approx.

10^6 Da) into low molecular mass HA of approximately 20 kDa. These HA fragments are then taken into the cell via cell surface receptors like CD44, LVYE-1 and HARE. Once inside the cell, these intermediately sized HA fragments are taken up by endosomes which gradually mature into lysosomes where they are degraded by lysosomal enzymes. HYAL1 and the exoglycosidases, β-hexosaminidase and β-glucuronidase, which likely work in concert to generate sugar monosaccharides [69] (Figure 1.2).

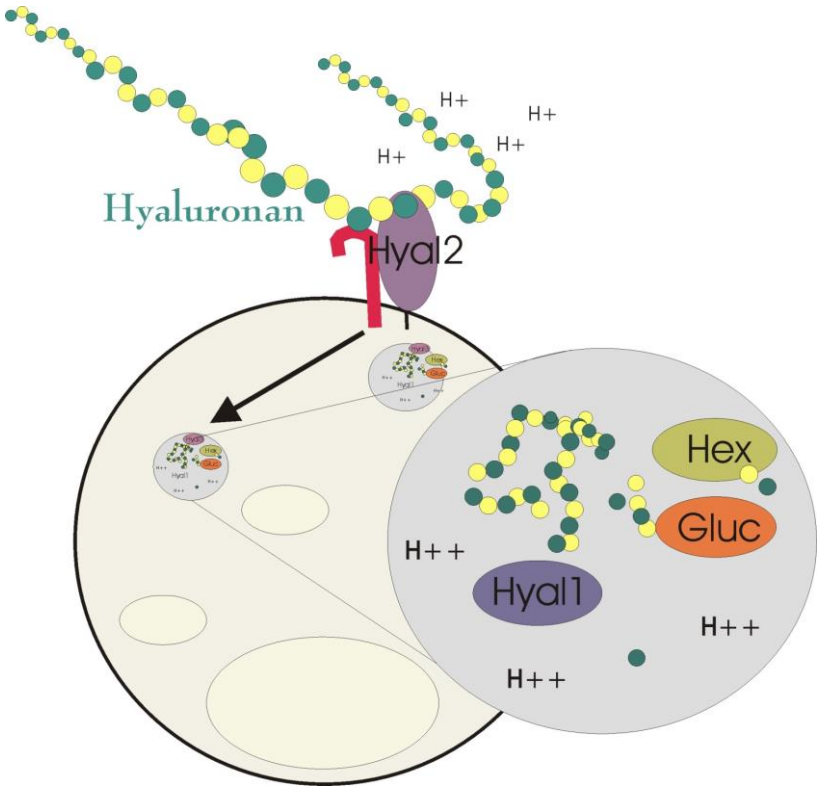

Figure 1.2. Proposed model of HA degradation (Courtesy: Dr. Barbara Triggs-Raine)

1.5.6 HA in cartilage & bones

HA has various functions in the skeletal system where its synthesis and degradation are highly regulated**.** In the ECM of cartilage HA exists as a complex with aggrecan via a link protein. Aggrecan is a major PG of articular cartilage that provides it with load

bearing capacity. On binding with HA, aggrecan forms a stable complex that allows it to stay immobilized in cartilage [70]. Therefore, the main function of HA in cartilage is to immobilize aggrecan. The larger the size of the aggregates in the cartilage, the more immobilized they will be in the collagen network and thus retain the elasticity of cartilage [71]. The rate of HA synthesis by HASs, degradation by HYALs and interaction with other proteins determines its properties in cartilage.

The major HA synthases responsible for HA synthesis in cartilage of humans, animals and cell culture is HAS2. HAS3 is also reported to be expressed in chondrocytes but its expression is lower than HAS2 and is sensitive to environmental factors like age and cytokine exposure. In contrast to HAS2 and HAS3, HAS1 expression in chondrocytes is not well understood and is thought to be variable. In synovium, HAS1 and HAS2 are the major synthases [72, 73]. For the purpose of degradation, all three major somatic HYALs (HYAL1, HYAL2 and HYAL3) are expressed by chondrocytes [74]. Previous studies on HA degradation by chondrocytes have demonstrated the endocytosis of HA by CD44 receptors. The HA-CD44 interaction was shown to be required for maintaining homeostasis of cartilage metabolism, and any disturbance promoted matrix remodeling [75–77]. The turnover of HA and aggrecan are co-regulated. However HA, and the HA bound link domain of aggrecan are endocytosed and degraded intracellularly while the remainder of aggrecan is catabolized outside the chondrocyte [78, 79].

HA does not have a structural role in bone similar to that in cartilage [80]. The exact function of HA in bones is still unclear though it is thought to take part in bone turnover by regulating osteoclasts. Though studies have shown the presence of CD44 on the

surface of osteoclasts, which are capable of binding to HA [80], it is still very unclear whether these osteoclasts are produced within the bone or derived from cells outside the bone [81]. Studies have shown that HA binds to hydroxyapatite of bone matrix but does not affect its mineralization [82]. HA is synthesized in osteoblasts of the periosteal layer of the tibial diaphysis as well as in osteocytes of cortical bone on stimulation by parathyroid hormone (PTH). On the contrary, the endosteal layer on the contrary does not synthesize any HA even on stimulation by PTH [83]. *In vitro* studies have suggested a role for HAS2 and HAS3 in the synthesis of HA and the role of HYAL2, HYAL3 and HYAL4 in the degradation of HA, in osteoblasts [84]. Overall, the role of HA in bones is still not explored fully, but a complete understanding will be important in understanding the pathogenesis of conditions like MPS IX which are characterized by an imbalance in HA regulation.

1.6 Structure and composition of skeletal system

The human skeleton is comprised of 206 bones that together contain 99% of the body's total calcium. The skeleton plays a major role in providing a framework to support the whole body. It protects the vital organs of the body, including the brain, heart and lungs, holds the bone marrow that produces red and white blood cells, acts as a reservoir for minerals like calcium & phosphates, and provides a site for the attachment of muscles, ligaments and articulation of joints necessary for movement to the body. An outline of the structure and composition of the skeletal system may assist in understanding the phenotype and interaction between various components and thus the pathogenesis of bones and joints in producing the phenotypes of MPSs.

1.6.1 Bones

Bone is a dense connective tissue consisting of a flexible but tough ECM containing both organic and inorganic substances. The organic substances include type I collagen, the GAGs HA, CS and KS, proteoglycans, glycoproteins, growth factors and bone morphogenetic proteins. The inorganic components primarily include calcium and phosphorus as calcium hydroxyapatite ($Ca_{10}(PO_4)_6(OH)_2$, but also possess magnesium, calcium, sodium and bicarbonate. It is the association of hydroxyapatite and collagen that makes the bones hard [85].

Depending upon shape, bones are divided into five categories- long bones, short bones, flat bones, irregular bones and sesamoid bones. Long bones are mostly involved in movement of skeleton and include the femur, tibia, humeri, radii, ulnae, metacarpals, metatarsals, phalanges and clavicles. They are mostly characterized by the presence of growth plates on both ends which are protected by articular cartilage, a hollow shaft called as diaphysis which is mostly made of cortical bone, a cone shaped region called the metaphysis below the growth plate and a rounded region called the epiphysis above the growth plate. Both the metaphysis and epiphysis are primarily comprised of trabecular bone surrounded by a very thin layer of cortical bone. Short bones are less involved with movement and mostly provide support. They include carpals and tarsals. Flat bones include cranium, sternum, ribs and pelvis which provide protection to the body's vital organs. Irregular bones include bones like the vertebrae and sacrum that do not have a defined shape. And lastly, a common example of sesamoid bones are the short bones embedded in tendons is the patella of knee joints [85] (Figure 1.3).

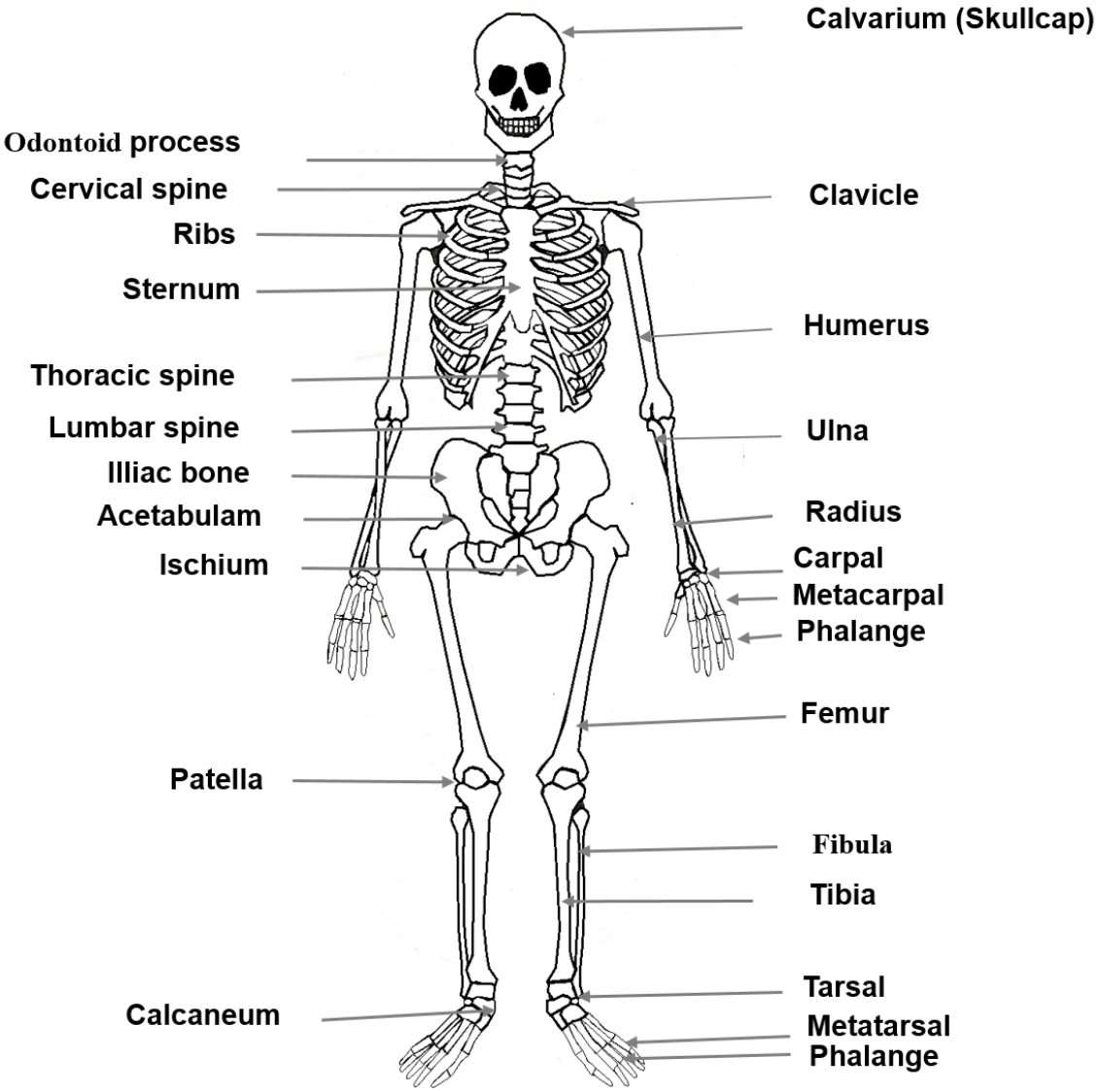

Figure 1.3. Human skeleton (http://montessoriworkjobs.blogspot.ca/2011/10/human-skeleton.html)

The bone is comprised of three cell types. First are the osteoblasts which synthesize the organic components of the bone matrix and mineralize bone. Hence they are the important cells for bone formation, a process termed as ossification or osteogenesis. The two processes by which osteoblasts form bone are intramembranous ossification, which is initiated by mesenchymal cells, and endochondral ossification which is initiated by the proliferation of cartilage followed by mineralization to form primary new bone. Both processes begin before birth. Osteoblasts originate from undifferentiated mesenchymal cells called osteogenic cells. They are mononucleated and changes shape depending upon their state of activity. They are rich in the alkaline phosphatase (ALP) enzyme and have receptors for parathyroid hormone and estrogen. In normal bone growth they act as matrix building cells by synthesizing collagen, PGs and glycoproteins. They also play a role in calcification of bone. The second cell type is the osteocytes, which are mature bone cells differentiated from osteoblasts after embedding themselves in bone matrix lacunae. Osteocytes are the most abundant cells in bone, and are connected to each other as well as to osteoblasts via cellular processes that form a network of canals called canaliculi. They express osteocalcin, galectin 3 CD44 and other bone matrix proteins. They are thought to be involved with bone maintenance and possibly in bone growth, although this is unclear. They are relatively quiescent cells and can apparently act both as bone forming as well as bone resorbing cells. The last of the cell types are osteoclasts, a large multinuclear cell associated with bone resorption. They are derived from mononuclear monocyte-macrophage precursor cells. Bone resorption mostly depends upon the release of hydrogen ions and cathepsin K from osteoclasts

where hydrogen ions provide the acidic environment suitable for degradation of bone minerals and cathepsin K breaks down collagen from the bone matrix. Resorbing osteoclasts also secrete other proteins like Tartrate Resistant Acid Phosphatase (TRAP), and Matrix Metalloproteinase 9 (MMP9) to digest bone matrix [86] (Figure 1.4A)**.** During fracture repair, osteoblasts derived from the osteoprogenitor cells of the cambium layer of the periosteum and endosteum play a major role [85].

Structurally there are two parts to bones, cortical bone which is the hard and compact part of the bone that surrounds the bone marrow space and constitutes 80% of the skeleton. It is abundant in the long bones and flat bones. The other part, internal to the cortical bone, is trabecular bone, also called cancellous bone. This is the spongy part of the bone found in largest amounts near the end of long bones and inner parts of flat bones where it is interspersed in the bone marrow [85] (Figure 1.4B).

Bone is protected by a layer of connective tissue both internally and externally. A dense and fibrous connective tissue layer present on the external surface of bone is called the periosteum. It is located outside the cortex of cortical bone and is attached to the bone through Sharpey's fibers. It is absent at joints which are covered by articular cartilage. Microscopically, it consists of an inner fibrous layer of collagenous matrix, elastic fibres, few cells and also blood vessels and nerves. The outer cambium layer is thinner and highly cellular, containing osteoblasts, mesenchymal stem cells, fibroblasts and pericytes. Periosteal cells are osteogenic and fibroblastic in nature, i.e. they have the capacity to proliferate and transform into osteoblasts; likewise pericytes play a role in vascularization, together making the periosteum an important layer during bone growth and repair. In spite of its role in bone development, it is one of the most poorly

understood layers of bone. A similar layer, called the endosteum, is present on the interior of trabecular bone and is connected to the bone marrow. It also contains blood vessels, nerves and cells just like periosteum, but is thinner and exhibits less sensitivity towards physical, hormonal and mechanical stimuli, as well as a lower expression of periostin protein [87] and estrogen receptors alpha [88] compared to periosteal cells. Also unlike the periosteum, the endosteum exhibits more bone resorption than bone formation [89–92] (Figure 1.4C).

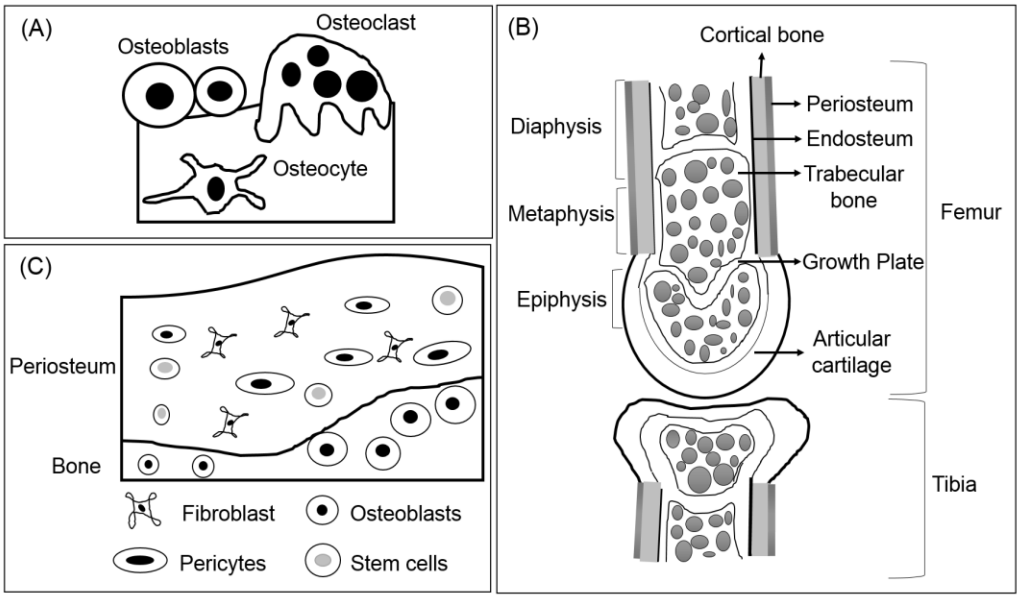

Figure 1.4. (A) Types of bone cells (B) Femur of knee joint showing cortical and trabecular bone; growth plate; epiphysis, metaphysis and diaphysis region of femur; periosteum and endosteum layer present outside and inside cortical bone respectively. (C) Cells of periosteum layer including fibroblast, osteoblasts and pericytes.

During a lifetime, bone constantly undergoes growth, modeling and remodeling. During development, growth occurs at the growth plate of long bones by endochondral ossification. The process by which bones adapt to mechanical loads by changing their

shape and size is called bone modeling. It removes any kind of damage that might occur due to mechanical loads and thus maintains bone strength. Modeling is a very common part of developmental growth, from birth to adulthood, and also occurs in response to mechanical loads produced by weight bearing, muscles and external forces[93]. Remodeling is another surface bone mechanism which involves breakdown of old bone matrix by osteoclasts and simultaneous synthesis of new bone matrix by osteoblasts. It occurs in response to injury or mechanical stress in order to heal or rearrange matrix according to need [93]. It is more common on the endosteal than periosteal surface [94]. Bone remodeling occurs throughout life and therefore is more frequent than bone modeling. In bone modeling, bone formation and resorption occurs on separate surfaces and are not linked with each other while in bone remodeling, the two processes are coupled and thus occur together [102].

1.6.2 Cartilage

Cartilage, another important part of the skeletal system, is a loose connective tissue mostly located around joints, ears, ribs and the intervertebral discs. The main function of the cartilage is to support soft tissues, allow movement, and provide weight bearing capacity especially in joints. There are 3 types of cartilage namely hyaline, fibrous and elastic cartilage. Hyaline cartilage contains a medium amount of collagenous fibres and is mostly present on the surface of bones that form joints and in the trachea. The matrix of fibrous cartilage is full of collagenous fibres and represents the cartilage of the intervertebral disc. On the other hand elastic cartilage contains both elastic and collagen fibres and can be seen in the ear and epiglottis [90]. It is composed of specialized cells

called chondrocytes that synthesize and maintain the extracellular matrix containing collagen, elastin and proteoglycans (PGs). The most predominant PG in cartilage is aggrecan, a chondroitin sulphate PG which gives compressive stiffness to the cartilage. In addition to this, other PGs like biglycan, decorin and perlecan are also present. The types of collagen present in cartilage are collagen type II, type IX and type XI. Collagen and aggrecan together provide the cartilage with high tensile strength and resistance against mechanical load and shock[95]. Hyaline and elastic cartilage is often surrounded by a layer of connective tissue called perichondrium and unlike other connective tissues, all types of cartilage lacks blood vessels, lymphatic vessels and nerves [90].

1.7 Micro-Computed Tomography (Micro-CT)

Computed tomography is a non-invasive imaging technique developed in 1973 by Godfrey Hounsfield [121] where unlike conventional radiography, X-ray transmission could be recorded from several angles thus providing 3-D view of the object being scanned. Later in 1980s, the concept of micro- computed tomography arose because the pixel size of the images that could be examined were in micrometers. It was useful in examining 3-D images of small specimens with micrometer resolution. The first microradiograph was described in 1981 by J. C. Elliott [122] and since then it is extensively being used in research involving animal models. With development in transgenic animal models, imaging techniques are increasingly being used in research not only for drug delivery studies but also for examining phenotypes and pathophysiology of diseases. In this study, micro-CT was used to assess the phenotype of an MPS IX mouse model. Micro-CT

basically consists of three elements, an X-ray source, sample bed and detectors**.** It works on the following principle, X-ray radiation from the source passes through an object. During this process, some of the radiation is absorbed by the object while the remainder is scattered depending upon the energy of the X-ray radiation and the density or arrangement of atoms in the object. Finally the X-rays scattered by the object are collected by the detectors from various angles to create a 3-D image. The proportion of X-rays absorbed or scattered is called as the attenuation coefficient which is a useful parameter when measuring density [96].

Micro-CT provides good contrast and spatial resolution for mineralized objects and therefore is commonly applied in musculoskeletal research to study different parameters from the whole body to the cellular level. It also allows the measurement of trabecular and cortical bone separately. In conventional techniques like radiography, the intensity of the X-ray passed from the scanned object gives a two-dimensional projection while micro-CT has the ability to assess both 2-D and 3-D structure both quantitatively as well as qualitatively. Similarly micro-CT also overcomes the limitation of histology which is commonly used to investigate things at a cellular level but requires that this sample is fixed, preventing further study. Micro-CT being non-invasive is often used in longitudinal research in animal models by performing *in-vivo* scanning. The main challenge encountered with it is its low sensitivity for soft tissues like cartilage which can be overcome or enhanced through the use of contrast agents [96]. We have used micro-CT as a major technique for this research because of its ability to provide detailed 3-D information of the skeletal system.

1.8 Rationale

As described earlier, skeletal deformities are common features of various types of MPS especially the attenuated types which are mostly progressive and often become debilitating for the patients. They do not respond to current available treatments like ERT and HSCT and their pathogenesis is still poorly understood. MPS IX is a rare and mild type of MPS, which unlike other MPSs shows primarily skeletal symptoms, mostly limited to joints. Our lab previously performed a general characterization of the *Hyal1*$^{-/-}$ mouse and compared it to human MPS IX [97]. A premature loss of proteoglycans from the articular cartilage of the knee joint was observed that progressed with age and was accompanied by the development of an osteophyte in one joint that was examined. The restriction of the MPS IX phenotype to the skeletal system makes the MPS IX (*Hyal1*$^{-/-}$) mouse model attractive for studying skeletal manifestations in all MPS disorders as the studies will not be complicated by abnormalities in other organ systems. However, the previous general characterization of the *Hyal1*$^{-/-}$ mouse model, which was done primarily by histological assessment, and where the emphasis was mostly on joints, was limited in terms of 3-D analysis and a much more detailed characterization of which joints are involved, and other characteristics of the affected joints and bones, is necessary. Therefore to understand the full range of skeletal symptoms in MPS IX, we further characterized the MPS IX mouse model using micro-CT. To accomplish this, the same MPS IX mouse model that had previously been found to have pathology in the knee joint was used. Micro-CT enables both quantitative and qualitative assessments of the mouse skeleton through *in vivo* imaging of animal models with high spatial resolution. It is

hoped that the information obtained will increase our understanding of the complete phenotype of MPS IX and help to generate new models of skeletal abnormalities due to GAG accumulation in MPSs. In the long term, this will also make *Hyal1*$^{-/-}$ a well characterized model that could be used for testing therapies targeting skeletal diseases related to MPSs as well as assist in determining if these therapies can be successfully provided in the postnatal period.

1.9 Thesis objective and hypothesis

The objective of this M.Sc. thesis is to characterize the complete skeletal phenotype of *Hyal1*$^{-/-}$ mice using micro-computed tomography. The investigation has the following specific aims:

1. To compare whole skeleton and 3-D macro architecture of *Hyal1*$^{-/-}$ mice with their age matched controls (*Hyal1*$^{+/+}$ or *Hyal1*$^{+/-}$).
2. To assess and compare trabecular bone mineral density and cortical tissue mineral density of *Hyal1*$^{-/-}$ mice with their age matched controls.
3. To assess and compare 3-D micro architecture of the bones of *Hyal1*$^{-/-}$ mice with their age matched controls.

Hypothesis

We hypothesized that HYAL1-deficiency in *Hyal1*$^{-/-}$ mice results in progressive changes in the articular cartilage that result in macroscopic skeletal manifestations that can be observed through micro-computed tomography.

Chapter 2

Materials & Methods

2.1 Animal Model

2.1.1 Generation of *Hyal1*-/- mice and controls

Mice heterozygous for the targeted disruption of the *Hyal1* gene, *Hyal1*$^{+/-}$ B6.129X1-*Hyal1*tm1Stn / Mmcd, were purchased from the Mutant Mouse Regional Resources Centers (MMRRC, Stock no. 000086-UCD, Davis, California, USA) in the year 2006 and maintained since then. These mice were generated by backcrossing the original strain 129X1, with C57BL/6J genetic background strain for 7 generations. The disruption of *Hyal1* was produced by homologous recombination, which resulted in a neomycin resistance gene (Neo) being inserted into exon 2. Mice for experimental studies were obtained by intercrosses between *Hyal1*$^{+/-}$ mice to generate *Hyal1* knockout (*Hyal1*$^{-/-}$) and control (*Hyal1*$^{+/+}$ or $^{+/-}$) mice.

2.1.2 Maintenance of experimental animals

Once the breeding began, the genotypes of progeny were identified using a PCR (Polymerase Chain Reaction) based method to amplify DNA prepared from ear clips at 14 days of age. Experimental mice (*Hyal1*$^{-/-}$ and control) were housed in groups of 3 per cage in the animal care facility of the University of Manitoba until they reached their experimental end point of six months or one year. Twelve pairs of *Hyal1*$^{-/-}$ and control animals, three male and three female at each time point, were used in this study. All the experimental procedures involving animals were reviewed and approved by the

University of Manitoba Animal Protocol Management and Review Committee according to the guidelines of Canadian Council on Animal Care.

2.2 DNA isolation

To prepare DNA from ear samples, the tissue was first incubated overnight at 55°C in 500 µl of lysis buffer (1 M Tris, pH 8.5; 10% SDS; 5 M NaCl; 0.5 M EDTA; 20 µg/µl Proteinase K [Invitrogen]). After assuring the samples were completely degraded, any remaining debris was separated from the aqueous phase by centrifugation for 10 minutes at 16000 g' (13200 rpm). The supernatant was removed to a new tube and isopropanol (500 µl) was added to precipitate DNA, which was later deposited to the bottom of the tubes by centrifugation at 16000 g (13200 rpm) for 10 minutes. The supernatant was then discarded and the tubes were kept inside a laminar hood for 10-15 minutes to evaporate any residual isopropanol. Then DNA pellet was resuspended in 500 µl of autoclaved distilled water. In cases where the DNA pellet appeared small, the amount of autoclaved water added to suspend the sample was reduced to 250-300 µl. To completely dissolve the pellet in water, tubes were placed in a 37°C water bath for 30 minutes. DNA was then stored at 4°C until genotyping.

2.3 Genotyping of mice

DNA isolated from ear samples were used for genotyping using PCR amplification. Each reaction tube contained 40.75 µl of ultra-pure distilled water that was DNAase and

RNAase free (Invitrogen, Life technologies); 5 µl of 10X ThermoPol reaction buffer (New England Biolabs) containing $MgCl_2$; 0.25 µl of Taq DNA polymerase (New England Biolabs), 1 µl of 10 mM dNTP mix (VWR) containing dATP, dCTP, dGTP and dTTP dissolved in highly purified water, pH 8.3; 1 µl of 100 ng/µl each of forward and reverse primers (Integrated DNA Technologies) and 1.5 µl of DNA. For the detection of the wild type allele the primers used were WPG 612 and WPG 613, which resulted in a product 340 bp in size and encompassed *Hyal1* exon 2. The disrupted *Hyal1* allele was amplified using primers WPG 610 and WPG 611 to generate a 270 bp product. The sequence of each primer is given in Table 2.1. A control sample that contained no DNA was also prepared with each reaction set to make sure there was no DNA contamination. PCR was performed in an Eppendorf Mastercycler using a 4 min denaturation step at 94°C, followed by 35 cycles of 1 min at 94°C for denaturation, 30 sec annealing at 52°C for wild type and 58°C for *Hyal1*$^{-/-}$ allele primers, and 1 min extension at 72°C, followed by a final elongation step at 72°C for 5 minutes. After the reaction was finished, PCR products were separated on a 1.5% agarose gel containing ethidium bromide (0.5 µg/ml) at 130 V for approximately 20 minutes in TAE (40 mM Tris acetate 1 mM EDTA) buffer using the 100 bp ladder (GeneDirex) as a size standard. The bands were visualized on an Alpha Imager 2000, and the results were interpreted based on comparison to the bands of known size in the ladder.

Table 2.1. Primers used for genotyping using PCR

Targeted allele	Primer ID	Primer sequence	Primer location	Product size	Direction
Hyal1 WT	WPG 612	5'-ctgggacagcaaggacattt-3'	*Hyal1* exon 2	340bp	Forward
Hyal1 WT	WPG 613	5'-cagtgctgcaggcaaataaa-3'	*Hyal1* exon 2	340 bp	Reverse
Hyal1 $^{-/-}$	WPG 610	5'-cttgggtggagagaggctattc-3'	Neo coding region	270 bp	Forward
Hyal1 $^{-/-}$	WPG 611	5'-aggtgagatgacaggagatc-3'	Neo coding region	270 bp	Reverse

2.4 *In vivo* micro-CT imaging

2.4.1 Scanning/ Image acquisition

In vivo micro-CT scanning was carried out using a high resolution *in vivo* scanner (Skyscan model 1176). Six months and one year old *Hyal1*$^{-/-}$ and control mice were anesthetised with 4% isoflurane and placed on the scanner bed in prone position, with the hind limbs stretched and fixed on the scanner bed with masking tape (Figure 2.1)**.** This extended the knee joint and prevented any movement while scanning. An eye lubricating gel (GenTeal, hypromellose lubricant, 0.3%) was applied to the animal's eye to prevent drying of the corneas during the scan. A whole body micro-CT scan was performed from the neck to the tail at a standard resolution of 35 μM to examine the shape of the bones. The femur bone of the mice was used for a high resolution scan at 9 μM for

quantification of bone density in comparison to phantom standards and analysis of three-dimensional bone micro-architecture.

The scans were performed using the following scanner settings: X-ray source voltage 50 kV, current 500 μA, 0.5 mm thick aluminium filter, frame averaging of 2, pixel size of 8.89 μm for high resolution and 35.57 μm for standard resolution images and rotation step 0.50^{o} for high resolution and 0.70^{o} for standard resolution, with a topographic rotation of 180^{o}. The total scan time for the whole body and femur was 35 and 20 minutes respectively. The animal was kept under anesthesia with the help of a nose cone which was connected to the gas and scavenging chamber simultaneously. Throughout scanning, the breathing rate of the animal was monitored on screen by capturing the signals produced by a small piece of styrofoam that was placed on its chest to detect the movement of the chest during respiration (Figure 5)**.** Calibration was performed each time a mouse was scanned by scanning phantom rods of known density (0.25 g/cm^3& 0.75 g/cm^3) provided with the micro-CT scanner, and using similar scanning parameters. These rods were made of calcium hydroxyapatite (CaHA) and thus imitate bones. To mimic the legs of mice, small phantom rods of 2 mm diameter were used immersed in water inside small Eppendorf tubes having a width approximately equivalent to the size of the animal's leg.

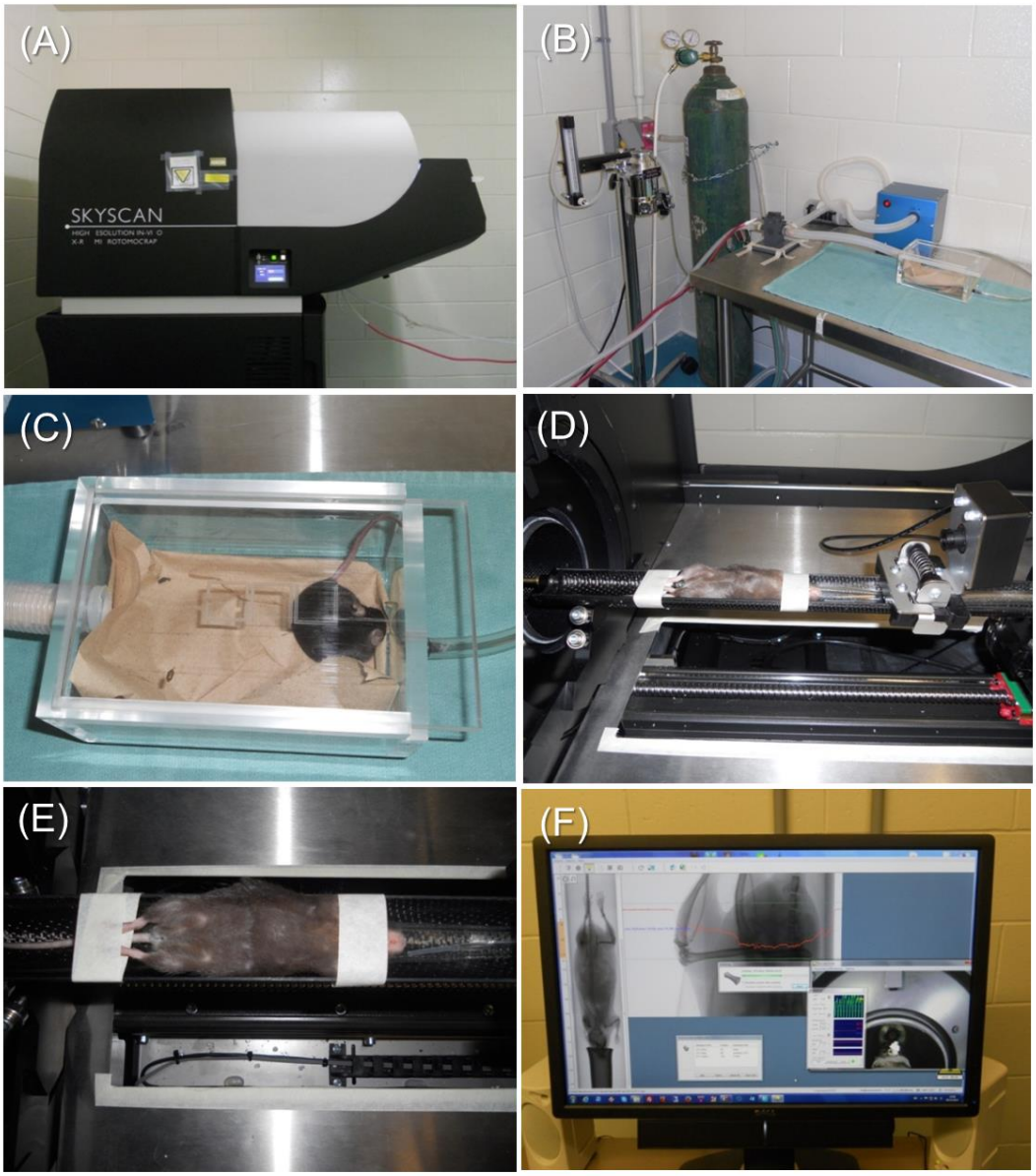

Figure 2.1: Steps involved in in vivo micro-CT imaging of the mouse hind limb: Panel A shows the micro-CT scanner from Skyscan, model number 1176 that was used to scan *Hyal1*$^{-/-}$ and control mice. Panel B shows the anaesthesia system with oxygen and isoflurane chambers. Panel C shows a mouse anaesthetised with 4% isoflurane in a chamber. Panel D shows a mouse placed on the scanner bed in prone position. Panel E shows the legs of the mouse being stretched and fixed on the scanner bed with masking tape. Panel F shows the screen on which the breathing and heartbeat of the mouse was monitored while scanning.

2.4.2 Image Processing

Reconstruction of scanned images

The cross sectional images (TIFF format) obtained after scanning were reconstructed using NRecon software based on the Feldkamp algorithm [98]. A stack of around 1500 to 2000 cross sections was reconstructed for both the whole body and femur keeping the following reconstruction parameters constant: Smoothing 2 using Gaussian kernel, beam hardening correction 30, ring artifact reduction 7, post alignment correction value varied for each image and was adjusted through the fine tuning option, dynamic image range from 0 to 0.088000, a value that gives best contrast of the image (Table 2.2). For reconstructing an image of the femur, a region of interest was selected that focussed on the knee joint. The size of the reconstructed images were 1000 x 668 and 4000 x 2672 pixels each for images of standard and high resolution respectively, and were stored as 8-bit BMP images (255 grey scales).

Table 2.2. Micro-CT reconstruction parameters

Parameters	**Value**	**Purpose**
Smoothing	2	Smooth each pixel and removes noise
Beam hardening correction	30%	Compensate for the preferential absorption of low energy X-rays by the outside of the object that leaves higher energy X-rays making the radiation more penetrating toward the opposite side of the object.
Ring artifact reduction	7	Compensate for the concentric ring like artifacts caused by imperfect detector elements that may over or underestimate the X-ray attenuation values
Post alignment	varied for each image and was adjusted through fine tuning option	Compensates any misalignment in the acquired image caused due to X-ray resolution, camera center or rotation.
Dynamic range	0.088000	Determines data dynamic range when converting real numbers into the output file format.

Defining Volume of Interest (VOI)

To orient all the images in similar directions, the dataset was first loaded in data viewer software. This gives a two dimensional view of reconstructed images in all three planes-transverse, coronal and sagittal. Images were straightened in each plane and then the oriented trans-axial image dataset was saved as new dataset. Using 3D data analysis software (CTAnalyser, version 1.13), on the stack of oriented reconstructed cross-sectional images of the femur, the growth plate was identified as a reference point which is a reproducible landmark. Bone mineral density was determined using either an automated processing scheme provided by the manufacturer, or by manual processing.

For manual processing, a region of interest (ROI) was drawn manually, on the binary page of the software, a specific distance away from the growth plate to form a volume of interest (VOI). For trabecular bone, the VOI was defined from the metaphysis, 200 cross sections away from the growth plate and consisted of 200 slices resulting in a height of 1.8 mm. For cortical bone, the VOI began 50 cross sections away from the last slice of trabecular VOI in the diaphysis region of the femur and consisted of 100 slices forming a height of 0.9 mm (Figure 2.2, Appendix A). In order to analyze the bone near the knee joint under the articular cartilage, a VOI was also chosen from the epiphysis, 80 slices (0.7 mm) above the growth plate for both trabecular and cortical bone**.** Similar to bone a VOI of 200 cross sections was made separately for each phantom. Finally these VOIs were used for bone mineral density (BMD) and 3-dimensional macro and micro architectural analysis of femur. For all the quantitative analysis, VOIs were delineated from the right femur of each mouse. Right leg was chosen randomly and kept constant for all types of measurements.

Segmentation / Thresholding

For the quantitative analysis of density and morphometric parameters, the grayscale images were segmented to black and white images to distinguish the mineralized bone tissue from the non-mineralized tissue. This was done through global thresholding on the binary page of CT Analyser (CTAn) software by adjusting the minimum threshold in the histogram to be the value that made the segmented image the best representation of the original structure. The maximum value was set to 255 as per the Skyscan manual. Since the trabecular bone of mice is very thin, it is difficult to separate the mineralized bone

from the non-mineralized marrow in micro-CT based studies. On the other hand, cortical bone being compact and denser than trabecular bone can easily be segmented to separate the mineralized bone from the neighbouring soft tissues. As a result segmentation was done only for cortical bone.

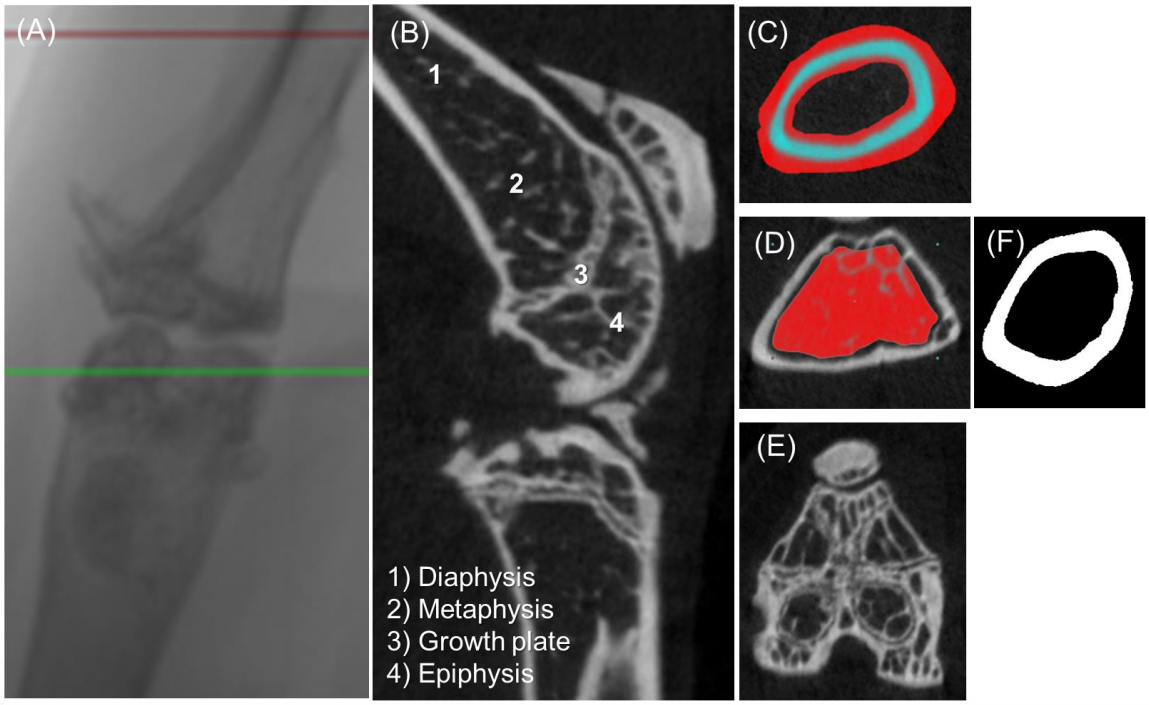

Figure 2.2: Image processing. Panel A: Image reconstruction, shows the image of the knee joint reconstructed using NRecon software. Panel B: Region of interest (ROI) and volume of interest (VOI) selection, the left image is an 8 bit grayscale view of the knee joint obtained after reconstruction of TIFF images. The top image on the right side highlights the ROI for cortical bone from the femoral diaphysis defined in the CTAnalyser software using the ROI tool. A set of ROIs from several consecutive cross sections were used to make a VOI for cortical bones from which measurements were made. The middle image on the right side highlights the ROI for trabecular bone from the femoral metaphysis defined by the CTAnalyser software using ROI tool. A set of ROIs from several consecutive cross sections were used to make a VOI for trabecular bones from which measurements were made. The bottom image on the right side shows the cross section of growth plate, which was considered as a reference point for defining metaphysis and diaphysis in order to select VOIs for trabecular and cortical bone

respectively. Panel C: Segmentation, shows the segmented cortical image with mineralized bone in white and non-mineralized bone in black.

2.4.3 Image Analysis

Whole mouse 3-dimensional bone macro architecture

The reconstructed cross sectional image dataset of the whole mouse skeleton scanned at standard resolution was loaded in CTVox (version 2.2) software to view a 3-D model of the whole skeleton of *Hyal1*$^{-/-}$ and control mice to look for any abnormalities in shape and structure of bones. The bones were analyzed for broad zygomatic arches, thickened digits and ribs, narrowing of the rib cage, spinal stenosis and an angled calcaneus as has been previously found in other MPS mice [14, 13].

Femur 3-D bone macro architecture (3-D rendered model)

Joints being the site of HA occurrence [34] and knee joint involvement being common in MPS IX human patients and mice [25, 24, 97], a high resolution scan of femur was used to generate a 3-D rendered model of each knee joint, in order to look for any abnormality in its structure compared to the structures of *Hyal1*$^{-/-}$ mice and controls. These three dimensional images were constructed by loading the reconstructed cross sectional image dataset from the femur ROI in CTVox (version 2.2, BMP file format) and CT Volume (version 2, P3G file format, double time cubes algorithm) software. Each ROI was visually examined in transverse, coronal and sagittal slices and rotated whenever required to compare *Hyal1*$^{-/-}$ and controls. Similar volume rendered three dimensional models were also constructed from cortical and trabecular VOI of *Hyal1*$^{-/-}$ and control mice to

look for any qualitative differences in thickness of cortical bone or porosity of trabecular bone.

Bone mineral density (BMD) and tissue mineral density (TMD) assessment

Using CTAn software, trabecular and cortical density were calculated from their respective processed VOI which was delineated by both manual and automatic custom processing methods from the mouse femur. This began with the calculation of the attenuation coefficient from the VOI of each phantom and entering the data into the formula for the calculation of BMD which completes the calibration of density against the attenuation coefficient. As trabecular bone was considered as a whole in combination with the bone marrow, the density calculated from trabecular VOI was termed as bone mineral density (BMD). On the contrary, the density calculated from compact and completely mineralized cortical VOI was termed as tissue mineral density (TMD). After calibration the X-ray absorption through the segmented trabecular and cortical VOI of femur were compared with the X-ray absorption of phantoms to calculate the BMD and TMD respectively. A similar method was used to calculate both trabecular BMD and cortical TMD from the epiphysis region of the femur near joints.

Trabecular & cortical bone microarchitecture assessment

For the assessment of bone microarchitecture, morphometric parameters of trabecular and cortical bone were calculated from the segmented VOIs following the protocol as described in the Skyscan manual which was based on the marching cube method [99]. Three dimensional morphometric parameters calculated from the trabecular region of the

femur metaphysis were bone volume fraction, trabecular bone pattern factor, trabecular thickness, trabecular separation, trabecular number and connectivity density. The key parameters calculated to describe the bone structure of the cortical bone from femur diaphysis included periosteal and endosteal perimeters, volumes and cortical thickness (Table 7) [100–103].

Table 2.3. Description of trabecular and cortical morphometric parameters

Bone volume fraction (BV/TV) (%)	Proportion of total tissue volume
Trabecular bone pattern factor (Tb.Pf, mm^{-1})	Inverse index of trabecular connectivity
Trabecular thickness (Tb.Th, mm)	Average width of trabecular bone
Trabecular Separation (Tb.Sp, mm)	Thickness of non-bone part between trabeculae
Trabecular Number (Tb.N, mm^{-1})	Number of trabecular bone per unit length
Connectivity Density (Conn. Den, mm^{-3})	3-D connectivity of trabeculae normalized by TV
Periosteal Perimeter (Pe.Pm, mm)	Surface area covered by the periosteum
Periosteal Volume (Pe.V, mm^3)	Volume inside periosteum
Endosteal Perimeter (En.Pm, mm)	Surface area covered by the endosteum
Endosteal Volume (En.V, mm^3)	Volume inside endosteum
Cortical thickness (Ct.Th, mm)	Average width of cortical bone

Standardized nomenclature of histomorphometric parameters, from the ASBMR (the American Society of Bone and mineral Research)

Tibia and femur length

The femur and tibia have been used for quantitative analysis of bone length in a large number of studies [101, 104–107]. This may be because both trabecular and cortical bone parameters can be easily calculated from long bones. Also there has been a study showing the mouse femur as an ideal bone for accurate and precise measurements [108]. Therefore, the femur was chosen for all quantitative studies. To evaluate if the measured

parameter has any correlation with femoral length and to see if there is any evidence of short stature as seen in MPS IX patient and other MPSs patients, right legs were measured to calculate tibia and femur length for each mouse using the measuring tool in data viewer software.

2.5 Histology

2.5.1 Dissection and skeletal tissue fixation

After the scanning was complete, eye lubricating gel was again applied to the eyes of the animal to prevent drying and they were placed back into the cage for recovery from the anaesthesia. *Hyal1*$^{-/-}$ and their controls were then euthanized using 25% Isoflurane (Baxter Corporation) in propylene glycol (Amresco) and dissected immediately. Heart, lungs, liver, spleen and kidney were collected and stored at -80^{o}C for future studies, if required. Skeletal tissues, including knee joint, hip joint, spine, ribs, paws and feet were gradually dissected, muscles surrounding them were carefully removed, and the tissues were fixed in paraformaldehyde lysine periodate (PLP) fixative (0.01M periodate, 0.075M lysine, 0.0375M sodium phosphate buffer and 2% paraformaldehyde, pH 7.4) at room temperature for 1 hour and then at 4^{o}C overnight. The following morning the tissues were washed three times for 10 minutes each with PBS (Phosphate buffered saline). Joints were then decalcified with Immunocal, a formic acid commercial decalcifier (American master tech) at 4^{o}C overnight and stored in 70% ethanol until processing.

2.5.2 Tissue Processing, embedding and microtomy

Tissues were processed using a Citadel 1000 tissue processor under vacuum which included dehydration with 70%, 95% and 100% alcohol for 1, 2 and 5.5 hours respectively; infiltration with xylene which is a clearing agent for 3 hours and finally introduction of paraffin wax into the tissue for 3 hours before embedding them into paraffin blocks in coronal orientation using a Histocentre 3 embedder. These paraffin blocks were stored for future studies.

2.6 Statistics

Descriptive statistics (mean & standard deviation) were used to compare BMD, TMD and morphometric parameters of *Hyal1*$^{-/-}$ with controls. Difference was analysed using an unpaired student's t-test at significance level $p<0.05$. These statistical analyses were done using MS Excel.

Chapter 3

Results Part 1: Qualitative Analysis

3.1 Description of 3-D macro-architecture of *Hyal1*$^{-/-}$ and control mice

3.1.1 Description of whole mouse 3-D macro-architecture scanned at standard resolution

Hyal1$^{-/-}$ and control (*Hyal1*$^{+/+}$ or *Hyal1*$^{+/-}$) mice were maintained in Central Animal Care until they reached 6 months or one year of age. Grossly, HYAL1-deficient mice appeared completely normal, and indistinguishable from their control littermates. Further, their movements appeared normal. To follow up the findings from the previous study [97] which showed a joint phenotype, the whole body skeleton of *Hyal1*$^{-/-}$ and control (*Hyal1*$^{+/+}$ or *Hyal1*$^{+/-}$) mice was examined using micro-CT to look for obvious abnormalities in bone shape and structure. In other mouse models of MPSs, abnormal skeletal findings have included broad zygomatic arches, skull enlargement, blunted nose, thickened digits, shortened long bones, wavy or oar shaped ribs, narrowing of the ribcage, spinal stenosis and angled calcaneus [14, 13]. A 3-D model of the whole mouse skeleton of *Hyal1*$^{-/-}$ and control mice was generated from a standard resolution scan at six months and one year of age. These analyses were performed on both male and female mice at 6 months and 1 year of age.

No obvious abnormalities in the shape and structure of the bones were found when the images from the *Hyal1*$^{-/-}$ mice were compared to those of normal controls.

There was no noticeable difference in the appearance of the skull, or thickness of the zygomatic arches, clavicles, ribs, vertebrae, pelvis, fore limbs and hind limbs of *Hyal1*$^{-/-}$ mice compared to controls suggesting no skeletal dysplasia was present. A representative pair of one year old male *Hyal1*$^{-/-}$ and *Hyal1*$^{+/+}$ mice is shown in Figure 3.1.

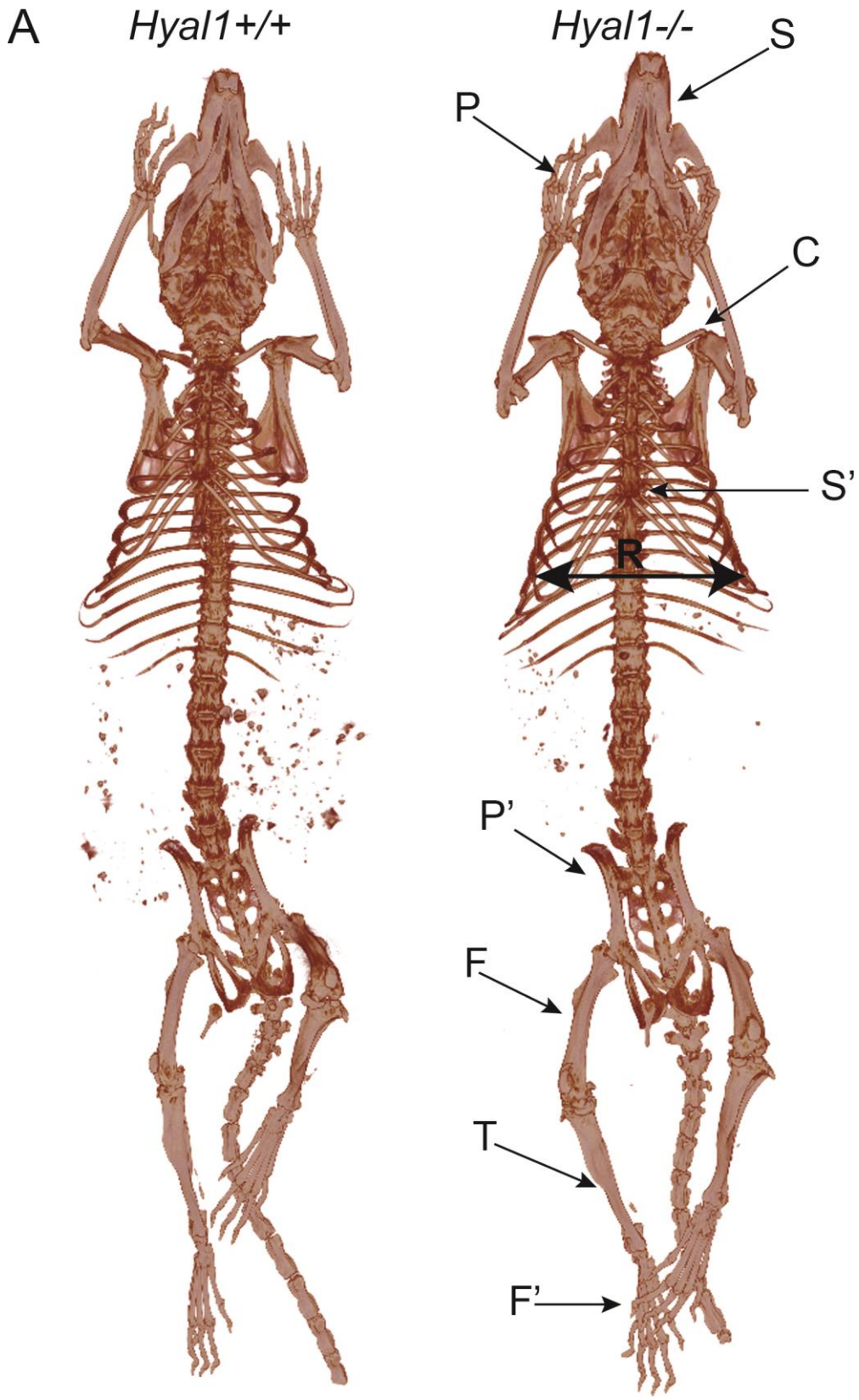
A
Hyal1+/+
Hyal1-/-
S
P
C
S'
R
P'
F
T
F'

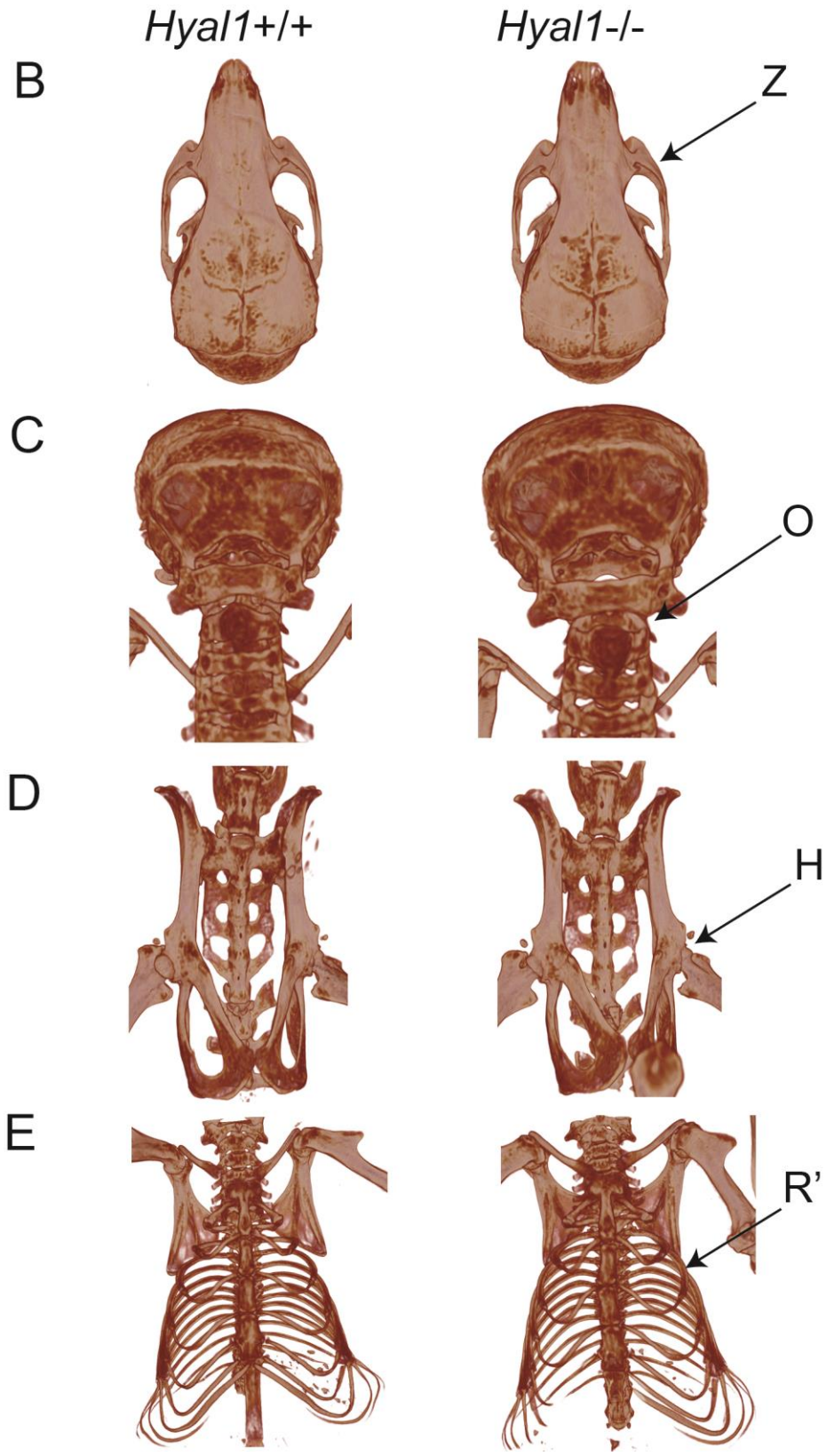
Hyal1+/+
Hyal1-/-
B
Z
C
O
D
H
E
R'

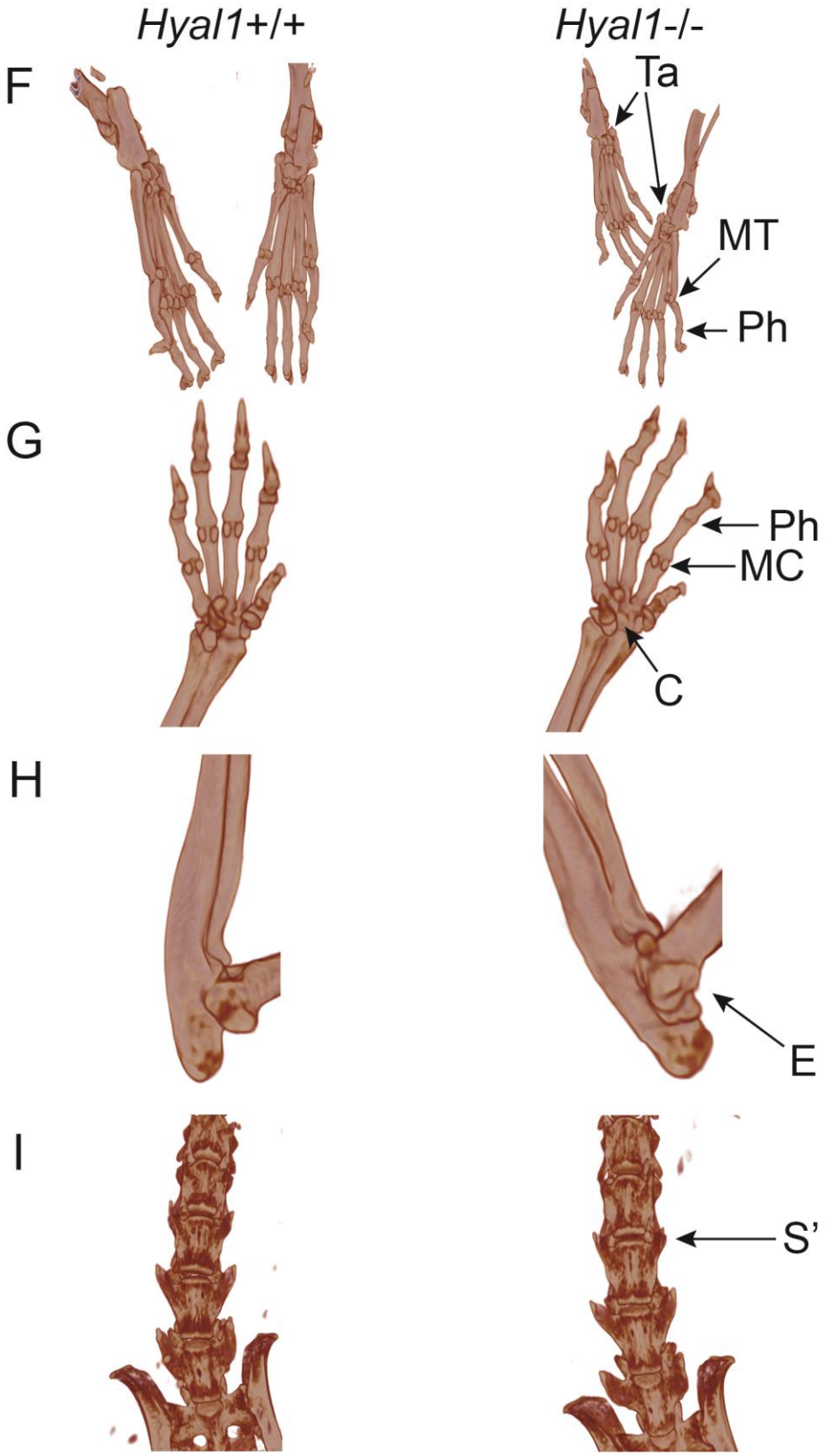
Hyal1+/+
Hyal1-/-
F
Ta
MT
Ph
G
Ph
MC
C
H
E
I
S'

Figure 3.1. **Representative 3-D images of the skeleton of a *Hyal1*$^{-/-}$ and *Hyal1*$^{+/+}$ male mouse:** Images of the mouse skeleton were obtained by micro-CT scanning at 35 µm resolution, and reconstructed using NRecon software. CTVox software was used to generate the colour-coded 3-D reconstruction. Colour-coding was chosen to provide a clear view of any outgrowths, if present. Comparison between *Hyal1*$^{-/-}$ and *Hyal1*$^{+/+}$ mice: (A) A ventral view of the whole mouse skeleton (B) A dorsal view of the skull (C) A dorsal view of the spine showing the odontoid process. (D) A ventral view of the pelvis including the hip joint and (E) A ventral view of the ribs. (F) An anterior view of the hind limb showing tarsals (Ta), metatarsals (MT) and phalangeal (Ph) joints. (G) An anterior view of the paw indicating carpal and metacarpal joints. (H) A dorsal view of elbow joint. (I) A ventral view of spine. Arrows indicate features that were examined and compared in these images of *Hyal1*$^{+/+}$ and *Hyal1*$^{-/-}$ mice, S= Skull, O= Odontoid process, *Z*= zygomatic arches, R= Ribcage, R'= Ribs, C= Clavicles, S'= Spine, H= Hip, P'= Pelvis, F= Femur, T= Tibia, P=Paws, F'= Feet, E = Elbow, Ta= Tarsals, MT= Metatarsals, Ph= Phalanges, C= Carpals, MC= Metacarpals. No obvious abnormality was seen in the structure and shape of the bones in the *Hyal1*$^{-/-}$ mice compared to controls. This is a representative image of 5 pairs of male mice aging both 6 months (n=2) and 1 year (n=3). These images are not to scale.

In addition to colour-coded images generated through software manipulations, we examined traditional grayscale micro-CT images which are a combination of 2^8 (256) different shades of black and white. Grayscale images of the whole body skeletons of *Hyal1*$^{-/-}$ and controls (*Hyal1*$^{+/+}$ or *Hyal1*$^{+/-}$), which resemble radiographs, were compared. These images were examined to detect differences in the radiodensity of the legs, spine, ribs, skull, digits, or thickened and sclerotic bones as have been seen in other MPS animals. Both male and female mice at 6 months and 1 year were analyzed. Similar to the colour-coded images, comparison of the grayscale images of the whole body showed no detectable difference in the image intensity, suggesting no abnormal calcification of bones in HYAL1-deficient mice compared to controls. This was specifically examined in the skull, zygomatic arches, ribs, vertebrae, humerus, radius and digits of fore limbs and femur, tibia and digits of hind limbs. A representative pair of one year old male *Hyal1*$^{-/-}$ and *Hyal1*$^{+/+}$ mice is shown in Figure 3.2.

A detailed description of the skeletal features of MPS IX mice at six months and one year of age compared to other MPS mice is summarized in Table 3.1 [12–15]. The skeletal system is severely affected in MPS II, MPS VII and MPS I mouse models compared to MPS IV, MPS VI and MPS IX. The absence of grossly detectable skeletal abnormalities in MPS IX mice is clear evidence that this disorder is comparatively milder than other MPSs, as was suggested in the previous study.

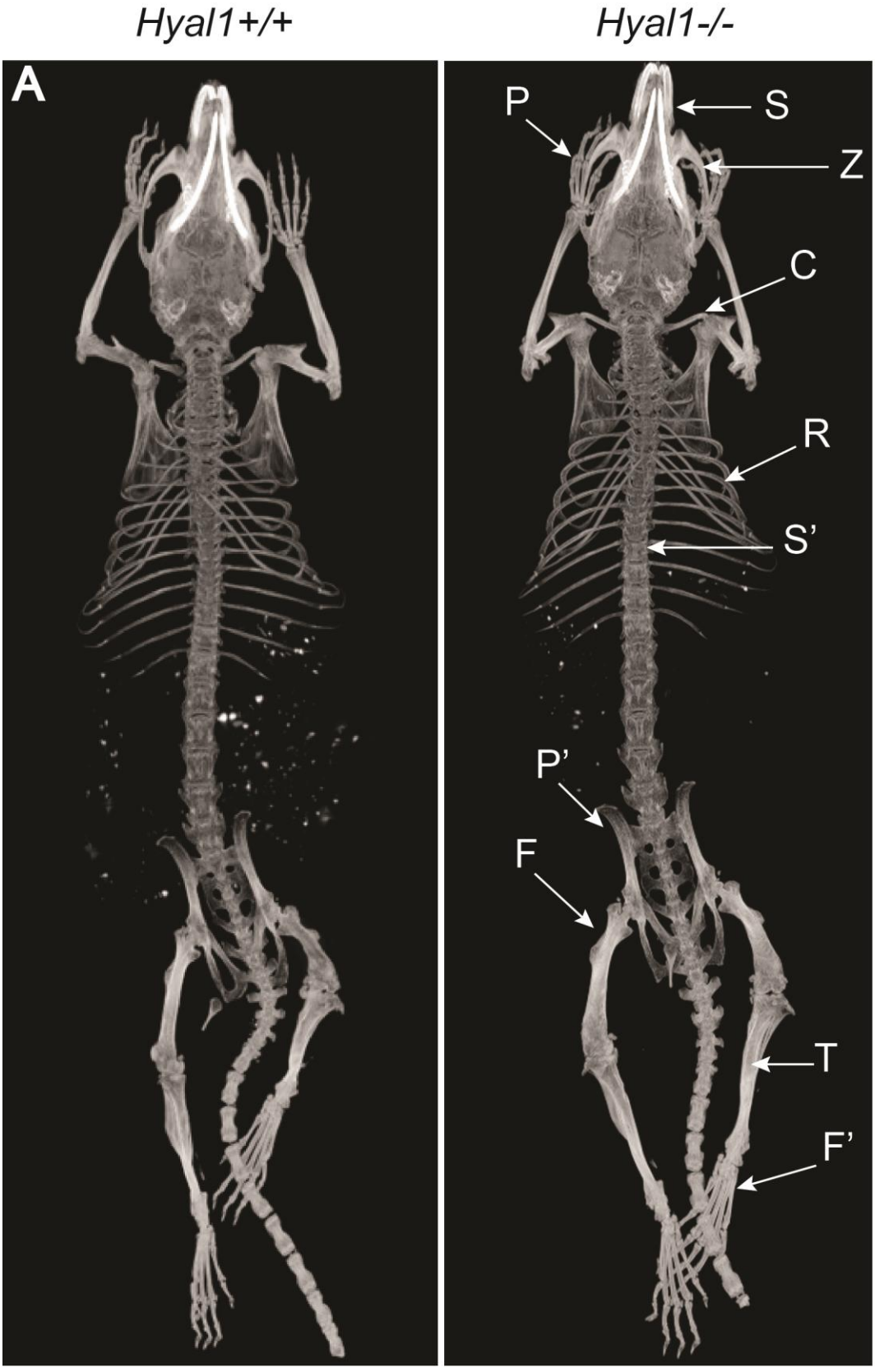
Hyal1+/+
Hyal1-/-
A
P
S
Z
C
R
S'
P'
F
T
F'

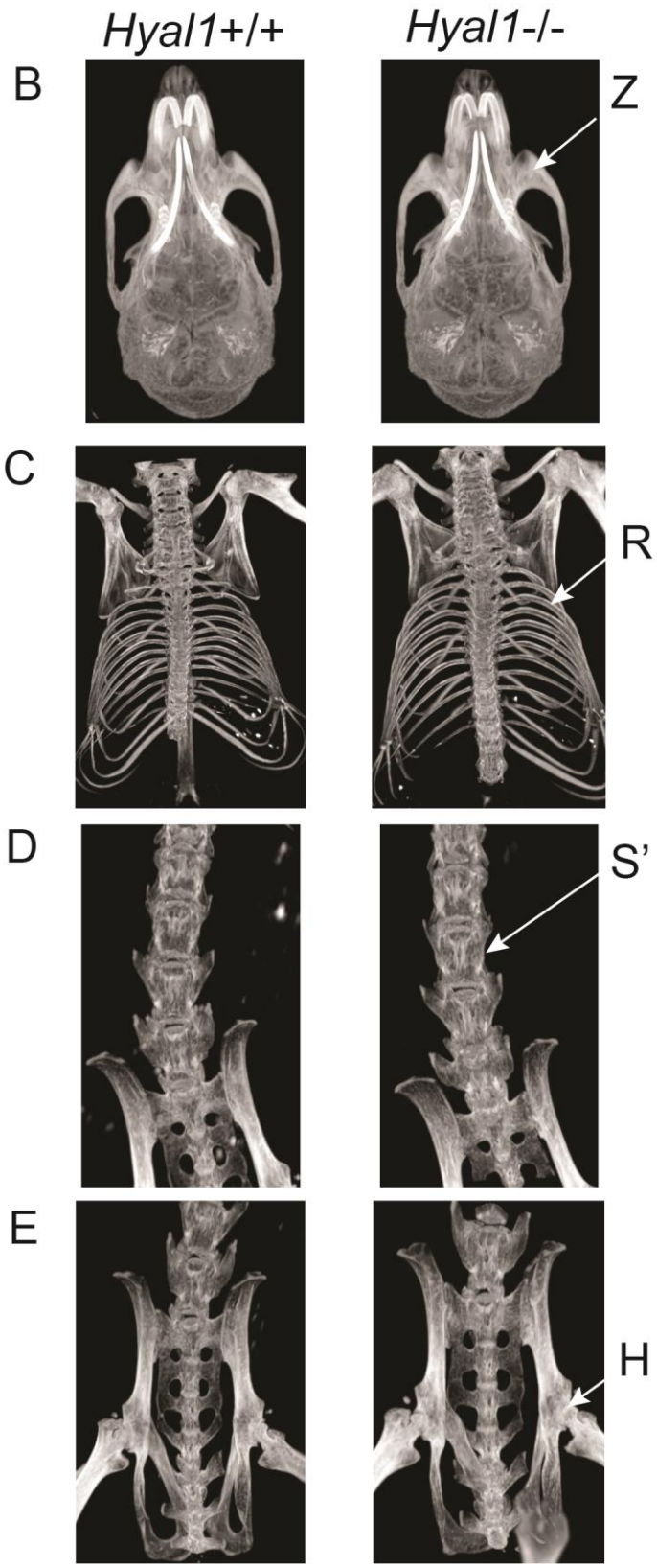
Hyal1+/+
Hyal1-/-
B
Z
C
R
D
S'
E
H

Figure 3.2. Representative 3-D grayscale images of the skeleton of a *Hyal1*$^{-/-}$ and *Hyal1*$^{+/+}$ mouse: Images of the mouse skeleton were obtained from micro-CT scanning at 35 µm resolution, reconstructed using NRecon software, and manipulated in CTVox software to generate the 8 bit grayscale 3-D image**.** The darkest shade is black, which has a value of 0 and represents total transmission of X-rays obtained from soft tissues. The lightest shade is white, with a value of 255, and represents total absorption obtained from dense tissues like bone. Comparison between *Hyal1*$^{-/-}$ and *Hyal1*$^{+/+}$ (A) A ventral view of the whole mouse skeleton, (B) A ventral view of the skull, (C) A ventral view of the ribs, (D) A dorsal view of the spine (E) A ventral view of the pelvis including hip joint, (E) A dorsal view of the feet and (F) A dorsal view of the spine. Arrows indicate features that were examined in these images S= Radiodensity of skull, Z= Thickness of zygomatic arches, R= Thickness of ribcage, C= Thickness of clavicles, S'= Spinal sclerosis, H= Hip sclerosis, F= Thickness and sclerosis of the femur, T= Thickness and sclerosis of the tibia, P=Thickness of the paws, F'= Thickness of the feet. No difference was detected in radiodensity of bones in *Hyal1*$^{-/-}$ compared to controls. This is a representative image of all 12 animals that were scanned including 6 months (n=6) and 1 year of age (n=6). These images are not to scale.

Table 3.1.Presence of skeletal findings in various mouse models of MPSs and its comparison with MPS IX mice

Skeletal Features	MPS IX	MPS I	MPS II	MPS III	MPS IV	MPS VI	MPS VII
Axial Skeleton							
Skull							
Flattened facial features	-	+	-	-	-	+	+
Blunted nose	-	+	-	-	-	-	+
Thickening of facial bones	-	-	-	-	-	-	-
Broad zygomatic arches	-	+	+	-	-	-	+
Enlarged skull bone/ Calvaria enlargement	-	+	+	-	-	+	-
Calvaria sclerosis	-		+	+	-	-	+
Ribs							
Anterior flaring of ribs (oar like)	-	+	-	-	-	-	+
Thickening of ribs	-	-	+	-	-	+	-
Narrow ribcage	-	-	-	-	-	-	+
Vertebrae							
Spinal stenosis (Narrowing of spinal canal)	-	+	-	-	-	-	+
Appendicular skeleton							
Clavicle enlargement	-	-	-	-	-	+	-
Pelvic abnormality	-	-	-	-	-	+	-
Thickening of digits	-	+	+	-	-	-	+
Thickening of fibulae	-	+	+	-	-	-	-
Shortened extremities	-	-	-	-	-	+	+
Femur sclerosis		-	+	-	-	-	+
Tibia sclerosis		-	+	-	-	-	+
Angled calcaneus	-	-	+	-	-	-	-
Femur enlargement	-	-	+	-	-	-	-
Tibia enlargement	-	-	+	-	-	-	-
Joints							
Periosteal bone formation	+	+	+	-	-	-	-
Joint deformation	+	-	+	+	-	-	+

3.1.2 Description of femur & knee joint macro-architecture

To continue and extend previous work that showed pathology in knee joints associated with HA accumulation, and due to the major involvement of joints in MPS IX patients,

the knee joint of the hind leg and the surrounding mid and distal femur and proximal tibia were chosen for high resolution (9 µm) micro-CT scanning. High resolution analysis allows the details in the structure of a sample to be visualized. The right hind leg joint of *Hyal1*$^{-/-}$ and controls (*Hyal1*$^{+/+}$ or *Hyal1*$^{+/-}$) were compared in both male and female mice at 6 months and one year of age. Skeletal abnormalities, including thickening of the long bones, sclerotic femur or tibia and periosteal bone formation, have previously been observed in other MPS mouse models [12, 15].

The resulting 3-D images from high resolution micro-CT scans of knee joints of 2 pairs of male and 4 pairs of female mice examined at 6 months of age, didn't show any noticeable abnormalities or differences in the joint structure between *Hyal1*$^{-/-}$ mice and their age matched controls (*Hyal1*$^{+/+}$ and *Hyal1*$^{+/-}$).

High resolution micro-CT scans of 1 year old male mice (n=3) demonstrated abnormal periosteal bone formation at the distal femur near the knee joint in two, of three, *Hyal1*$^{-/-}$ mice, but not controls. Cross sectional images of these joints also showed a thickened periosteum at the distal femur and the proximal tibia. The knee joint of a representative male *Hyal1*$^{-/-}$ and *Hyal1*$^{+/+}$ control is shown in Figure 3.3. Though such formations were absent in one male, an uneven surface at and above the knee joint was apparent at the distal femur. Periosteal bone formation has also been seen in two other MPS models and thus can be considered as symptomatic evidence of MPS [13, 14]. Likewise, knee joints of one year old females (n=3) were also scanned at 9 µm resolution. Though periosteal formations were absent in one year old female counterparts, an uneven surface at the knee joint was apparent in one, of three pairs, while the other two pairs

didn't show any differences between *Hyal1*$^{-/-}$ and control mice. Knee joints of one year old female *Hyal1*$^{-/-}$ and control mice are shown in Figures 3.4 and 3.5.

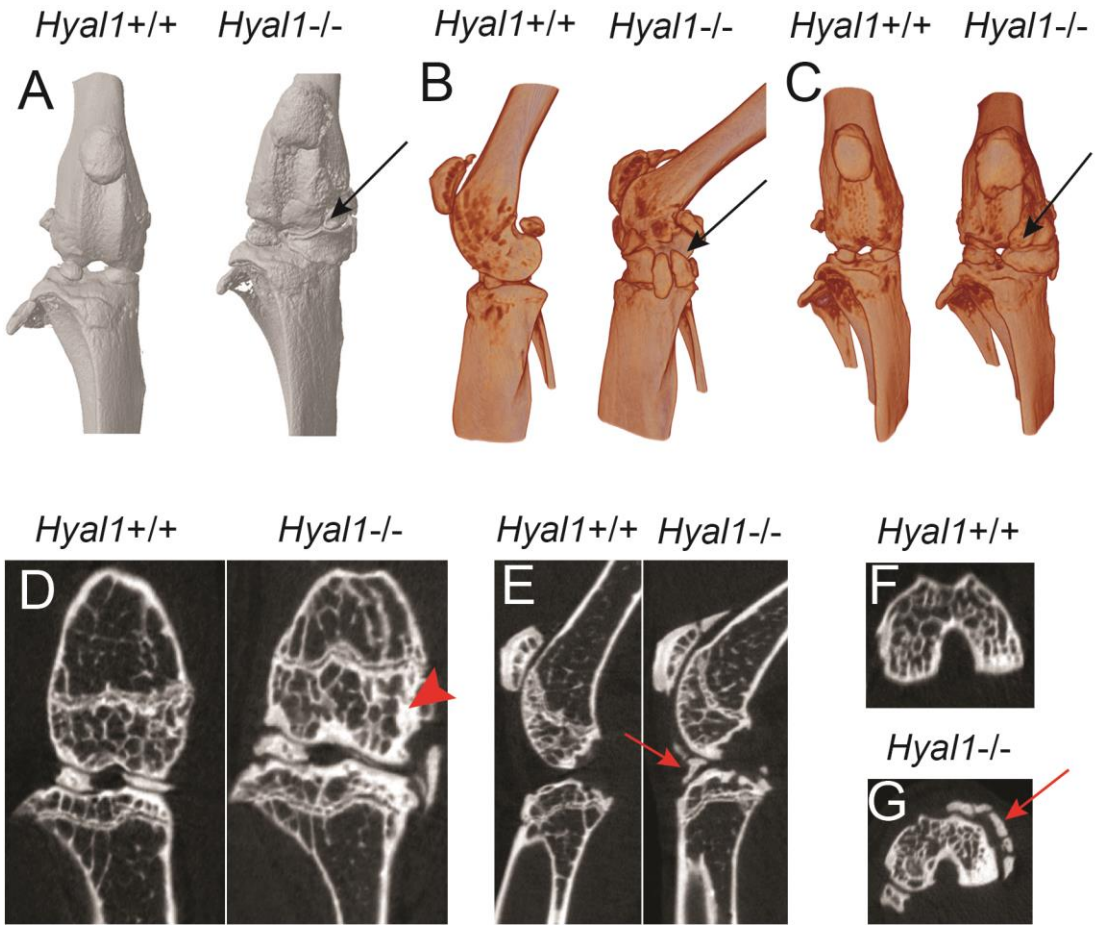

Figure 3.3. Representative micro-CT images of the right hind leg joint in a *Hyal1*$^{-/-}$ and *Hyal1*$^{+/+}$ male mouse at 1 year of age: The upper row shows the 3-D micro-CT images of the knee joint, with maximum extension, obtained by micro-CT scanning at 9 µm resolution, and reconstructed using NRecon software. (A) A ventral view of a volume-filled image obtained by loading a reconstructed image into CTVol software. (B) A ventral view of a colour-coded volume-filled image obtained by loading a reconstructed image into CTVox software. (C) A lateral view of a colour-coded volume-filled image obtained by loading a reconstructed image into CTVox software. Black arrows show abnormal extra bone formation on the distal femur of *Hyal1*$^{-/-}$ mice**.** These images are not to scale. Bottom row shows 2-D cross-sectional slices of the knee joint with (D) coronal, (E) saggital and (F, G) transaxial orientation respectively. F and G show a 2-D slice of the knee joint showing transaxial views of growth plate and epiphysis, respectively. Red arrowhead denote increased bone thickness and thin red arrows show extra periosteal bone formation in a *Hyal1*$^{-/-}$ mouse compared to an age matched control. This is a representative image of two of three pairs of male mice.

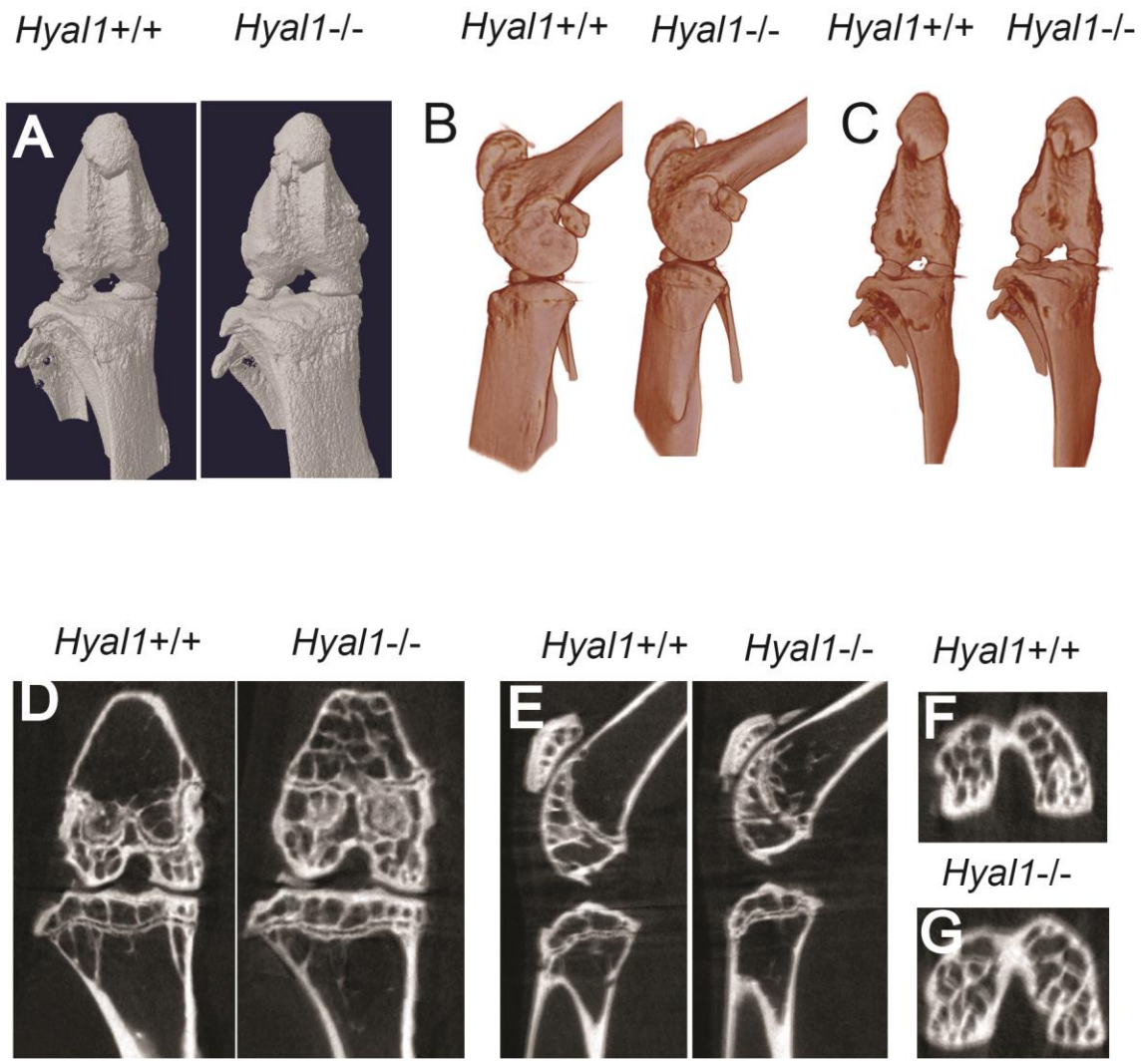

Figure 3.4. Representative micro-CT images of the right hind leg joint in *Hyal1*$^{-/-}$ and *Hyal1*$^{+/-}$ female mouse at 1 year of age: The top row shows the 3-D micro-CT images of knee joint obtained by micro-CT scanning at 9 µm resolution and reconstructed using NRecon software. (A) A ventral view of a volume-filled image obtained by loading a reconstructed image into CTVol software. (B) A ventral view of a colour-coded volume-filled image obtained by loading a reconstructed image into CTVox software (C) A lateral view of colour-coded volume-filled image obtained by loading a reconstructed image into CTVox software. No difference was seen in the volume-filled 3-D images of *Hyal1*$^{+/+}$ mice compared to controls. These 3-D images are not to scale. Bottom row shows 2-D cross-sectional slices of the knee joint with (D) coronal, (E) sagittal and (F, G) transaxial orientation respectively. No prominent difference in the thickness, or abnormal bone growth, is observed in *Hyal1*$^{-/-}$ compared to control mice. This was seen in two of three pairs of female mice.

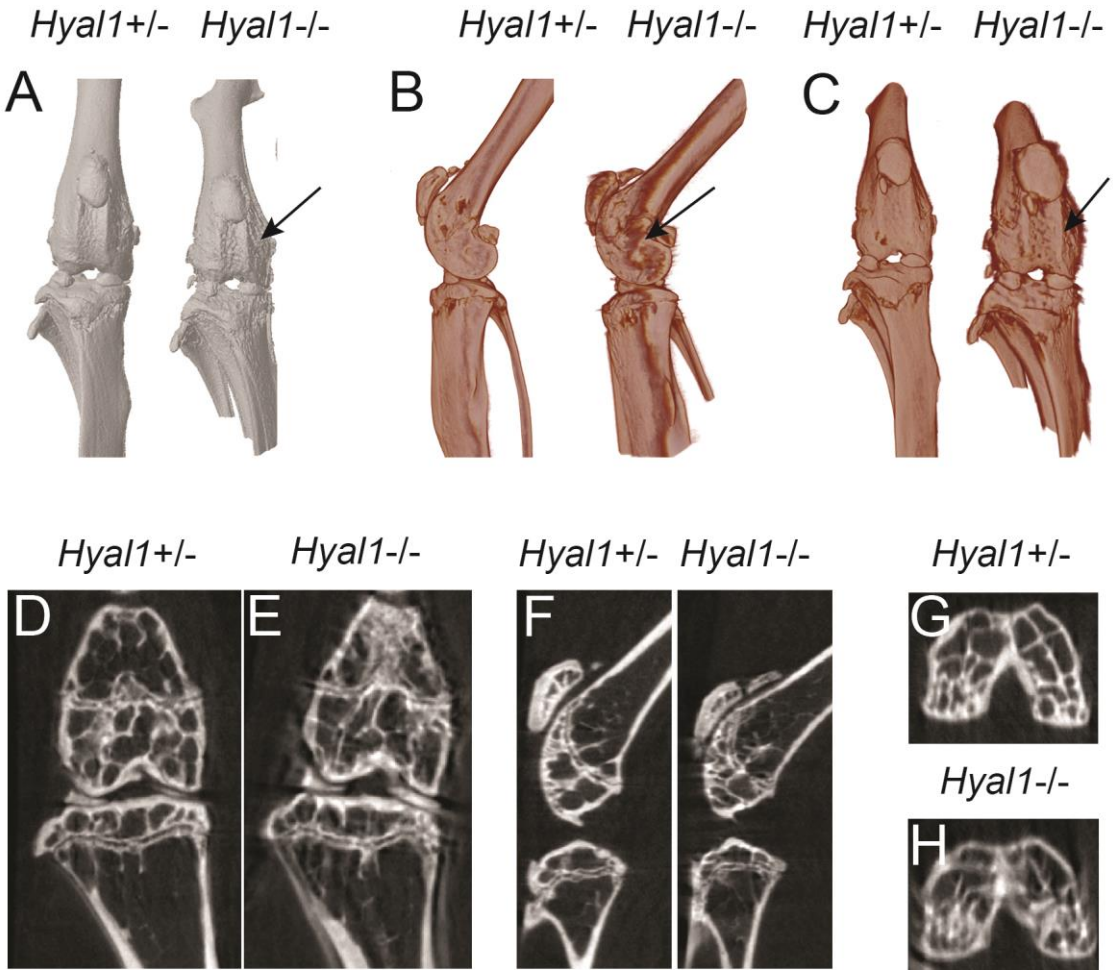

Figure 3.5. **Representative micro-CT images of the right hind leg joint in one of the *Hyal1*$^{-/-}$ and *Hyal1*$^{+/-}$ female mouse at 1 year of age:** The top row shows the 3-D micro-CT images of knee joint obtained by micro-CT scanning at 9 µm resolution and reconstructed using NRecon software. (A) A ventral view of a volume-filled image obtained by loading a reconstructed image into CTVol software. (B) A ventral view of a colour-coded volume-filled image obtained by loading a reconstructed image into CTVox software (C) A lateral view of colour-coded volume-filled image obtained by loading a reconstructed image into CTVox software. Black arrows shows an uneven surface on the distal femur of a *Hyal1*$^{-/-}$ mouse near the joint in the volume filled images**.** This was seen in only in one of the three pairs of female mice. These 3-D images are not to scale. Bottom row shows 2-D cross-sectional slices of the knee joint with (D) coronal, (E) sagittal and (F, G) transaxial orientation respectively. No prominent difference in the thickness, or abnormal bone growth, is observed in *Hyal1*$^{-/-}$ compared to control mice.

3.1.3 Description of other joints scanned at high resolution

As described in the previous section, only the area around the knee joints was scanned at high resolution for 1 year old male mice. After observing the periosteal bone formation in the male mice, other joints were scanned in 1 year old female mice whose time point was reached later. Additional joints that were scanned at high resolution included the tarsals, tibiotarsals, hip joints and cervical vertebrae (odontoid process). High resolution scans of different joints from a representative pair of one year old female mice is presented in Figure 3.6**.** Qualitative evaluation of other joints did not reveal any abnormal growths, suggesting the knee is the primary affected area in MPS IX mice. However, differences might have been observed if we had scanned the joints from one year old male *Hyal1*$^{-/-}$ mice.

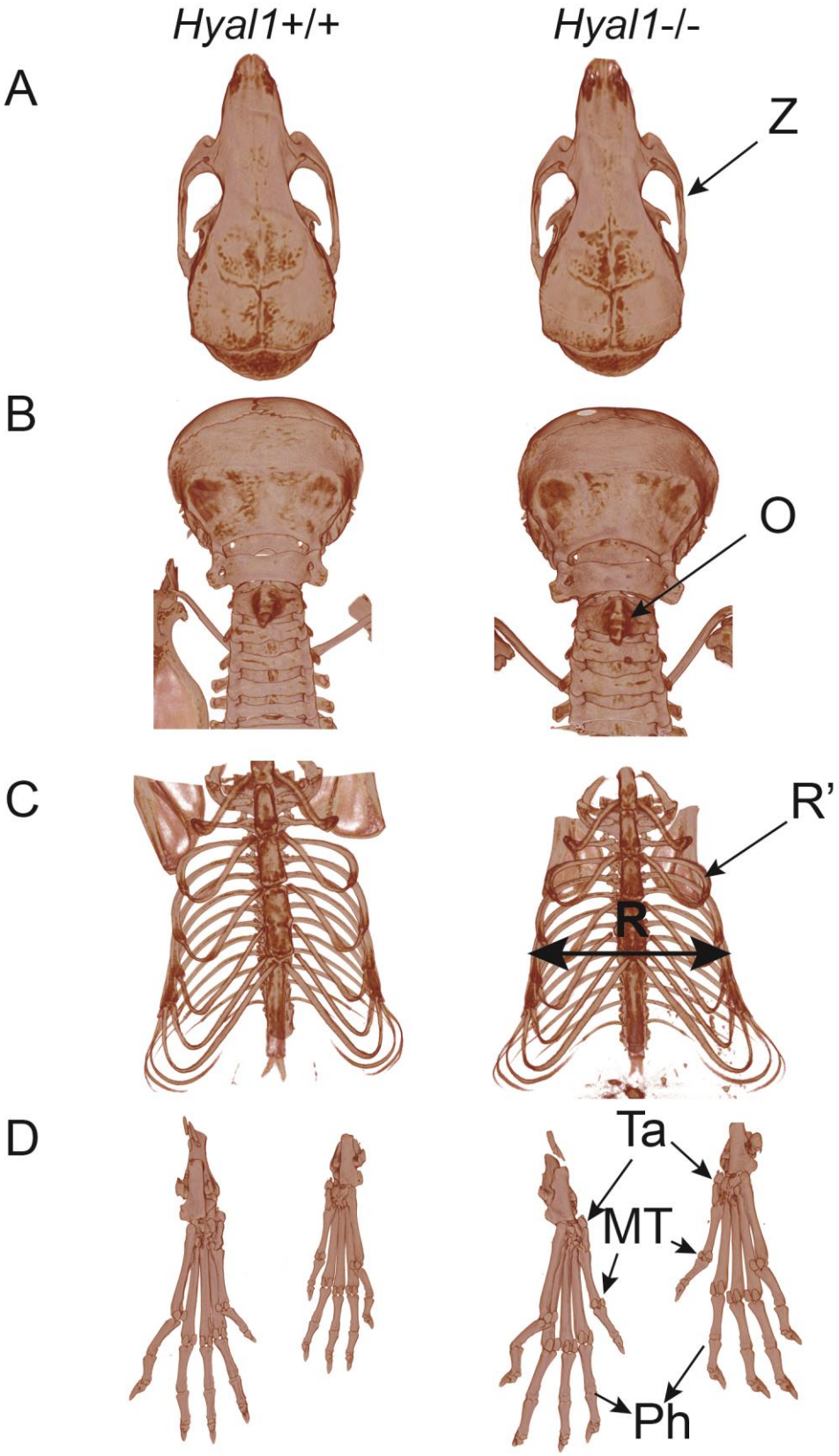
Hyal1+/+
Hyal1-/-
A
Z
B
O
C
R'
R
D
Ta
MT
Ph

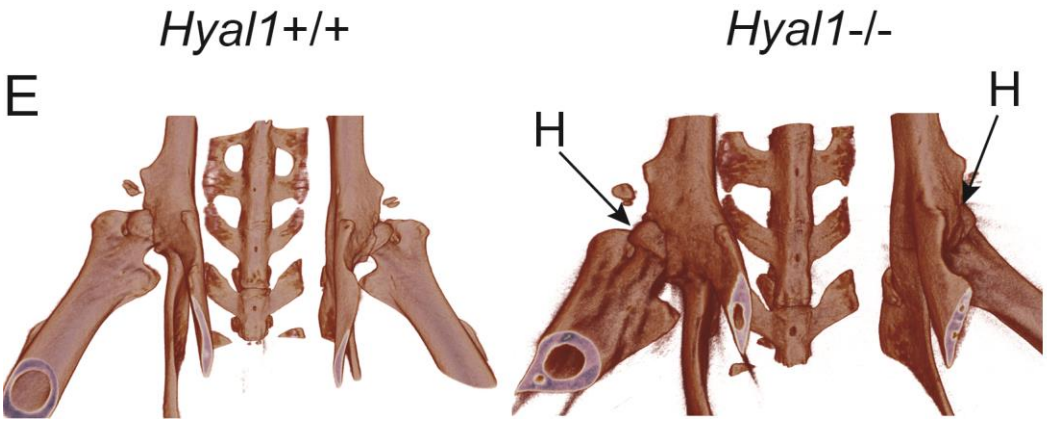

Figure 3.6. Representative high resolution colour-coded 3-D images of the skeleton of 1 year old female *Hyal1*$^{-/-}$ and *Hyal1*$^{+/+}$ control mice: Images of the mouse skeleton were obtained from micro-CT scanning at 9 µm resolution and reconstructed using NRecon software, followed by CTVox software to generate the colour-coded 3-D reconstruction. Colour-coding was selected to provide clear view of any outgrowths, if present. Comparison between *Hyal1*$^{-/-}$ and *Hyal1*$^{+/+}$ controls mice: **(**A) A dorsal view of the skull. (B) A dorsal view of the cervical vertebrae (odontoid process). (C) A ventral view of the ribcage. (D) An anterior view of the hind feet showing tarsals (T), metatarsals (MT) and phalanges (P). (E) A ventral view of pelvis showing hip joint (H). Arrows indicate features that were examined in these images. High resolution scans of different joints didn't show any abnormalities in the *Hyal1*$^{-/-}$ mice compared to controls. Z= Zygomatic arches, O= Odontoid process, H= Hip, Ta=Tarsal joints, MT=Metatarsals, P=Phalanges. These are representative of 3 sets of mice. Images are not to scale.

3.1.4 Description of macroarchitecture of different joints in young mice

All four MPS IX patients were diagnosed at a young age with skeletal symptoms. Given that knee joint abnormalities were present in 1 year *Hyal1*$^{-/-}$ mice, we decided to perform high resolution micro-CT scans on two additional sets of female mice at 6 weeks and one male mouse pair at 3 months of age. Different joints of one pair of 6 week old

Hyal1$^{-/-}$ and control mice are shown in Figure 3.7. These images were examined for abnormalities like periosteal bone formation in the joints of the hind and fore limbs; scoliosis and kyphosis in the spine; periosteal bone formation in the joints between tarsals, metatarsals, carpals, metacarpals, phalanges and dysplasia in the hip joint. No detectable difference was observed in any of the joints.

The knee joint of the 3 month old male mice was scanned *ex vivo*; a prominent rough surface at the distal femur was observed in the *Hyal1*$^{-/-}$ mouse which was not observed in a normal heterozygous control mouse (Figure 3.8).

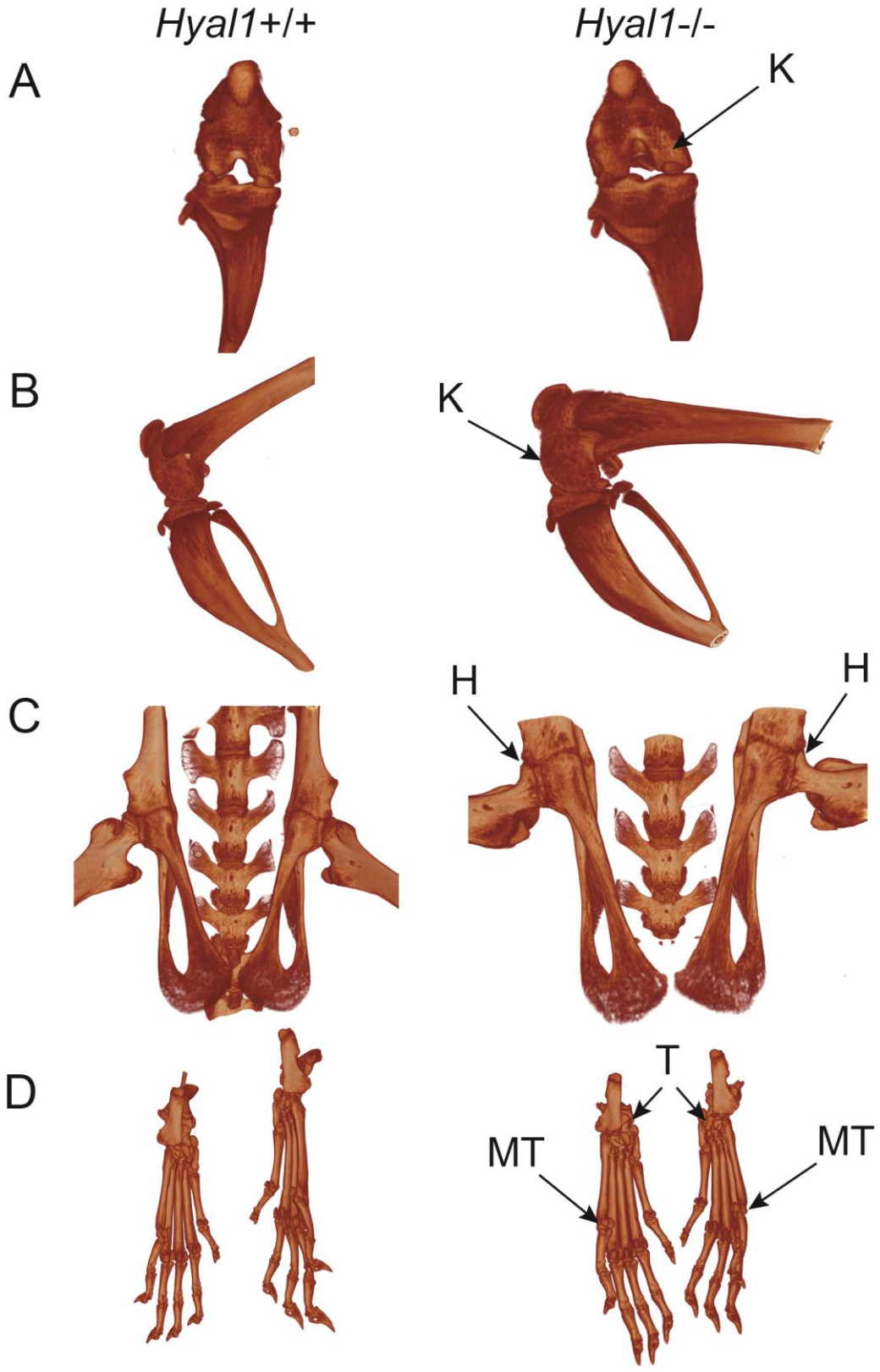
Hyal1+/+
Hyal1-/-
A
K
B
K
C
H
H
D
T
MT
MT

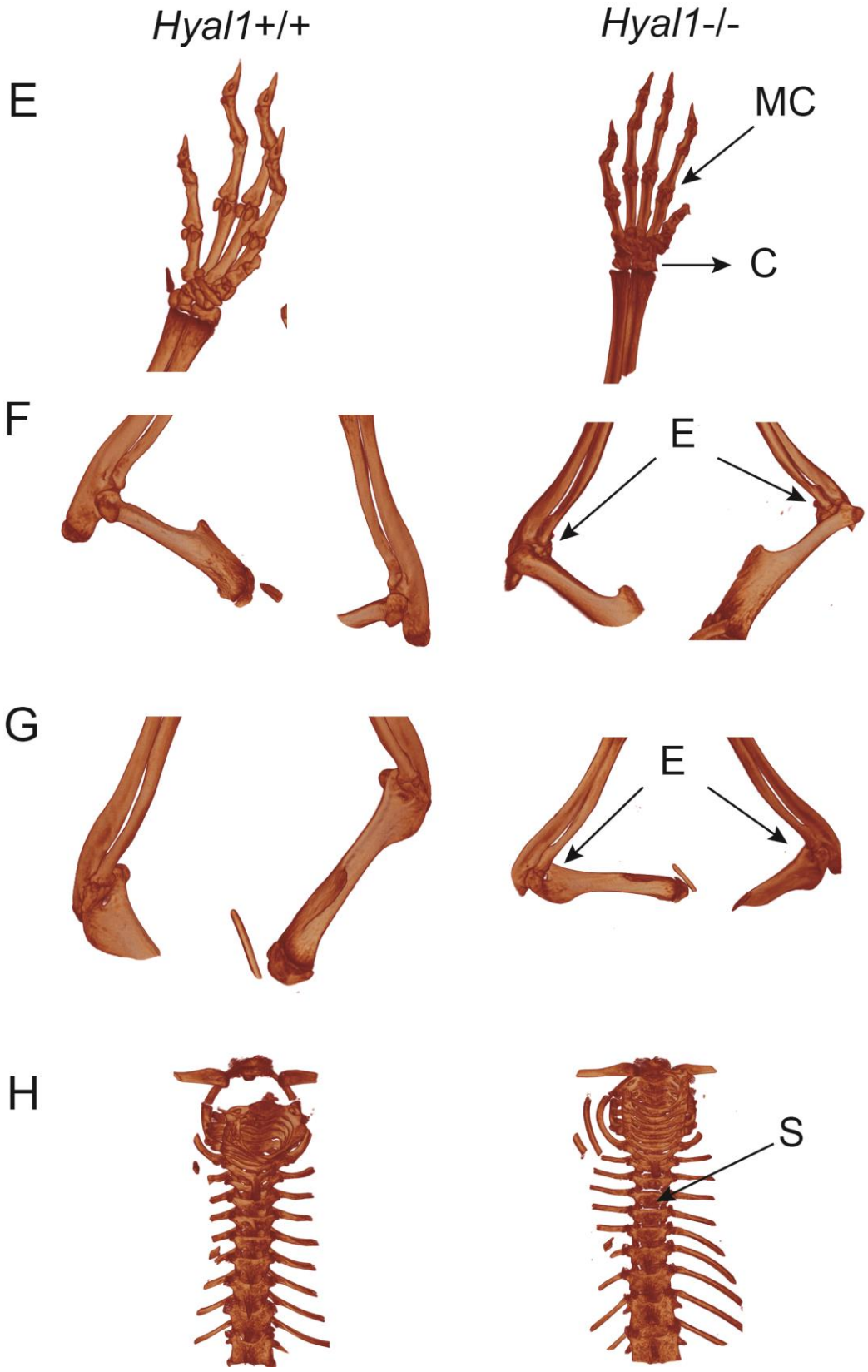
Hyal1+/+
Hyal1-/-
E
MC
C
F
E
G
E
H
S

Figure 3.7. Representative high resolution colour-coded 3-D micro-CT images of different joints of a 6 weeks old female *Hyal1*$^{-/-}$ and *Hyal1*$^{+/+}$ mouse: Images of the mouse skeleton were obtained from micro-CT scanning at 9 µm resolution and reconstructed using NRecon software, followed by manipulation using CTVox software to generate the colour-coded 3-D reconstruction. Colour-coding was chosen to provide clear view of any outgrowths, if present. Comparison between *Hyal1*$^{-/-}$ and *Hyal1*$^{+/+}$: **(**A) A ventral view of the knee joint at midway fexion. (B) A lateral view of the knee joint at midway flexion. (C) A ventral view of the pelvis including hip joint. (D) An anterior view of the hind paw showing tarsal and metatarsal joint. (E) An anterior view of the fore limb showing carpal and metacarpal joint. (F) An anterior view of elbow joint (G) A posterior view of elbow joint (H) A ventral view of spine. Arrows show features that were examined in these images. E= elbows, Ta= tarsals, MT= metatarsals, P= phalanges, MC=metacarpals, C=carpals, K=knee joint, H=Hip, S= Spine. This is a representative image from three pairs of female mice aging 6 weeks. Images are not to scale.

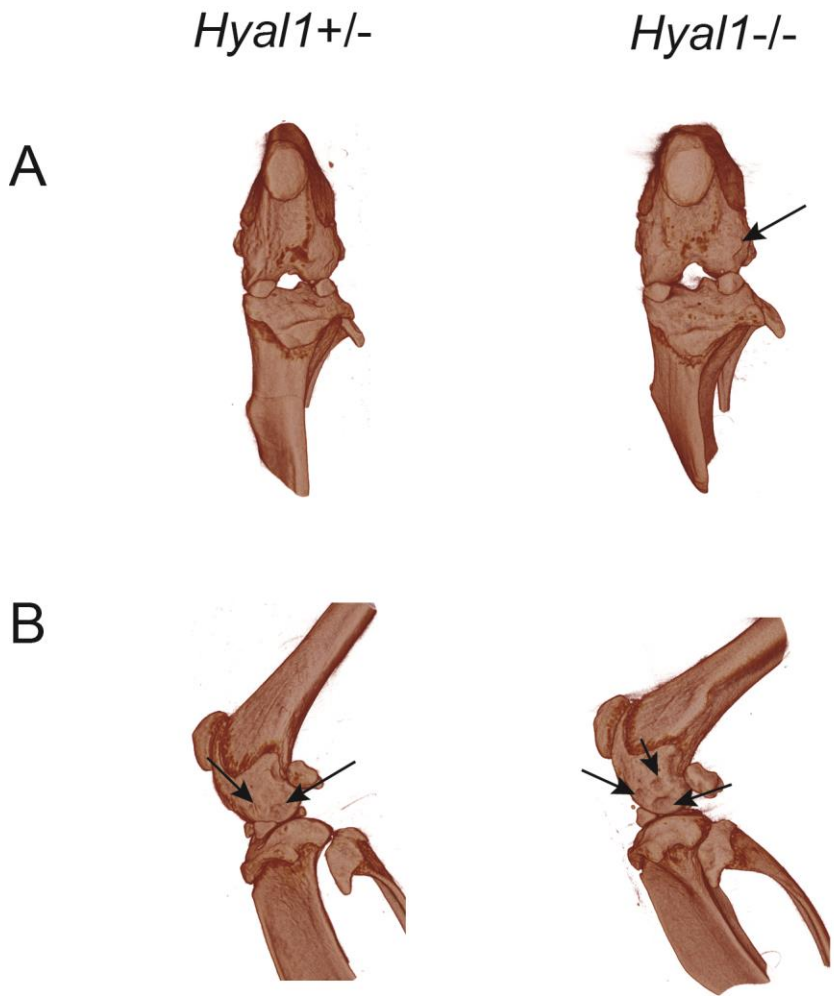

Figure 3.8. High resolution colour coded 3-D micro-CT images of knee joints of 3 months old male *Hyal1*$^{-/-}$ and *Hyal1*$^{+/-}$ mouse: Images of the mouse skeleton were obtained from micro-CT scanning at 9 µm resolution and reconstructed using NRecon software, followed by viewing in CTVox software to perform the colour coding Colour-coding was chosen appropriate to provide clear view of any outgrowths, if present. Comparison between *Hyal1*$^{-/-}$ and *Hyal1*$^{+/-}$ controls: (A) Colour-coded image of an anterior view of knee joint. (B) Colour-coded image of a lateral view of the knee joint. Arrows show a more prominent rough surface in the *Hyal1*$^{-/-}$ mouse. Images are not to scale.

3.1.5 Description of trabecular and cortical bone macroarchitecture

Macroarchitecture of trabecular and cortical bone of the femur was also analysed for differences between *Hyal1*$^{-/-}$ and control (*Hyal1*$^{+/+}$ and *Hyal1*$^{+/-}$) mice in the porosity of the trabecular bone, and the thickness of the cortical bone. For this purpose, 3-D models were generated from the volume of interest (VOIs) defined from the metaphysis for trabecular bone and from the diaphysis for cortical bone. Since trabecular bone is seen mostly at the end of long bones in the metaphysis and cortical bone in the diaphysis of the appendicular skeleton, they are commonly used to make measurements.

Trabecular and cortical bone macroarchitecture analysis was examined in both male and female mice at one year and six months of age (3 pairs per group). The observations obtained were similar for both age groups and gender and are shown in Figure 3.9 and Figure 3.10. No prominent, noticeable or consistent differences between *Hyal*1$^{-/-}$ and control mice were detected**.** In 2 pairs of male and 2 pairs of female aging 1 year, the cortical bone of the *Hyal1*$^{-/-}$ mouse was found to be slightly thicker, and trabecular bone to be denser, with reduced porosity compared to controls but this observation was inconsistent in other pairs. Overall qualitative evaluation of the micro-CT scans did not reveal noticeable differences between *Hyal1*$^{-/-}$ and control mice except severe periosteal bone formation at the lateral aspect of the distal femur.

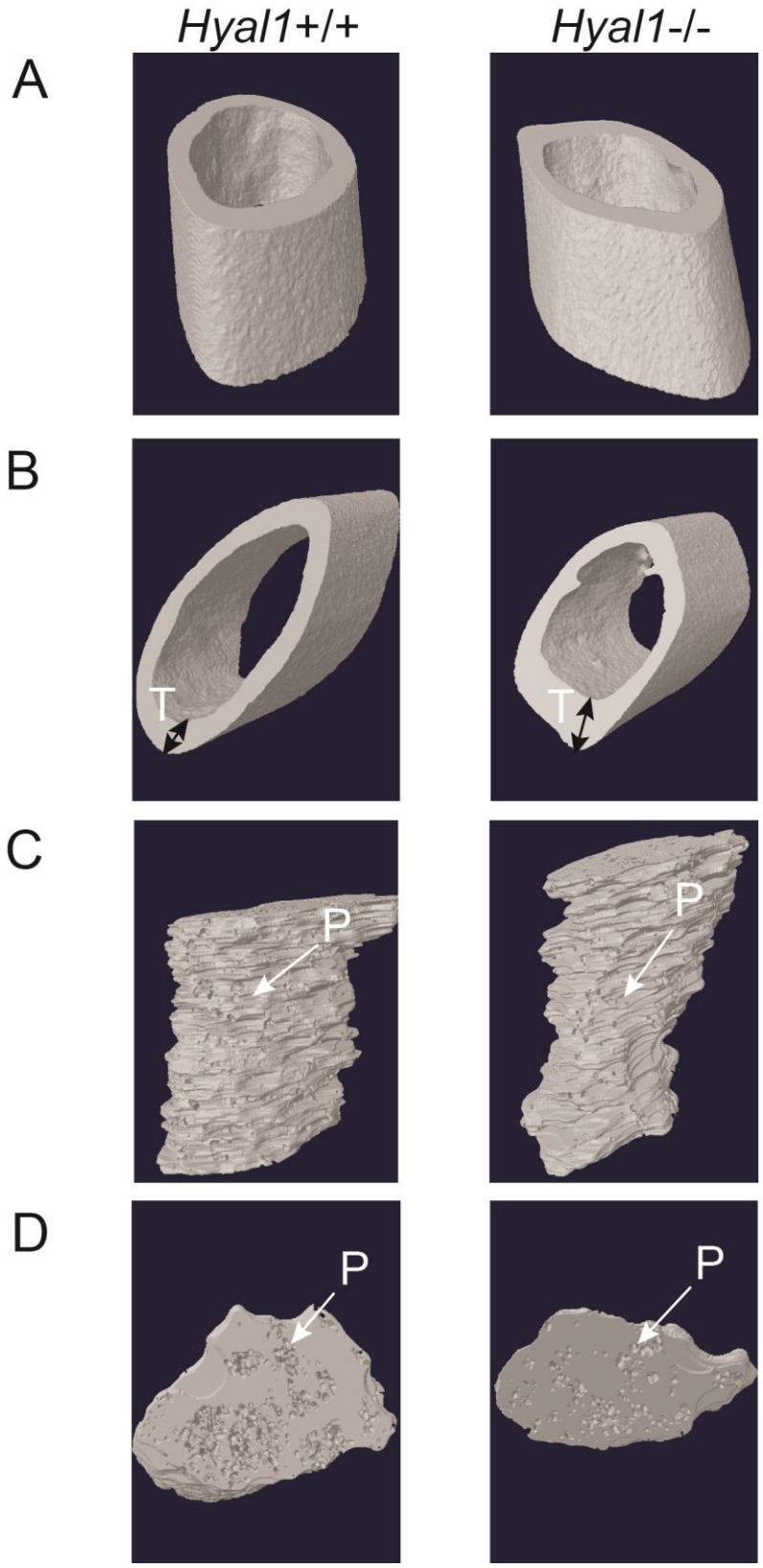
Hyal1+/+
Hyal1-/-
A
B
T
T
C
P
P
D
P
P

Figure 3.9. 3-D surface rendering of micro-CT images of cortical and trabecular bone from the femur of adult male *Hyal1*$^{-/-}$ and *Hyal1*$^{+/+}$ mice: Images were obtained by micro-CT scanning at 9 µm resolution, reconstructed using NRecon software and analyzed using CTAn software. A 3-D image file was generated by a double times cube algorithm which was finally used to visualize the volume-filled 3-D images of cortical and trabecular bone in CTVol software. Comparison between *Hyal*1$^{-/-}$ and *Hyal1*$^{+/+}$**:** (A) An anterior view of cortical bone from the diaphysis. (B) A transaxial view of cortical bone from the proximal end of the diaphysis. Black arrows in A and B highlight the thickness (T) of cortical bone which looks slightly thicker in the *Hyal1*$^{-/-}$ mouse than controls. However, this observation was not consistent in all pairs. (C) A lateral view of the trabecular bone from the metaphysis. (D) A transaxial view of trabecular bone from the proximal end of the metaphysis. Arrows highlight pores (P) in trabecular bone which appear reduced in *Hyal1*$^{-/-}$ suggesting decreased porosity, but again this observation was inconsistent appearing in only 2 of 5 pairs of male mice scanned.

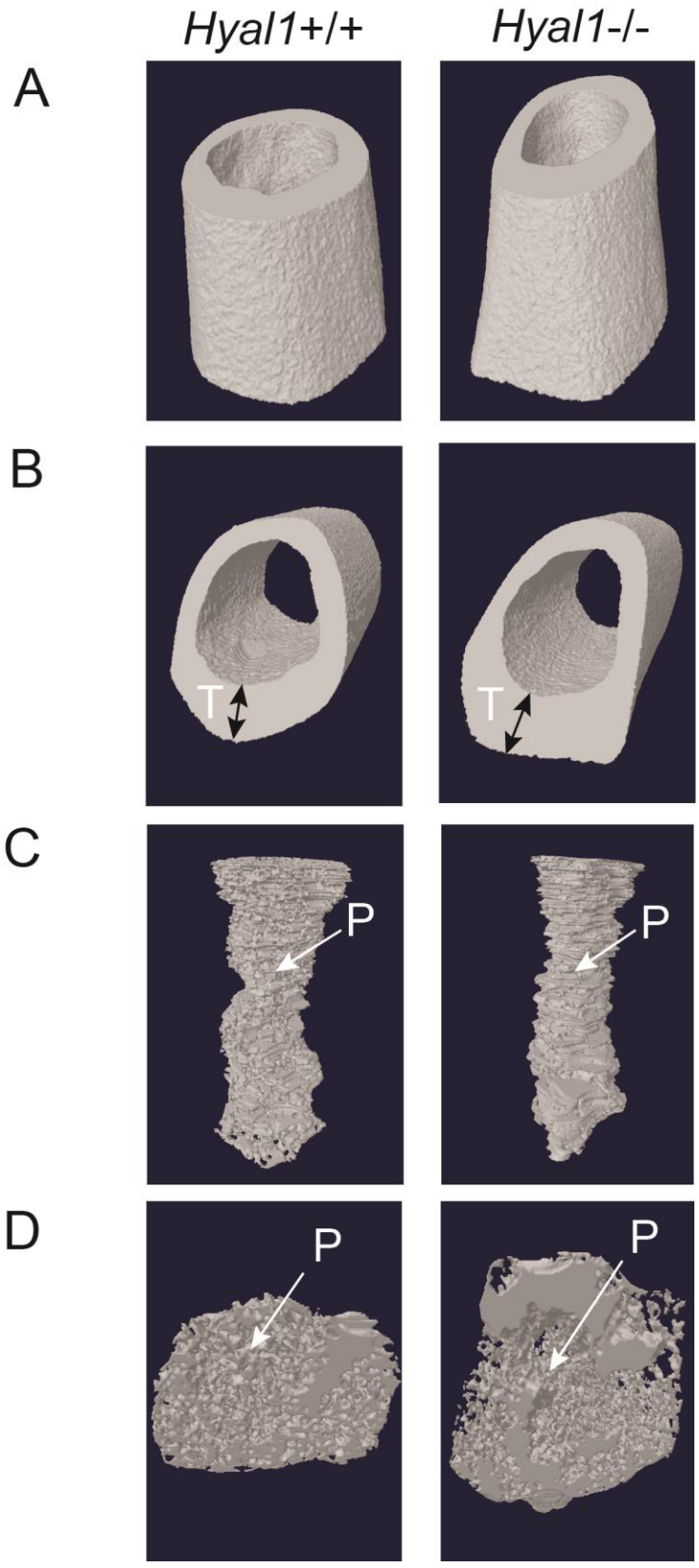
Hyal1+/+
Hyal1-/-
A
B
T
T
C
P
P
D
P
P

Figure 3.10. 3-D surface rendering of micro-CT images of cortical and trabecular bone from femur of adult female *Hyal1*$^{-/-}$ and *Hyal1*$^{+/+}$ control mouse: Images were obtained from micro-CT scanning at 9 µm resolution, reconstructed using NRecon software, and then analyzed using CTAn software. A 3-D image file was generated by the double times cube algorithm which was used to visualize the volume-filled 3-D images of cortical and trabecular bone in CTVol software. Comparison between *Hyal1*$^{-/-}$ and *Hyal1*$^{+/+}$: (A) An anterior view of cortical bone from the diaphysis. (B) A transaxial view of cortical bone from the proximal end of the diaphysis. Black arrows in A and B highlight the thickness (T) of the cortical bone which looks slightly thicker in the *Hyal*1$^{-/-}$ mouse than controls but this observation was not consistent in all pairs. (C) A lateral view of trabecular bone from the metaphysis (D) A transaxial view of trabecular bone from the proximal end of the metaphysis. Arrows highlight pores (P) in the trabecular bone which appear reduced in *Hyal1*$^{-/-}$ suggesting decreased porosity. Again this observation was inconsistent. This appeared in only 2 of 7 pairs of female mice scanned.

Chapter 4

Results Part 2: Quantitative Analysis

4.1 Determination of Bone or Tissue mineral density (BMD/TMD)

BMD is the measurement of calcium hydroxyapatite content in the whole bone, including the soft tissue within the bone. Reduced BMD helps to characterize and plays a role in the assessment of conditions like osteoporosis, osteopenia, or defects in ossification, and is an indicator for increased risk of fracture. TMD is a measurement of the calcium hydroxyapatite content in the mineralized bone, and does not include any surrounding soft tissue. To determine if HYAL1-deficiency led to changes in the mineralization of bone, micro-CT was used to quantify BMD and TMD. Determination of BMD or TMD using micro-CT allows spatial assessment of changes in bone calcification.

Trabecular bone is the soft interior part of the bone which is most abundant at the end of long bones, where it is mingled with the bone marrow in the metaphysis region. The trabecular bone is porous in nature and is often referred to as cancellous or spongy bone. Its main function is to provide structural support and organization to the bone marrow. The thin nature of the trabecular bone in mice prevents it from being easily separated from the rest of the bone using micro-CT based studies for the determination of density. As a result, trabecular bone is considered as a whole in combination with the marrow and termed BMD. Cortical bone on the other hand is the compact portion of the bone, and is denser and more calcified than the trabecular bone and thus provides mechanical strength to the skeleton. It is present outside the bone marrow space, and can

be easily separated in micro-CT-based studies to allow its mineralization to be determined as a separate tissue and termed TMD.

4.1.1 Determination of BMD and TMD using the mid-femur (standard site)

In this study, micro-CT images of the right femur of the hind limb, near to the knee joint, were used for measurements. Cortical TMD was determined from the femoral mid-diaphyseal region where cortical bone is abundant, whereas trabecular BMD was determined from the distal femoral metaphysis, which is rich in trabecular bone. The VOIs, with relation to the growth plate were selected as described in the Materials and Methods, 2.4.2. Within these VOIs, regions of interest (ROIs) representing trabecular and cortical bone were specified using both manual and automated custom processing methods (see Materials and methods, Figure 2.2). The automated method was more accurate than the manual method as it reduced variation and increased the reproducibility of the results. At both 6 months and one year of age, the mean BMD of trabecular bone did not differ significantly between the *Hyal1*$^{-/-}$ and control (*Hyal1*$^{+/+}$ or *Hyal1*$^{+/-}$) mice using either the manual or custom processing options (Tables 4.1 and 4.2 and Figures 4.1 and 4.2). Similarly, the TMD of cortical bone did not differ significantly using either custom or manual processing options (Tables 4.1 and 4.2 and Figures 4.1 and 4.2). Although custom processing had less variability in its values, the trend toward increased BMD in trabecular bone (*Hyal1*$^{+/+}$ or *Hyal1*$^{+/-}$: 0.149 ± 0.044, *Hyal*1$^{-/-}$: 0.159 ± 0.050 [p = 0.729] in animals aging 6 months and *Hyal1*$^{+/+}$ or *Hyal1*$^{+/-}$: 0.121 ± 0.010, *Hyal1*$^{-/-}$: 0.131

± 0.010 [p = 0.111] in 1 year old animals) and TMD in cortical bone (*Hyal1*$^{+/+}$ or *Hyal1*$^{+/-}$: 0.873 ± 0.104, *Hyal1*$^{-/-}$: 0.909 ± 0.056 [p = 0.479] in animals aging 6 months and *Hyal1*$^{+/+}$ or *Hyal1*$^{+/-}$: 1.010 ± 0.054, *Hyal1*$^{-/-}$: 1.038 ± 0.051 [p = 0.383]in 1 year old animals), did not reach significance.

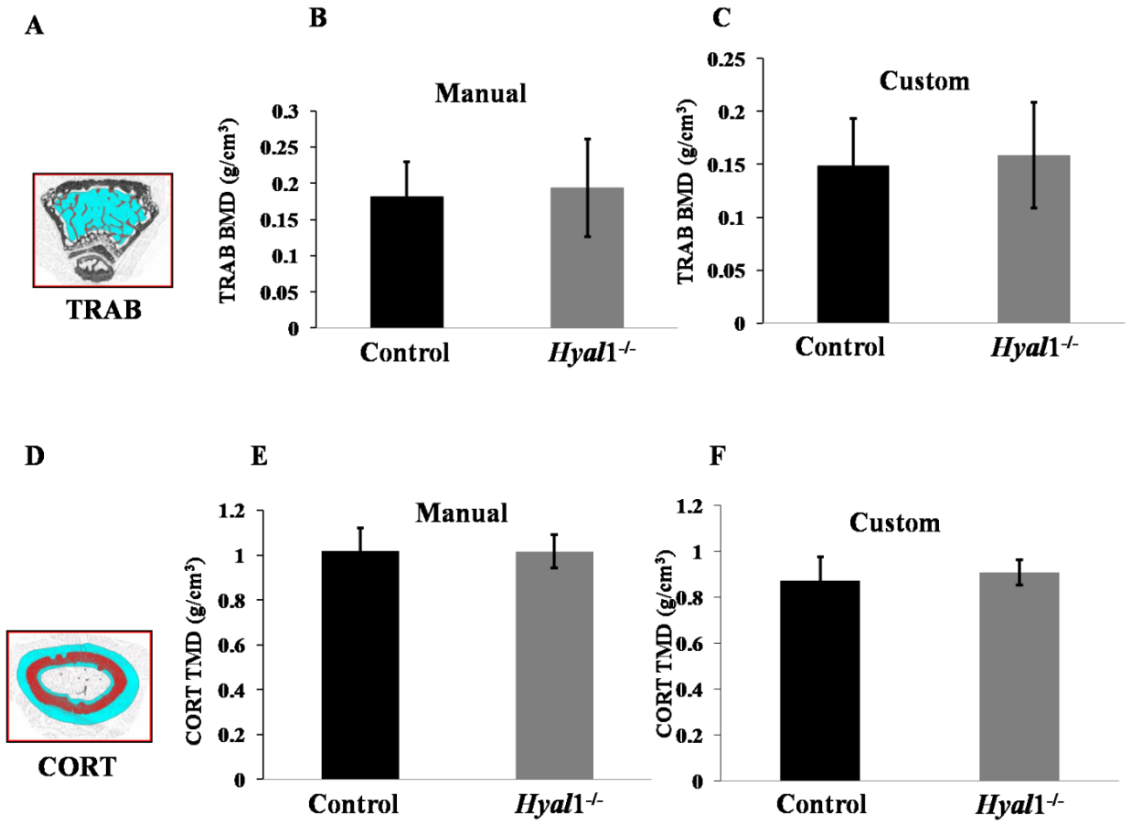

Figure 4.1. BMD of trabecular bone and TMD of cortical bone at six months of age. High resolution (9 µm) micro-CT scans were reconstructed and used to select a VOI for measurement of trabecular and cortical bone. Within these VOIs, the region of interest (ROI) was chosen by custom or manual processing. Panel A shows the ROI representing the trabecular bone (TRAB) in blue. Panel B shows the TRAB BMD for control (*Hyal1*$^{+/+}$ or *Hyal1*$^{+/-}$) and *Hyal1*$^{-/-}$ mice where the ROI for the calculation was selected manually. Panel C shows the TRAB BMD for control and *Hyal1*$^{-/-}$ mice where the ROI for the calculation was selected automatically. Panel D shows the ROI representing cortical bone (CORT) in red. Panel E shows the CORT TMD of control and *Hyal1*$^{-/-}$ mice calculated from manually selected ROIs. Panel F shows the CORT TMD of control and *Hyal1*$^{-/-}$ mice calculated from automatically selected ROIs. Bar graphs show the

mean±SD (Error bars= SD), *p < 0.05 between *Hyal1*$^{-/-}$ and control mice. (n = 6). Please note that both female and male mice were included in this calculation.

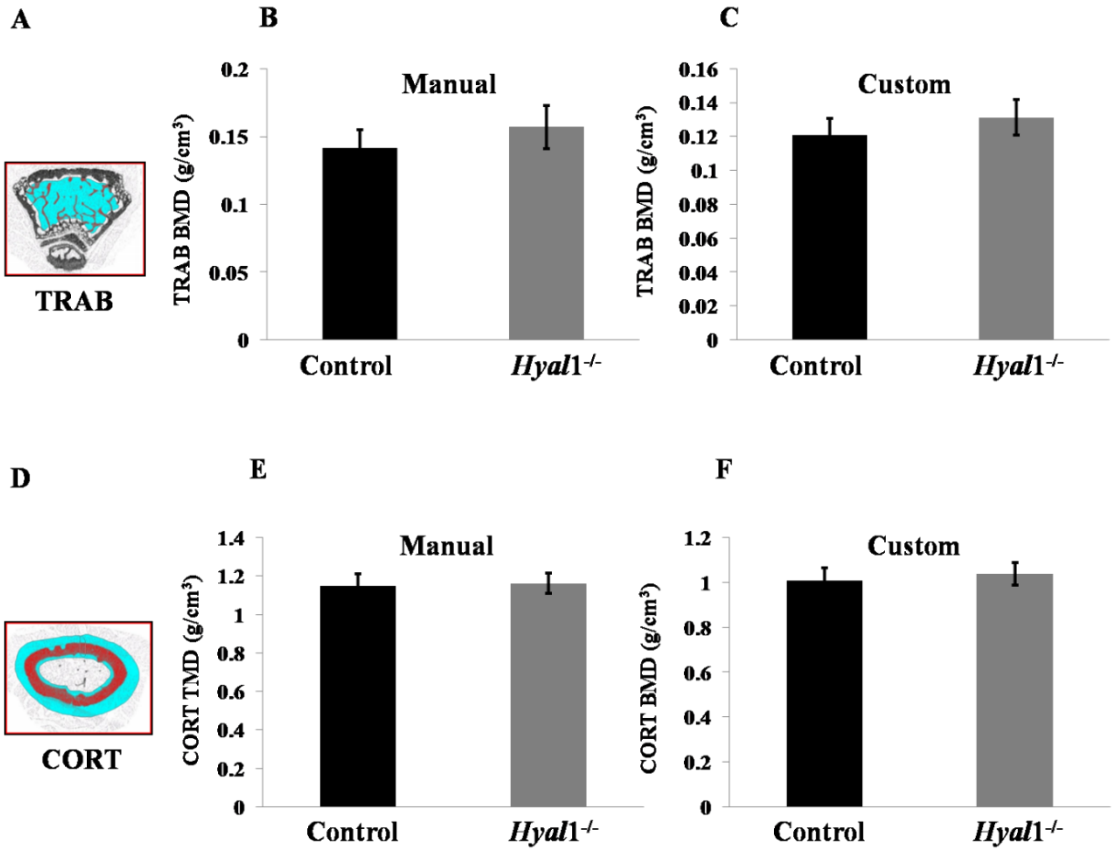

Figure 4.2. BMD of trabecular bone and TMD of cortical bone at 1 year of age. High resolution (9 µm) micro-CT scans were reconstructed and used to select a VOI for measurement of trabecular and cortical bone. Within these VOIs, the region of interest (ROI) was chosen by custom or manual processing. Panel A shows the ROI representing the trabecular bone (TRAB) in blue. Panel B shows the TRAB BMD for control (*Hyal1*$^{+/+}$ or *Hyal1*$^{+/-}$) and *Hyal1*$^{-/-}$ mice where the ROI for the calculation was selected manually. Panel C shows the TRAB BMD for control and *Hyal1*$^{-/-}$ mice where the ROI for the calculation was selected automatically. Panel D shows the ROI representing cortical bone (CORT) in red. Panel E shows the CORT TMD of control and *Hyal1*$^{-/-}$ mice calculated from manually selected ROIs. Panel F shows the CORT TMD of control and *Hyal1*$^{-/-}$ mice calculated from automatically selected ROIs. Bar graphs show the mean±SD (Error bars= SD), *$p < 0.05$ between *Hyal1*$^{-/-}$ and control mice. (n = 6). Please note that both female and male mice were included in this calculation.

4.1.2 Determination of BMD from the distal femur

Qualitative analysis of high resolution scans of hind limbs showed abnormal periosteal bone formation at the distal femurs near knee joints. To determine if periosteal bone formation brings any change in the bone mineral density, both trabecular and cortical BMD were measured from the distal femoral epiphysis using manual and automated methods. The region of interest was chosen from the edge of the articular cartilage to the growth plate. The mean BMD measurements for epiphyseal trabecular bone were as follows: by manual method, *Hyal1*$^{+/+}$ or *Hyal1*$^{+/-}$: 0.512 ± 0.037, *Hyal1*$^{-/-}$: 0.547 ± 0.052 ($p = 0.215$); by custom processing, *Hyal1*$^{+/+}$ or *Hyal1*$^{+/-}$: 0.349 ± 0.048, *Hyal1*$^{-/-}$: 0.349 ± 0.045 ($p = 0.999$). The mean TMD measurements for epiphyseal cortical bone were as follows: by manual method, *Hyal1*$^{+/+}$ or *Hyal1*$^{+/-}$: 0.883 ± 0.025, *Hyal1*$^{-/-}$: 0.879 ± 0.029 ($p = 0.782$); by custom processing, *Hyal1*$^{+/+}$ or *Hyal1*$^{+/-}$: 0.755 ± 0.019, *Hyal1*$^{-/-}$: 0.757 ± 0.043 ($p = 0.906$). Similar to standard sites, BMD and TMD measured from epiphysis also didn't show any significant difference between the groups. (Figure 4.3 and 4.4)

The summarized mean BMD measurements obtained from micro-CT analysis for *Hyal1*$^{-/-}$ and controls are also given in the Tables 4.1 and 4.2. So overall, the results of the mean BMD values from the micro-CT images resembled the qualitative radiodensity trends of the grayscale images in showing no density change. Also increased periosteal bone formation at the distal femur didn't seem to bring any significant changes in the trabecular and cortical BMD, provoking other speculations for the phenotype seen in *Hyal1*$^{-/-}$ mice.

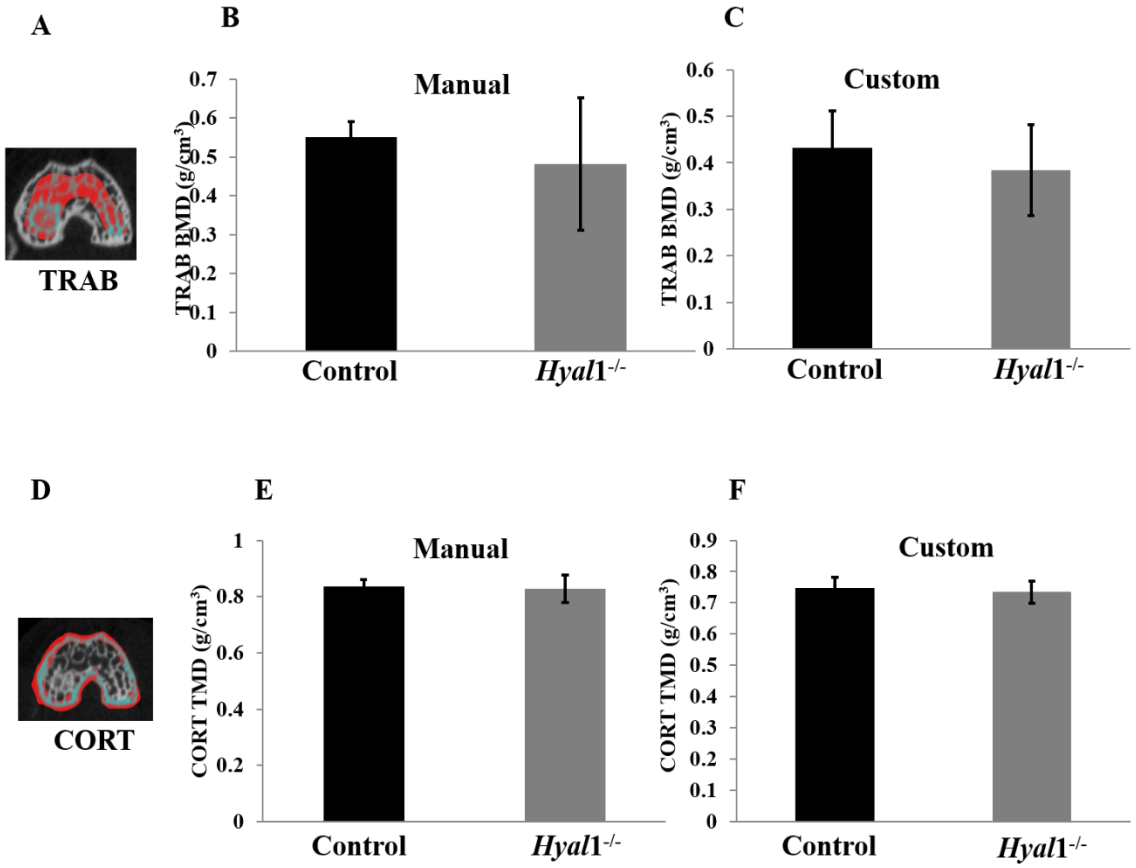

Figure 4.3. BMD of trabecular bone and TMD of cortical bone from epiphysis at 6 months of age: High resolution (9 µm) micro-CT scans were reconstructed and used to select a VOI for measurement of trabecular and cortical bone. Within these VOIs, the region of interest (ROI) was chosen by custom or manual processing. Panel A shows the ROI representing the trabecular bone (TRAB) from epiphysis in red. Panel B shows the TRAB BMD for control (*Hyal1*$^{+/+}$ or *Hyal1*$^{+/-}$) and *Hyal1*$^{-/-}$ mice where the ROI for the calculation was selected manually. Panel C shows the TRAB BMD for control and *Hyal1*$^{-/-}$ mice where the ROI for the calculation was selected automatically. Panel D shows the ROI representing cortical bone (CORT) from epiphysis in blue. Panel E shows the CORT TMD of control and *Hyal1*$^{-/-}$ mice calculated from manually selected ROIs. Panel F shows the CORT TMD of control and *Hyal1*$^{-/-}$ mice calculated from automatically selected ROIs. Bar graphs show the mean±SD (Error bars= SD), *$p < 0.05$ between *Hyal1*$^{-/-}$ and control mice. (n = 6). Please note that both female and male mice were included in this calculation.

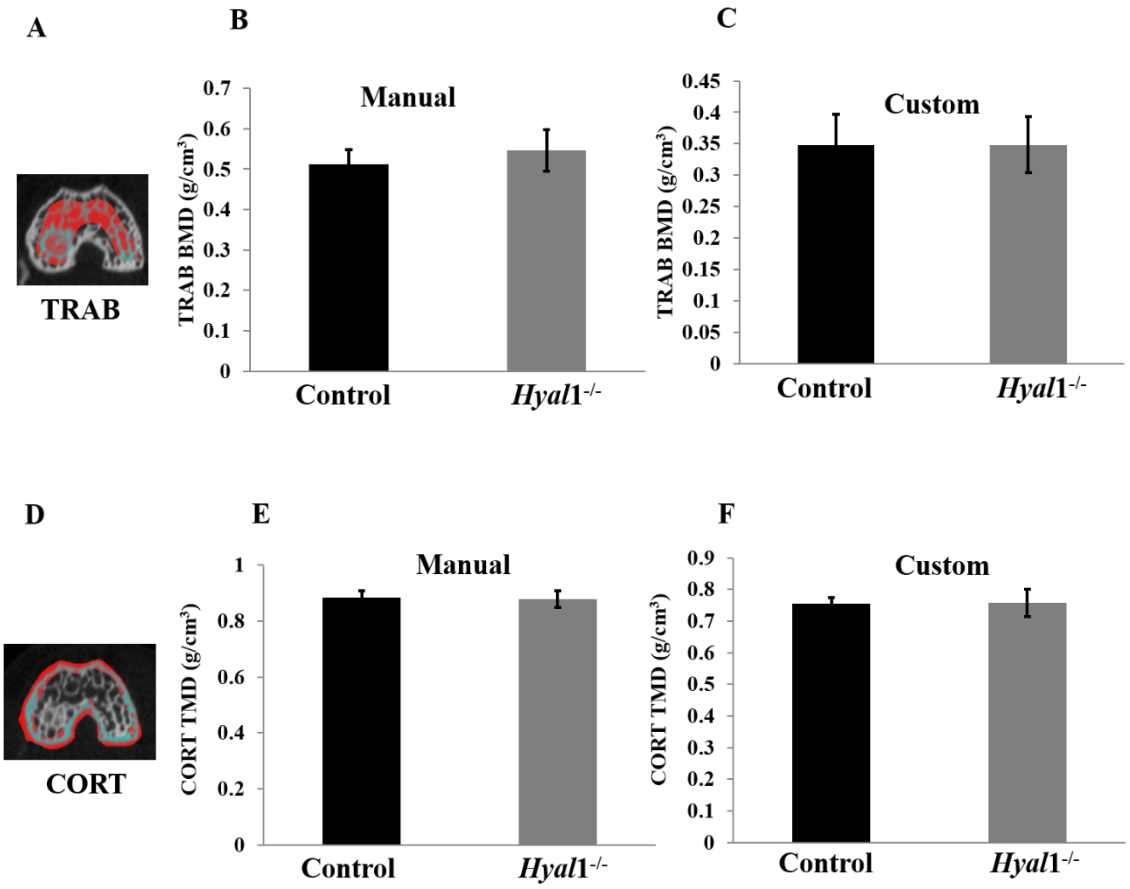

Figure 4.4. BMD of trabecular bone and TMD of cortical bone from epiphysis at 1 year of age: High resolution (9 µm) micro-CT scans were reconstructed and used to select a VOI for measurement of trabecular and cortical bone. Within these VOIs, the region of interest (ROI) was chosen by custom or manual processing. Panel A shows the ROI representing the trabecular bone (TRAB) from epiphysis in red. Panel B shows the TRAB BMD for control (*Hyal1*$^{+/+}$ or *Hyal1*$^{+/-}$) and *Hyal1*$^{-/-}$ mice where the ROI for the calculation was selected manually. Panel C shows the TRAB BMD for control and *Hyal1*$^{-/-}$ mice where the ROI for the calculation was selected automatically. Panel D shows the ROI representing cortical bone (CORT) from epiphysis in blue. Panel E shows the CORT TMD of control and *Hyal1*$^{-/-}$ mice calculated from manually selected ROIs. Panel F shows the CORT TMD of control and *Hyal1*$^{-/-}$ mice calculated from automatically selected ROIs. Bar graphs show the mean±SD (Error bars= SD), *$p < 0.05$ between *Hyal1*$^{-/-}$ and control mice. (n = 6). Please note that both female and male mice were included in this calculation.

Table 4.1. Comparison of trabecular BMD and cortical TMD of 6 month old mice (n=6).

BMD (g/cm^3)	***Hyal1*$^{+/+}$ or *Hyal1*$^{+/-}$**	***Hyal1*$^{-/-}$**	**p-value***
Metaphysis & diaphysis			
MANUAL			
TRAB BMD	0.181±0.049	0.194±0.068	0.724
CORT BMD	1.018±0.104	1.017±0.073	0.982
CUSTOM PROCESSING			
TRAB BMD	0.149±0.044	0.159±0.050	0.729
CORT BMD	0.873±0.104	0.909±0.056	0.479
Epiphysis			
MANUAL			
TRAB BMD	0.552±0.038	0.481±0.170	0.345
CORT BMD	0.837±0.022	0.828±0.049	0.672
CUSTOM PROCESSING			
TRAB BMD	0.432±0.079	0.385±0.098	0.378
CORT BMD	0.747±0.035	0.734±0.035	0.531

Table 4.2. Comparison of trabecular BMD and cortical TMD of 1 year old mice (n=6)

BMD (g/cm^3)	***Hyal1*$^{+/+}$ or *Hyal1*$^{+/-}$**	***Hyal1*$^{-/-}$**	**p-value ***
Metaphysis & diaphysis			
MANUAL			
TRAB BMD	0.141±0.014	0.157±0.016	0.101
CORT TMD	1.149±0.061	1.163±0.053	0.690
CUSTOM PROCESSING			
TRAB BMD	0.121±0.010	0.131±0.010	0.111
CORT TMD	1.010±0.054	1.038±0.051	0.383
Epiphysis			
MANUAL			
TRAB BMD	0.512±0.037	0.547±0.052	0.215
CORT TMD	0.883±0.025	0.879±0.029	0.782
CUSTOM PROCESSING			
TRAB BMD	0.349±0.048	0.349±0.045	0.999
CORT TMD	0.755±0.019	0.757±0.043	0.906

4.2 Trabecular & Cortical Bone Microarchitecture assessment

To extend our characterization of the pathophysiology of the skeletal system in HYAL1 deficiency, bone microarchitecture of *Hyal1*$^{-/-}$ and control (*Hyal1*$^{+/+}$ or *Hyal1*$^{+/-}$) mice were evaluated and compared. Using the same volume of interest defined for bone or

tissue density measurements, certain morphometric parameters of the trabecular and cortical bone were calculated. The bone microarchitecture were measured from VOIs that were defined from the standard sites, right femoral distal metaphysis for trabecular bone and right femoral diaphysis for cortical bone. Micro-CT bone morphometry is an advanced form of bone histomorphometry and has been used by others to examine changes in the bone [101].

Parameters calculated for trabecular bone were bone volume fraction (BV/TV) which indicates the amount of bone volume present in the total tissue volume, trabecular bone pattern factor (Tb.Pf) which indicates the connectivity within the trabecular bone, trabecular thickness (Tb.Th) which is the measure of average trabecular thickness, trabecular separation (Tb.Sp) which is the measure of average distance of non-bone part between the trabeculae, trabecular number (Tb.N) which is the amount of trabecular bone present per unit length and connectivity density (Conn.D) which measures the number of connections between the trabecular structures per unit volume. Similarly, the parameters calculated for cortical bone were periosteal perimeter (Pe.Pm) which is the total surface area covered by the periosteum layer surrounding the cortical bone, periosteal volume (Pe.V) which is the total volume inside the periosteum, endosteal perimeter (En.Pm) which is the total surface area covered by the endosteum inside the cortical bone, endosteal volume (En.V) which is the total volume inside the endosteum and cortical thickness (Ct.Th) which is the average thickness of cortical bone [102, 103].

Parallel to qualitative analysis, no significant differences between 6 months old male and female *Hyal1*$^{-/-}$ and control (*Hyal1*$^{+/+}$ or *Hyal1*$^{+/-}$) mice were found for all

trabecular and cortical bone parameters (Figure 4.5, 4.6). However, at one year there was a statistically significant increase in trabecular separation in *Hyal1*$^{-/-}$ mice (1.331 ± 0.045) compared to controls (1.404 ± 0.057, [p = 0.035]) and likewise a decrease in the trabecular number of *Hyal1*$^{-/-}$ mice (0.708 ± 0.099) compared to controls (0.548 ± 0.148) which was close to significance (p = 0.052). No statistically significant difference was found in other trabecular parameters like trabecular thickness, bone volume fraction, connectivity density, and trabecular pattern factor (Figure 4.7). While there do appear to be some differences in the trabecular bone structure, further micro-CT controls would need to be done to verify that the calculations of trabecular bone are accurate because trabecular bone of mice is too thin to be analysed accurately in micro-CT based studies. The values obtained are for trabecular bone combined with bone marrow. This can be overcome by using controls for example, tin foil of different widths could be scanned to determine the accuracy with which bone thickness can be measured.

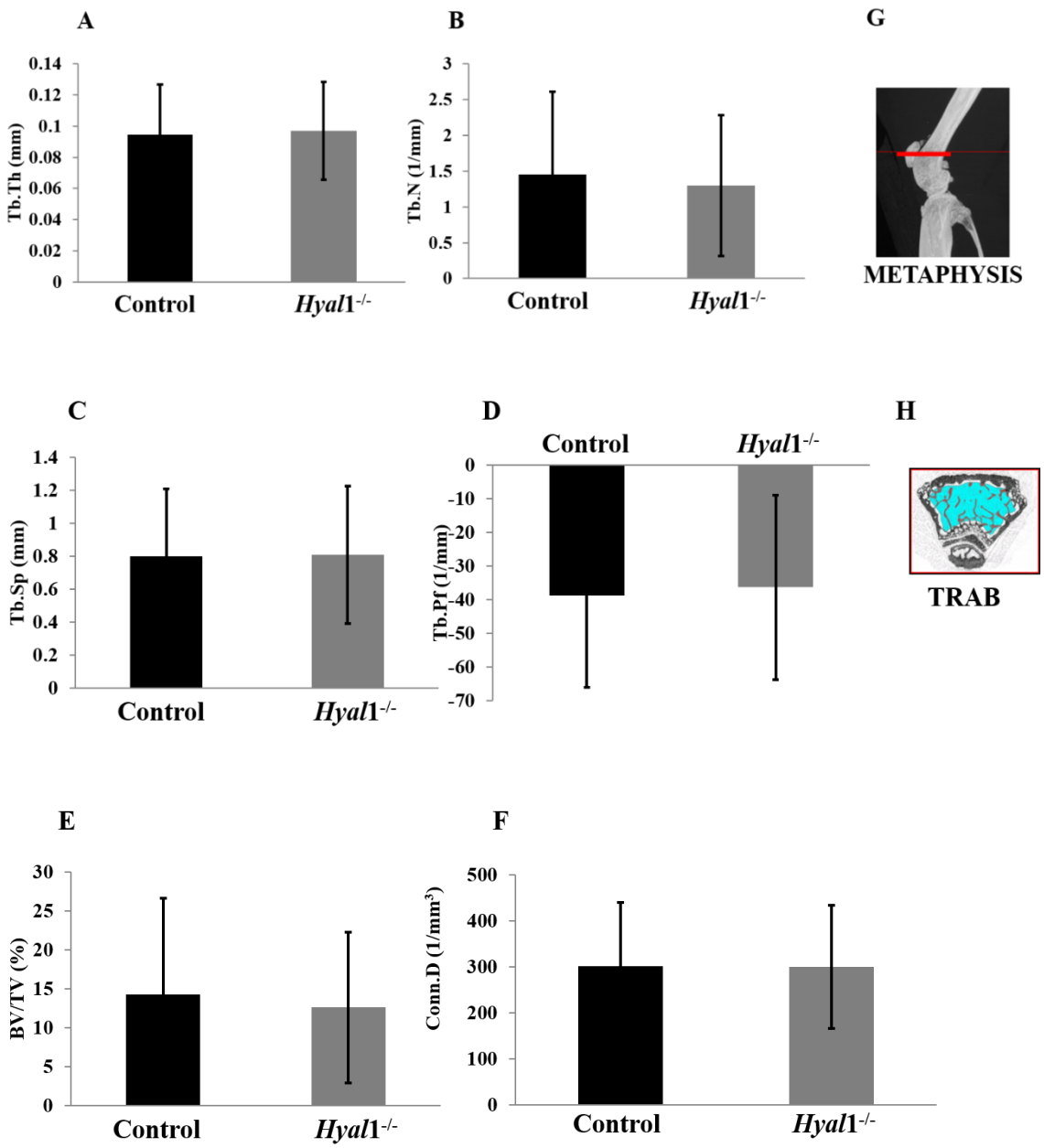

Figure 4.5. Comparison of morphometric parameters of trabecular bone in *Hyal1*$^{-/-}$ mice and controls (*Hyal1*$^{+/+}$ or *Hyal1*$^{+/-}$) at six months of age: Micro-CT images from high resolution scans were analyzed in CTAn as described in 2.4.3 from the metaphysis of femur**.** Panel A shows comparison of trabecular thickness. Panel B shows comparison of trabecular number. Panel C shows comparison of trabecular separation. Panel D shows comparison of trabecular pattern factor. Panel E shows comparison of bone volume fraction. Panel F shows comparison of connectivity density. Panel G shows the

metaphysis region of the femur indicated by red bar from where all the trabecular measurements were made. Panel H highlights the region of interest (ROI) for trabecular bone from the femoral metaphysis defined by the CTAnalyser software ROI tool. Bar graphs show mean±SD (Error bars= SD), *p < 0.05 between *Hyal1*$^{-/-}$ and control mice. Abbrevations: Tb.Th, trabecular thickness; Tb.N, Trabecular number; Tb.Sp, Trabecular separation; Tb.Pf, Trabecular pattern factor, BV/TV, bone volume/tissue volume; Conn.D, Connectivity density. Please note that both female and male mice were included in this calculation.

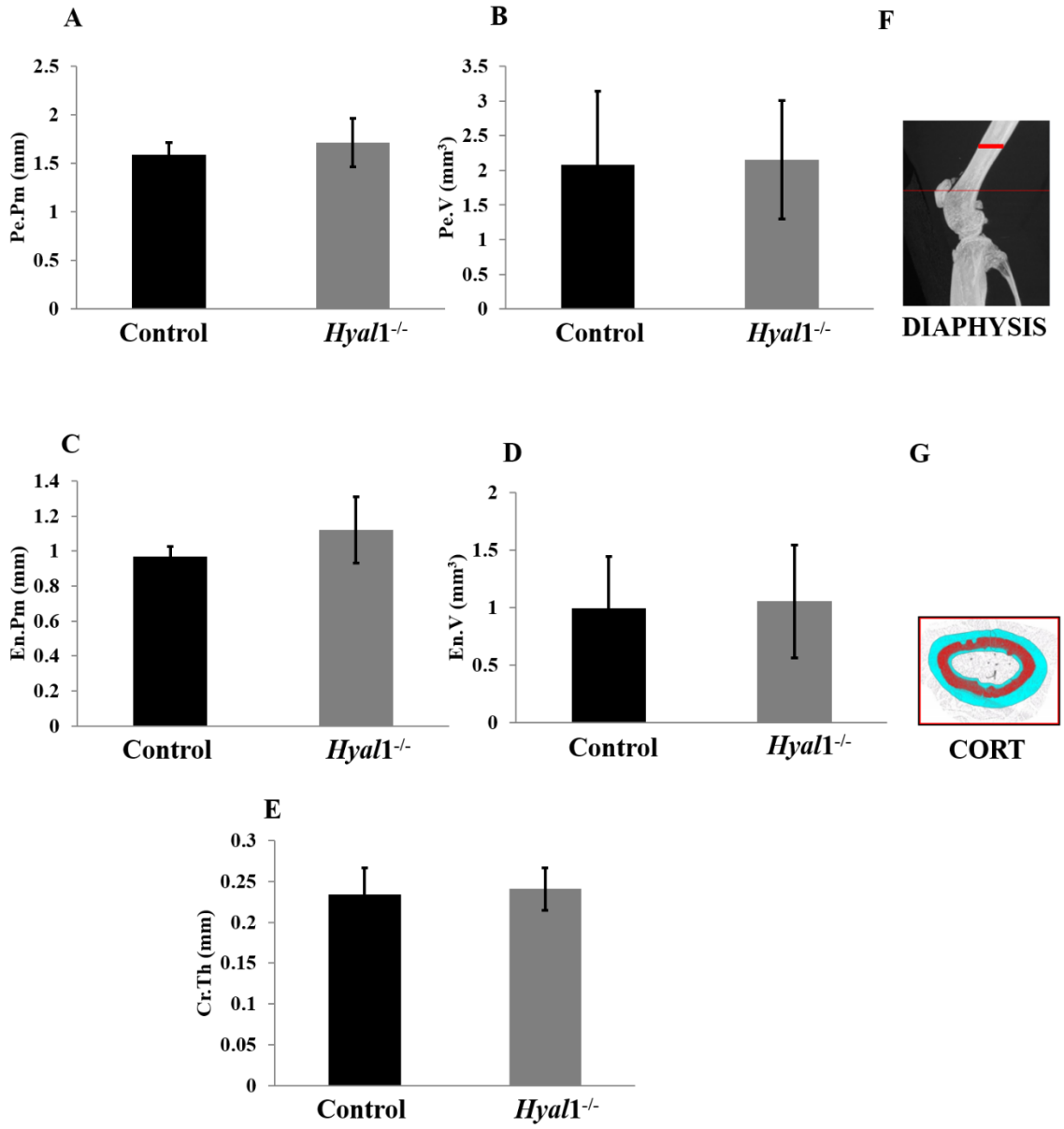

Figure 4.6. Comparison of morphometric parameters of cortical bone in *Hyal1*$^{-/-}$ mice and controls (*Hyal1*$^{+/-}$ or *Hyal*$^{+/-}$) at six months of age: Micro-CT images from high resolution scans were analyzed in CTAn as described in 2.4.3 from the diaphysis of femur**.** Panel A shows comparison of periosteal perimeter in *Hyal1*$^{-/-}$ than controls. Panel B shows a comparison of periosteal volume in *Hyal1*$^{-/-}$ and controls. Panel C shows a comparison in the endosteal perimeter between *Hyal1*$^{-/-}$ and controls. Panel D shows comparison in the endosteal volume of *Hyal1*$^{-/-}$ compared to controls. Panel E shows a comparison in the cortical thickness of *Hyal1*$^{-/-}$ and controls. Panel F shows a red bar in the diaphysis region of the knee joint indicates the region from which measurements were made. Panel G highlights the region of interest (ROI) for cortical bone from the femoral diaphysis defined by the CTAnalyser software ROI tool. A set of ROIs from several consecutive cross sections were used to make a volume of interest (VOI) for cortical bones from which morphometric parameters were measured. Bar graphs show mean±SD (Error bars= SD), *p < 0.05 between *Hyal1*$^{-/-}$ and control mice. (n = 6). Abbrevations: Pe.Pm, Periosteal perimeter; Pe.V, Periosteal volume; En.Pm, Endosteal perimeter; En.V, Endosteal volume; Cr.Th, Cortical thickness. Please note that both female and male mice were included in this calculation.

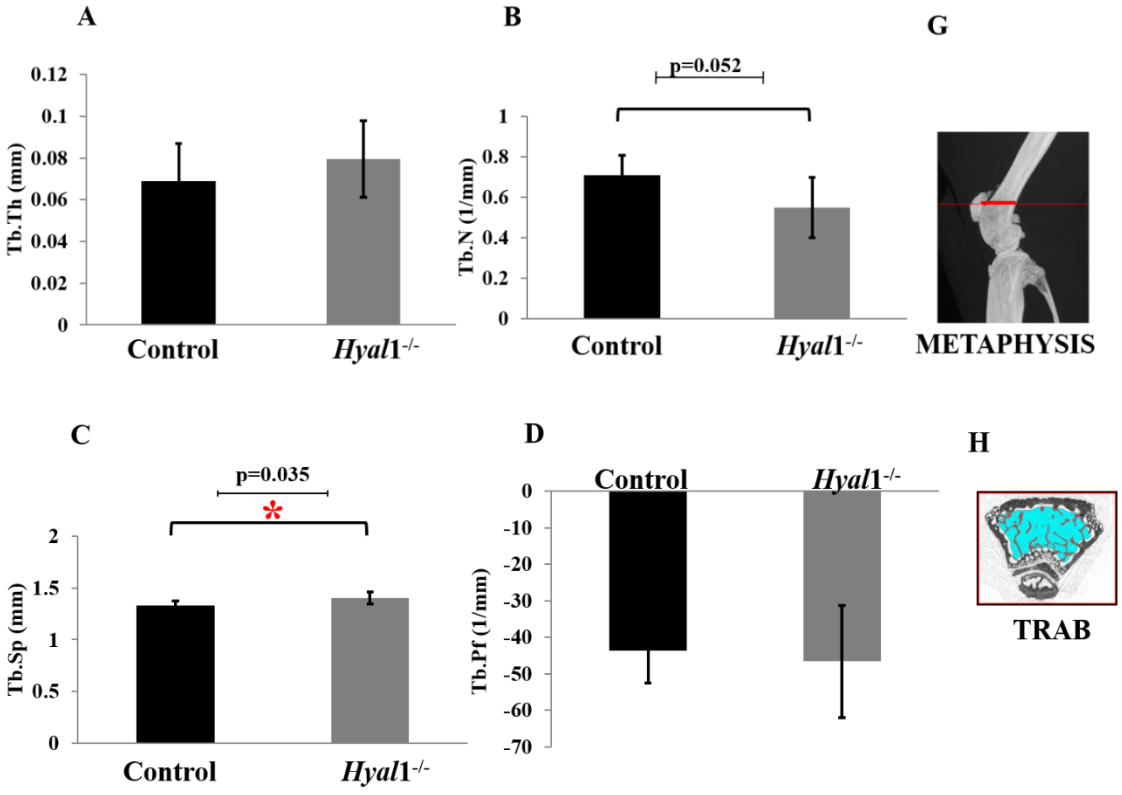

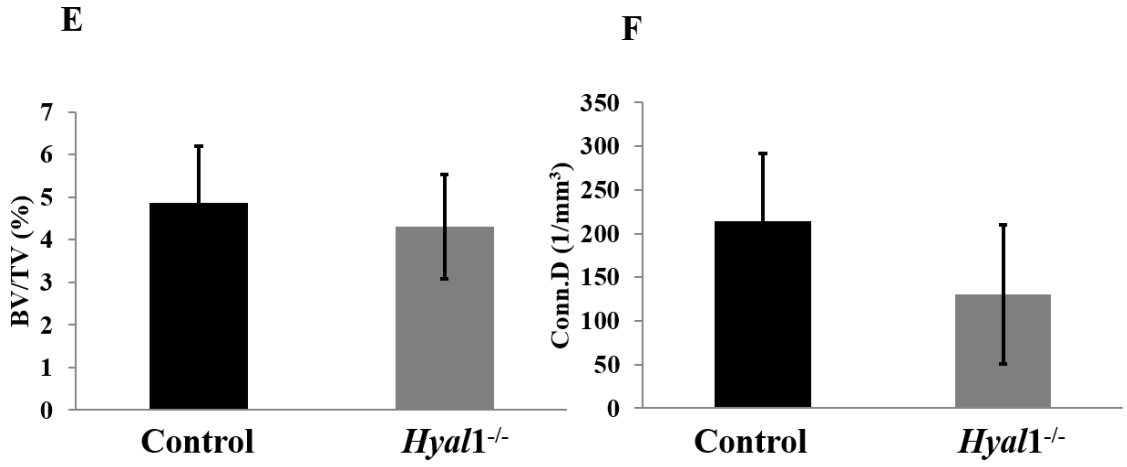

Figure 4.7. Comparison of morphometric parameters of trabecular bone in Hyal1$^{-/-}$ mice and controls (*Hyal1*$^{+/-}$ or *Hyal1*$^{+/-}$) at one year of age: Micro-CT images from high resolution scans were analyzed in CTAn as described in 2.4.3 from the metaphysis of femur**.** Panel A shows a comparison of trabecular thickness. Panel B shows a comparison of trabecular number. Panel C shows a comparison of trabecular separation. Panel D shows comparison of trabecular pattern factor. Panel E shows a comparison of bone volume fraction. Panel F shows a comparison of connectivity density. Panel G shows a red bar in the metaphysis region of the femur indicating the area from where all the trabecular measurements were made. Panel H highlights the region of interest (ROI) for trabecular bone from the femoral metaphysis defined by the CTAnalyser software ROI tool. Bar graphs show mean±SD (Error bars= SD), *p < 0.05 between *Hyal1*$^{-/-}$ and control mice. Abbrevations: Tb.Th, trabecular thickness; Tb.N, Trabecular number; Tb.Sp, Trabecular separation; Tb.Pf, Trabecular pattern factor, BV/TV, bone volume/tissue volume; Conn.D, Connectivity density. Please note that both female and male mice were included in this calculation.

The primary differences in the cortical bone parameters at one year of age were in the average periosteal perimeter which was 2.165 ± 0.183 in *Hyal1*$^{-/-}$ mice, significantly greater than that in the controls, 1.890 ± 0.128 ($p = 0.013$). Periosteal volume was also significantly increased in *Hyal1*$^{-/-}$ mice (3.190 ± 0.533) compared to controls (2.452 ± 0.317, $p < 0.016$). Differences in other cortical bone parameters including the endosteal perimeter, endosteal volume and cortical thickness did not significantly differ (Figure 4.8). Tables 4.3 & 4.4 show the summarized data and comparison of trabecular and

cortical morphometric parameters of *Hyal1*$^{-/-}$ and control mice at 1 year and 6 months of age.

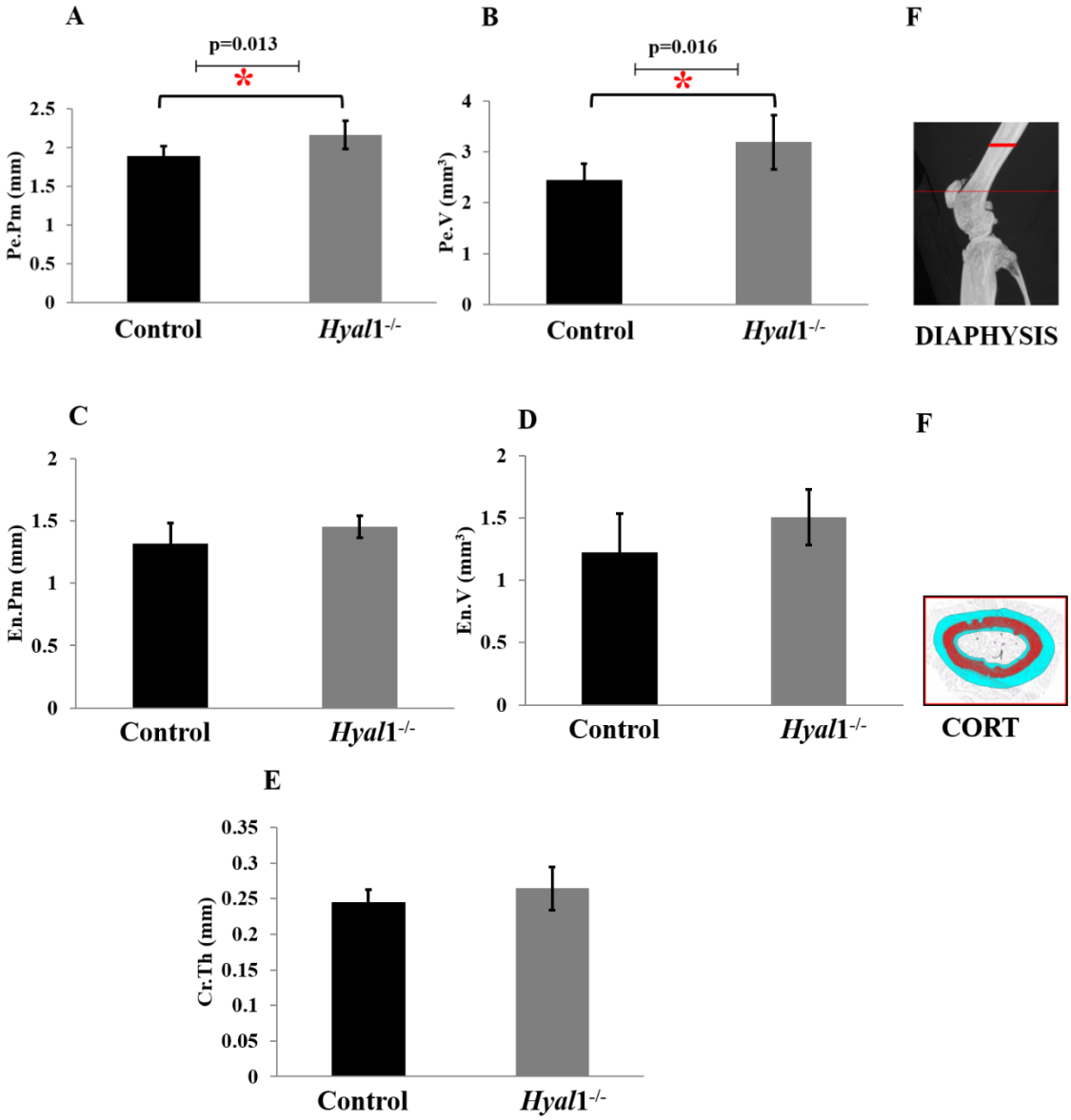

Figure 4.8. Comparison of morphometric parameters of cortical bone in *Hyal1*$^{-/-}$ mice and controls (*Hyal1*$^{+/+}$ or *Hyal1*$^{+/-}$) at one year of age: Micro-CT images from high resolution scans were analyzed in CTAn as described in 2.4.3.4 from the diaphysis of femur. Panel A shows a comparison of periosteal perimeter in *Hyal1*$^{-/-}$ and controls. Panel B shows a comparison of periosteal volume in *Hyal1*$^{-/-}$ than controls. Panel C shows a comparison in the endosteal perimeter between in *Hyal1*$^{-/-}$ and controls. Panel D

shows a comparison in the endosteal volume of *Hyal1*$^{-/-}$ compared to controls. Panel E shows a comparison in the cortical thickness of *Hyal1*$^{-/-}$ and controls. Panel F A red bar in the diaphysis region of the knee joint indicates the region from which measurement were made. Panel G highlights the region of interest (ROI) for cortical bone from the femoral diaphysis defined by the CTAnalyser software ROI tool. A set of ROIs from several consecutive cross sections were used to make a volume of interest (VOI) for cortical bones from which morphometric parameters were measured. Bar graphs show mean±SD (Error bars= SD), *$p < 0.05$ between *Hyal1*$^{-/-}$ and control mice. ($n = 6$). Abbrevations: Pe.Pm, Periosteal perimeter; Pe.V, Periosteal volume; En.Pm, Endosteal perimeter; En.V, Endosteal volume; Cr.Th, Cortical thickness. Please note that both female and male mice were included in this calculation.

Table 4.3. Morphometric parameters of the femur metaphysis in *Hyal1*$^{-/-}$ and their controls

6 months old (n=6)			
Trabecular morphometric parameters	***Hyal1*$^{+/+}$ or *Hyal1*$^{+/-}$ (mean ± SD)**	***Hyal1*$^{-/-}$ (mean ± SD)**	**p-value ***
Bone Volume fraction (BV/TV)	14.300±12.357	12.596±9.739	0.796
Trabecular bone pattern factor (Tb. Pf)	-38.734±27.390	-36.324±27.333	0.882
Trabecular thickness (Tb. Th)	0.094±0.032	0.097±0.031	0.895
Trabecular separation (Tb. Sp)	0.800±0.408	0.809±0.418	0.972
Trabecular number (Tb. N)	1.457±1.155	1.298±0.982	0.803
Connectivity Density (Conn. Den)	302.155±138.549	300.452±134.454	0.983
Cortical Parameters			
Periosteal Perimeter	1.591±0.123	1.715±0.252	0.305
Periosteal Volume	2.085±1.058	2.154±0.855	0.904
Endosteal Perimeter	0.968±0.056	1.122±0.188	0.085
Endosteal Volume	0.992±0.455	1.055±0.491	0.822
Cortical thickness	0.234±0.032	0.241±0.026	0.711

Table 4.4. Morphometric parameters of femur in *Hyal1*$^{-/-}$ and their controls

1 year old (n=6)			
Trabecular morphometric parameters	***Hyal1*$^{+/+}$ or *Hyal1*$^{+/-}$ (mean ± SD)**	***Hyal1*$^{-/-}$ (mean ± SD)**	**p-value ***
Bone Volume fraction (BV/TV)	4.877±1.316	4.312±1.230	0.460
Trabecular bone pattern factor (Tb. Pf)	-43.612±8.889	-46.617±15.426	0.688
Trabecular thickness (Tb. Th)	0.069±0.0178	0.080±0.0184	0.333
Trabecular separation (Tb. Sp)	1.331±0.045	1.404±0.057	0.035*
Trabecular number (Tb. N)	0.708±0.099	0.548±0.148	0.052
Connectivity Density (Conn. Den)	214.774±77.191	130.701±79.781	0.093
Cortical Parameters			
Periosteal Perimeter	1.890±0.128	2.165±0.183	0.013*
Periosteal Volume	2.452±0.317	3.190±0.533	0.016*
Endosteal Perimeter	1.318±0.164	1.454±0.087	0.102
Endosteal Volume	1.223±0.312	1.508±0.223	0.099
Cortical thickness	0.245±0.019	0.265±0.030	0.203

In conclusion, morphometric analysis of cortical bone revealed a significant increase in periosteal perimeter and periosteal volume of the cortical bone in one year old *Hyal1*$^{-/-}$ mice compared to controls. In the cortical bones of 6 months old mice there is a trend towards an increase in the periosteal perimeter and volume but the difference is not significant. Similarly the morphometric analysis of trabecular bone shows a significant

increase in trabecular separation and a close to significant decrease in trabecular number of *Hyal1*$^{-/-}$ than controls in one year old mice but no significant change was observed in 6 months old mice suggesting that changes taking place in cortical and trabecular bone are progressive. One limitation of this study was that the morphometric analysis was measured from the traditional sites and not from the distal epiphysis around which the outgrowth was observed because of the technical difficulty of running the program in the epiphysis region which contained outgrowths which are not connected with each other.

4.3 Determination of tibia and femur length

Shortened extremities are a common feature of MPS patients as well as animal models of MPSs. The first patient with MPS IX was also found to have short stature. Therefore micro-CT images were used to measure the length of the right femur and tibia to determine if HYAL1-deficiency had any impact on growth. The mean femur and tibia length in males and female mice at one year and six months of age are summarized in Table 4.5 and 4.6. Consistent with qualitative observations, no difference in the length of the femur or tibia was found when *Hyal1*$^{-/-}$ and controls (*Hyal1*$^{+/+}$ or *Hyal1*$^{+/-}$) at one year [male, femur: p=0.406, tibia: p=0.320 (n=3); female, femur: p= 0.320, tibia: p= 0.925 (n=3)] and 6 months [male, femur: p=0.098, tibia: p= 0.782 (n=2); female, femur: p=0.679, tibia: p= 0.992 (n=3)] of age were compared. Neither males nor females display evidence of short stature at either 6 or 12 months of age, indicating that HYAL1-deficiency does not impact growth in the mouse model. Given the variability in this

phenotypic feature in human patients, it is possible that the genetic background may impact growth and obscure any effect of HYAL1-deficiency.

Table 4.5. Comparison of right femur length in male *Hyal1*$^{-/-}$ and age matched control mice

	***Hyal1*$^{+/+}$ or *Hyal1*$^{+/-}$ Mean ± SD (mm)**	***Hyal1*$^{-/-}$ Mean ± SD (mm)**	**p-value ***
6 months (n = 2)			
Femur	15.714 ±0.108	15. 273 ± 0.182	0.098
Tibia	17.651 ± 0.073	17.634 ± 0.011	0.782
1 year (n =3)			
Femur	15.745 ± 0.067	15.925± 0.330	0.406
Tibia	17.583 ± 0.417	17.708 ± 0.051	0.320

Table 4.6. Comparison of right femur length in female *Hyal1*$^{-/-}$ mouse and age matched control mice

	***Hyal1*$^{+/+}$ or *Hyal1*$^{+/-}$ Mean ± SD (mm)**	***Hyal1*$^{-/-}$ Mean ± SD (mm)**	**p-value ***
6 months (n = 3)			
Femur	15.410 ± 0.681	15.637 ± 0.560	0.679
Tibia	17.573 ± 0.298	17.571 ± 0.209	0.992
1 year (n = 3)			
Femur	15.797 ± 0.323	15.45 ± 0.320	0.320
Tibia	17.728 ± 0.304	17.701 ± 0.353	0.925

4.4 Determination of body weights

After micro-CT scanning and before dissection on the same day, each mouse was weighed to compare the size of *Hyal1*$^{-/-}$ with controls and analyze for evidence of short

stature. This weight included the whole body mass including that of muscles and skeleton. **Table 4.7** reveals the body weights of male and female mice respectively with HYAL1 deficiency compared with age matched controls. Male and female mice were analysed separately due to the difference in the sex-specific development of the body weight and mass in some strains. No statistical difference was found when data was compared at 1 year [male p=0.875 (n=3); female p=0.725 (n=3)] and 6 months (male p=0.393 (n=2); female p=0.627 (n=4)] of age. However, there was a difference of approximately 15 g between 1 year and 6 months old males in both controls and *Hyal1*$^{-/-}$ mice. Similarly 1 year and 6 months old females showed a difference of between 8-10 g. There were also differences between the weights of male and female mice; at 1 year of age males weighed 10-15 g more than females and 8-9 g more at 6 months of age. These differences could be due to the absence of extra bony outgrowths in males at 6 months and females at 1 year of age.

Table 4.7. Comparison of body weights in *Hyal1* $^{-/-}$ mice with age matched controls

	***Hyal1*$^{+/+}$ or *Hyal1*$^{+/-}$ Mean ± SD (g)**	***Hyal1*$^{-/-}$ Mean ± SD (g)**	**p-value ***
Male			
1 year (n = 3)	49.967 ± 7.247	48.65 ± 11.345	0.874
6 months (n = 2)	34.225 ± 1.520	33.025 ± 0.389	0.393
Female			
1 year (n =3)	32.733 ± 5.611	34.5 ± 5.851	0.725
6 months (n = 4)	25.5 ± 1.435	24.938 ± 1.662	0.627

Chapter 5

Discussion, Conclusions & Future Directions

5.1 Discussion

This study is a follow up to a previous study in our laboratory in which a general characterization of HYAL1-deficient (*Hyal1*$^{-/-}$) mice was performed. In these studies, histological investigations showed a premature loss of proteoglycans from the articular cartilage of knee joints that progressed with age, as well as the presence of an osteophyte in one joint at an older age [97]. This study was however limited in that no gross morphological or 3-D analysis was performed to detect bone structure, density and microarchitecture. Therefore to better characterize the skeletal phenotype we used low and high resolution micro-CT to evaluate *Hyal1*$^{-/-}$ mice. Micro-CT imaging demonstrated consistent changes in the joints of *Hyal1*$^{-/-}$ mice, providing further evidence of significant joint involvement in HYAL1-deficiency. This new symptomatic evidence of skeletal involvement leads to further speculation regarding the mechanism underlying this pathology.

5.1.1 Periosteal bone formation in knee

In this study, we have demonstrated that there are no obvious abnormalities in the shape and structure of the skeleton in *Hyal1*$^{-/-}$ mice. However, 1 year old male mice showed multiple osteophytes which appears to be abnormal periosteal bone formation at the distal femur near knee joints. In one year old female mice, the distal femur of one of the three pairs, was rough but did not show the dramatic periosteal growth seen in the male mice.

Periosteum is a thin layer of membrane that covers the outer surface of all bones, except at joints, which are covered by articular cartilage. It is innervated, vascularised, and consists of osteogenic and fibroblastic cells. The periosteal region is often defined as a bone formation area [92]. This anatomical abnormality in *Hyal1*$^{-/-}$ adult male mice was accompanied by a significant increase in the cortical bone parameters periosteal perimeter (Pe.Pm) and volume (Pe.V), indicating extra periosteal growth. Interestingly, though we didn't find any abnormality in two 6 month old *Hyal1*$^{-/-}$ male mice, the knee joint of one *Hyal1*$^{-/-}$ male mouse showed a rough surface at the distal femur compared to the control at only 3 months. However, since the total number of male animals scanned at 3 months and 6 months are 1 and 2 respectively, we cannot confidently say that symptomatic evidence of periosteal bone formation begins at a young age.

Previous literature has shown that during bone modeling, bone is deposited on the quiescent periosteal surface without any prior resorption on the endosteal surface resulting in changes in bone size and shape. This is unlike bone remodeling where periosteal apposition occurs in response to endosteal bone erosion [109]. In this study a significant increase in periosteal parameters without any significant difference in endosteal parameters leads us to speculate that HA accumulation leads to bone modeling which might be responsible for periosteal bone formation.

The finding of periosteal bone formation from the high resolution scans of knee joints, encouraged us to examine the high resolution scans of other joints including the hip, elbow, tibiotarsal, metacarpal and cervical spine. Unfortunately, because of the timing of the periosteal findings, additional scans were only possible on one year old

female mice, which were not as severely affected as male mice. Abnormalities were not detected in these joints, suggesting that the knee joint is the most severely affected area in mice. Although it is possible that other joints might have been affected in male mice, the costs and time required to age an additional set of *Hyal1*$^{-/-}$ and control mice was prohibitive. Knee joints may be the most severely affected because they are the most stressed weight bearing joint of the body unlike other weight bearing joints like hip and ankle. Hip joint is a ball and socket joint which has the tendency to move in all directions thus making it a much stronger and stable joint. Ankles are gliding joint where the articular cartilage is flat or slightly curved allowing limited motion mostly gliding movements between the two bones. Knee are modified hinge joints that can bend, extend and slightly rotate. Because of its structure they usually bear more pressure with weight and other loads while movement (Fig. 1.3) [123]. In quadruped animals like mice, the knee joint is referred to as a stifle joint, which is the most complex synovial joint of the animal's body and is equivalent to the human knee joint[124]. Also, the fact that periosteum is thickest in the long bone diaphysis (2-3 mm) and very thin in metaphysis and epiphysis [110], may explain the propensity for periosteal bone formation in long bones due to changes in bone matrix. One might expect elbows which are similar to knee joints to be affected as well. However, though the elbow and knee are hinge joints, the elbow has only one plane of motion (flexion & extension) whereas the knee has flexion, extension, and a rotation (pivot) component, making it a highly movable and stressed joint, and perhaps more susceptible to pathologies. Though other joints didn't show any phenotype, it is possible that an injury or stress might induce similar pathologies.

5.1.2 Differences in the phenotype of male and female *Hyal1*-/- mice

Interestingly, adult female mice, had no obvious periosteal bone formation as compared to male mice. A possible explanation for the absence of the phenotype in female mice might be hormonal differences between males and females. Some previous studies have reported that estrogen in females inhibits periosteal bone formation and instead promotes endocortical bone formation while androgens in males stimulate periosteal growth and thus the bone expands towards the periosteum [92, 111]. This is a very interesting finding and might suggest that the phenotype in human females affected with MPS IX, and other MPSs, would be less severe than that in males. To further study the role of sex hormones, similar studies could be conducted in male and female mice that have been subjected to castration and ovarictemies respectively. If hormones are significant contributors to the phenotype, extra bony outgrowths would be expected in adult female *Hyal1*$^{-/-}$ mice in the absence of estrogen and no bony outgrowth in adult male mice with testes removed. However, no sex differences in the skeletal phenotype of the MPSs have been reported, but this should be more fully explored to determine if female MPS patients have reduced or delayed skeletal phenotypes.

5.1.3 Possible role of HA in periosteal bone formation

It has been shown in previous studies that the accumulation of GAGs like dermatan sulphate (DS) and heparin sulphate (HS) in bone impairs osteoclast activity and cartilage

resorption by inhibiting the collagenolytic activity of cathepsin K, ultimately leading to insufficient space for new bone formation and causing skeletal abnormalities [20, 112]. HA is thought to be synthesized in the osteoblasts of the periosteum of the diaphysis on stimulation by parathyroid hormone [83]. Another study also shows that HA inhibits differentiation of osteoclasts via TLR4 receptor by hindering macrophage-colony stimulating factor (M-CSF) signaling which is required for the proliferation and differentiation of osteoclasts and receptor activator of nuclear factor κ B ligand (RANKL) which is necessary for the commitment of osteoclast precursor to osteoclasts [113]. Taken together, we think accumulation of HA in the extracellular matrix of periosteal bone, might be contributing to bone remodeling reactions in the periosteum by inhibiting bone resorption and causing its abnormal growth. Further studies will be needed to assess this possibility.

5.1.4 Bone strength

Bone mineral density and bone microarchitecture are the main determinants of bone strength as they indicate the amount and quality of bone respectively. In the present study, the extra periosteal bone formation in *Hyal1*$^{-/-}$ mice was not accompanied by a significant difference in the density of bone. However, analysis of the microarchitecture of the trabecular bone of one year old mice showed a significant increase in trabecular separation and decrease in trabecular number which was close to significance (p=0.052). Trabecular separation is the thickness of the soft tissues or spaces between the trabecular bone within the trabecular volume of interest. Therefore an increase in trabecular

separation could be indicative of a decrease in the amount of bone. On the other hand trabecular number is the number of bony spicules present per unit length and a decrease in trabecular number also indicates reduction in the amount of bone. Taking together, the bone microarchitecture analysis suggests an active process of trabecular bone erosion but no change in bone mineral density. Further studies would be needed to verify this finding using additional micro-CT controls to validate the thickness of the trabecular bone.

The observed changes in trabecular bone parameters may explain the absence of a significant difference in BMD and TMD, which may have occurred as a result of the occurrence of periosteal apposition and trabecular erosion occurring in parallel to each other. However, there was a trend toward increased BMD in *Hyal1*$^{-/-}$ compared to controls, suggesting that the periosteal apposition was larger when compared to trabecular erosion, and increasing the total number of experimental animals might give significant evidence for this explanation. Also, for each of the parameters calculated in this study, the standard deviation was quite high which indicates a wide range of values for each parameter. This heterogeneity was present in both controls as well as *Hyal1*$^{-/-}$ mice, and small changes could not be detected given our small animal numbers (n=6 for 1 year old, n=6 for 6 months old). Increasing the number of experimental animals for future studies might compensate for the variability between animals. Determining the power of the study will assist in evalutating the sample size, and whether it was sufficient to identify a significant difference if one existed. For example, the power analysis of the metaphysis TRAB BMD of 1 year old animals through manual processing gave a value

of 41% which shows this study had type II error and was underpowered. Increasing the sample size to 16 could increase the power up to 80%.

5.1.5 Comparing the *Hyal1*-/- mice phenotype with the human MPS phenotype

Combining this study with the previous study of joint histology and comparing with the human phenotype, it is clear that *Hyal1*$^{-/-}$ mice do not fully recapitulate the human condition as the joints involved are more diverse in humans, but it does confirm joints as the commonly affected region in MPS IX. The periosteal bone formation appears to take place after the loss of proteoglycan which was detected as early as 3 months of age in *Hyal1*$^{-/-}$ mice. Joint disease typically precedes the formation of osteophytes in other models as well. Both the loss of proteoglycans in the articular cartilage and the formation of osteophytes are features of osteoarthritis. Thus the pathogenesis of MPS IX appears to share many features with osteoarthritis.

Symptomatic skeletal deformities like short stature, acetabular erosions, baker's cyst, facial dysmorphism, nodule formations in the synovium and non-skeletal HA accumulation appear to be absent in the MPS IX mice model. However, it is possible that further studies are needed to identify the synovial findings as these would not be visible by micro-CT and may have been missed in earlier histological studies. Also significant skeletal abnormalities outside of the joints were absent in a second set of MPS IX patients which suggests that symptoms might vary from patient to patient but both the

degeneration of the articular cartilage of the knee, and abnormal periosteum formation in knee joints can be considered as important symptomatic evidence of MPSs.

Compared with other MPS mice models, MPS IX mouse phenotype is very mild which is consistent with the human phenotype. It lacks obvious skeletal abnormalities like spinal stenosis, oar shaped ribs, shortened extremities, thickened bones and hip dysplasia. As shown in previous studies in our lab, this mild phenotype might be the consequence of compensation for hyaluronidase deficiency by β-hexosaminidase and β-glucuronidase[28]. However the periosteal bone formation seen around the knee joints in *Hyal1*$^{-/-}$ mice are similar to those seen in MPS I, MPS II and MPS VII mice. Understanding the mechanisms under which such abnormal bony outgrowths might occur could help in targeted treatments and prevention of many such skeletal deformities. Clearly, studies aimed at identifying additional MPS IX patients should focus on the joint abnormalities.

5.1.6 *Hyal1*-/- mice as an ideal model

As described in Chapter 1, skeletal symptoms are the most common clinical manifestation in most of the MPSs, and they respond poorly to the existing treatments causing significant morbidity to patients, and necessitating a better understanding of its pathogenesis in MPS disorders. General characterization of *Hyal1*$^{-/-}$ mice showed a premature loss of proteoglycans from the articular cartilage of knee joints and no abnormalities in other organ systems. In this study, the use of micro-CT improved our ability to understand changes in bone macro and micro architecture, helping us to

completely define the skeletal perspective of MPS IX. Although there were no significant skeletal differences found in *Hyal*1$^{-/-}$ mice via micro-CT analysis, it showed consistent changes in the joint of the animal in the form of periosteal bone formation near joints. Periosteal bone formations in *Hyal*1$^{-/-}$ mice look similar to an osteochondrophyte, also called as chondro-osteophyte. They are a type of osteophyte arising in the periosteum that lie above the bone near the cartilage and is a common feature of primary [125] osteoarthritis [114]. The origin of chondro-osteophytes is not well understood and may be formed secondarily to joint disease. They occur in many MPS disorders and can involve many different joints; for example disc osteophytes can obstruct airways and lead to breathing problems [115]. The progressive nature from a rough periosteum to periosteal bone formation in our model, may allow us to begin to better understand the process of osteochondrophyte formation. This makes the *Hyal1*$^{-/-}$ mice a well characterized model that could be useful for testing therapies for skeletal abnormalities especially periosteum and joints in all MPSs. Even though this symptom is relatively robust in our model, we believe that adding injury or stress to the joints will further stimulate periosteal bone formation leading to extra bony outgrowths that could impact other joints like the hip, ankle, elbow and shoulders. We also think that the restriction of MPS IX phenotype to the joints makes the MPS IX mouse model attractive for studying the joint manifestations in all MPS disorders as the studies will not be complicated by abnormalities in other organ systems.

5.2 Conclusion & Significance

In conclusion, this thesis advances in our understanding in the area of inherited metabolic disorders with particular focus on skeletal manifestations which are a common but untreatable symptom in many LSDs, especially attenuated types including MPSs. This work extends the results of previous work done in our lab and provides new symptomatic evidence of a skeletal abnormality associated with MPS IX. We could now say that just like osteophyte formation is an integral component of osteoarthritis pathogenesis, periosteal bone formation and cartilage degradation could be an integral component of MPS IX pathogenesis and understanding its biology can give insights in the disturbed homeostasis in MPS IX joints.

Though periosteal bone formation has not been seen in any patients yet, it is possible that the disturbed biochemical homeostasis underlying it might lead to symptoms in the patients in their later years. This finding definitely highlights the importance of the periosteum in the pathogenesis of skeletal abnormalities in MPSs. These findings also indicate that the periosteum may be a good target for drug therapies in the postnatal period. Drugs suppressing the deposition of organic matrix on the periosteum layer that will later get mineralized (periosteal apposition) or maintaining the activity of molecules or enzymes responsible for it may help in maintaining skeletal homeostasis. An increase in periosteal volume and perimeter, coupled with periosteal bone formation and decreased trabecular bone quality strongly suggests a mechanism related to bone modeling in the pathogenesis of MPS IX. Therefore, identifying more

attenuated patients and focusing on the periosteum and bone modeling mechanisms while treating musculoskeletal symptoms in MPSs has the potential to bring promising outcomes.

5.3 Future Directions

Treatments for enzyme deficiencies underlying several LSDs and MPSs are already established or investigations are ongoing. However, the existing treatments have not adequately treated the skeletal symptoms, making this an important area of continued exploration. Although the study of bone and joint manifestations in MPSs has attracted the interest of researchers in recent years [18, 20, 112] the exact mechanism underlying the skeletal abnormalities are mostly unknown and therefore effective treatments for them are still distant. Understanding the pathogenesis behind each clinical symptom can help in finding treatments for such manifestations.

Periosteal bone formation gives further insight into the phenotype of MPS IX plus the mechanism underlying skeletal pathogenesis. A first step would be to validate whether this abnormal outgrowth may be linked to the deficiency of HYAL1. Immunohistochemistry could be done to determine the expression of HYAL1 at the periosteal membrane of knee joints of mice where the abnormal growths are found. Similarly, histology using hyaluronan binding protein (HABP) could be used to demonstrate the accumulation of HA in periosteum region, if any. If HYAL1 plays an important role, it would be expected to be highly expressed at the periosteal membrane in

controls while highly reduced in *Hyal1*$^{-/-}$ mice, and in its absence, HA would be expected to accumulate.

The second obvious step would be to investigate the mechanism underlying periosteal bone formation. The first step towards this would be to analyse the changes in the components of the ECM, and to evaluate the osteoblast and osteoclast number at the periosteal surface. This will also indirectly investigate bone modeling and remodeling mechanisms. This can be done by using bone formation and resorption markers like ALP and TRAP which are specifically expressed in osteoblasts and osteoclasts respectively [116, 117]. In addition, a cysteine protease called cathepsin K which is selectively expressed in active osteoclasts and is responsible for degrading collagen from bones and cartilage can be used to investigate the activity of osteoclasts. As has been suggested for MPS I [112], any loss of collagenolytic activity of cathepsin K can be attributed to accumulation of glycosaminoglycans which can be further evaluated by co-localization studies of cathepsin K with HA [20, 112].

Lastly, this was a cross-sectional study designed to enable quantitative and qualitative assessment of the MPS IX mouse skeleton through micro-CT. In future, a longitudinal study design can also be applied to study skeletal changes within the same animal over the time. Also, if the HYAL1, HABP, ALP and TRAP experiments described above are informative for the knee joints, they could be extended to other joints of the body like hip, spine, tarsal and carpal joins to see if any mechanistic changes could be seen histologically despite the absence of periosteal bone formation. One might also

stress the animals by exercise or injury to determine if this leads to the involvement of other joints.

Once the mechanisms underlying skeletal abnormalities are well defined in HYAL1 deficient mice, they can be used as an ideal model for testing therapies for the skeletal system that will be relevant to all MPSs and other LSDs that show skeletal manifestations.

References

1. Boustany, R.-M. N., Lysosomal storage diseases[mdash]the horizon expands. *Nat Rev Neurol* **2013,** *9* (10), 583-598.
2. Aldenhoven, M.; Sakkers, R. J. B.; Boelens, J.; de Koning, T. J.; Wulffraat, N. M., Musculoskeletal manifestations of lysosomal storage disorders. *Annals of the Rheumatic Diseases* **2009,** *68* (11), 1659-1665.
3. Lampe, C.; Bellettato, C. M.; Karabul, N.; Scarpa, M., Mucopolysaccharidoses and Other Lysosomal Storage Diseases. *Rheumatic Disease Clinics of North America* **2013,** *39* (2), 431-455.
4. Muenzer, J., Overview of the mucopolysaccharidoses. *Rheumatology* **2011,** *50* (suppl 5), v4-v12.
5. Cimaz, R.; La Torre, F., Mucopolysaccharidoses. *Curr Rheumatol Rep* **2013,** *16* (1), 1-9.
6. White, K. K.; Sousa, T., Mucopolysaccharide Disorders in Orthopaedic Surgery. *Journal of the American Academy of Orthopaedic Surgeons* **2013,** *21* (1), 12-22.
7. White, K. K., Orthopaedic aspects of mucopolysaccharidoses. *Rheumatology* **2011,** *50* (suppl 5), v26-v33.
8. Cimaz, R.; Coppa, G.; Kone-Paut, I.; Link, B.; Pastores, G.; Elorduy, M.; Spencer, C.; Thorne, C.; Wulffraat, N.; Manger, B., Joint contractures in the absence of inflammation may indicate mucopolysaccharidosis. *Pediatric Rheumatology* **2009,** *7* (1), 18.
9. Lutsky, K. F.; Tejwani, N. C., Orthopaedic manifestations of Gaucher disease. *Bulletin of the NYU Hospital for Joint Diseases* **2007,** *65*, 37.

10. Noh, H.; Lee, J. I., Current and potential therapeutic strategies for mucopolysaccharidoses. *Journal of Clinical Pharmacy and Therapeutics* **2014,** *39* (3), 215-224.
11. Wynn, R., Stem Cell Transplantation in Inherited Metabolic Disorders. *ASH Education Program Book* **2011,** *2011* (1), 285-291.
12. Evers, M.; Saftig, P.; Schmidt, P.; Hafner, A.; McLoghlin, D. B.; Schmahl, W.; Hess, B.; von Figura, K.; Peters, C., Targeted disruption of the arylsulfatase B gene results in mice resembling the phenotype of mucopolysaccharidosis VI. *Proceedings of the National Academy of Sciences* **1996,** *93* (16), 8214-8219.
13. Rowan, D. J.; Tomatsu, S.; Grubb, J. H.; Montano, A. M.; Sly, W. S., Assessment of bone dysplasia by micro-CT and glycosaminoglycan levels in mouse models for mucopolysaccharidosis type I, IIIA, IVA, and VII. *Journal of Inherited Metabolic Disease* **2013,** *36* (2), 235-246.
14. Garcia, A. R.; Pan, J.; Lamsa, J. C.; Muenzer, J., The characterization of a murine model of mucopolysaccharidosis II (Hunter syndrome). *Journal of Inherited Metabolic Disease* **2007,** *30* (6), 924-934.
15. Clarke, L. A.; Russell, C. S.; Pownall, S.; Warrington, C. L.; Borowski, A.; Dimmick, J. E.; Toone, J.; Jirik, F. R., Murine Mucopolysaccharidosis Type I: Targeted Disruption of the Murine α-l-Iduronidase Gene. *Human Molecular Genetics* **1997,** *6* (4), 503-511.
16. Simonaro, C. M.; Haskins, M. E.; Schuchman, E. H., Articular Chondrocytes from Animals with a Dermatan Sulfate Storage Disease Undergo a High Rate of Apoptosis and Release Nitric Oxide and Inflammatory Cytokines: A Possible Mechanism Underlying Degenerative Joint Disease in the Mucopolysaccharidoses. *Lab Invest* **0000,** *81* (9), 1319-1328.
17. Simonaro, C. M.; D'Angelo, M.; He, X.; Eliyahu, E.; Shtraizent, N.; Haskins, M. E.; Schuchman, E. H., Mechanism of Glycosaminoglycan-Mediated Bone and Joint Disease: Implications for the Mucopolysaccharidoses and Other Connective Tissue Diseases. *The American Journal of Pathology* **2008,** *172* (1), 112-122.

18. Clarke, L. A., Pathogenesis of skeletal and connective tissue involvement in the mucopolysaccharidoses: glycosaminoglycan storage is merely the instigator. *Rheumatology* **2011,** *50* (suppl 5), v13-v18.
19. Li, Z.; Yasuda, Y.; Li, W.; Bogyo, M.; Katz, N.; Gordon, R. E.; Fields, G. B.; Brömme, D., Regulation of Collagenase Activities of Human Cathepsins by Glycosaminoglycans. *Journal of Biological Chemistry* **2004,** *279* (7), 5470-5479.
20. Wilson, S.; Bromme, D., Potential role of cathepsin K in the pathophysiology of mucopolysaccharidoses. *Journal of pediatric rehabilitation medicine* **2010,** *3* (2), 139-46.
21. Triggs-Raine, B.; Salo, T. J.; Zhang, H.; Wicklow, B. A.; Natowicz, M. R., Mutations in HYAL1, a member of a tandemly distributed multigene family encoding disparate hyaluronidase activities, cause a newly described lysosomal disorder, mucopolysaccharidosis IX. *Proceedings of the National Academy of Sciences* **1999,** *96* (11), 6296-6300.
22. Fraser, J. R. E.; Laurent, T. C.; Laurent, U. B. G., Hyaluronan: its nature, distribution, functions and turnover. *Journal of Internal Medicine* **1997,** *242* (1), 27-33.
23. Knudson, C. B.; Knudson, W., Hyaluronan-binding proteins in development, tissue homeostasis, and disease. *The FASEB Journal* **1993,** *7* (13), 1233-41.
24. Natowicz, M. R.; Short, M. P.; Wang, Y.; Dickersin, G. R.; Gebhardt, M. C.; Rosenthal, D. I.; Sims, K. B.; Rosenberg, A. E., Clinical and Biochemical Manifestations of Hyaluronidase Deficiency. *New England Journal of Medicine* **1996,** *335* (14), 1029-1033.
25. Imundo, L.; LeDuc, C.; Guha, S.; Brown, M.; Perino, G.; Gushulak, L.; Triggs-Raine, B.; Chung, W., A complete deficiency of Hyaluronoglucosaminidase 1 (HYAL1) presenting as familial juvenile idiopathic arthritis. *Journal of Inherited Metabolic Disease* **2011,** *34* (5), 1013-1022.
26. Martin, D. C.; Atmuri, V.; Hemming, R. J.; Farley, J.; Mort, J. S.; Byers, S.; Hombach-Klonisch, S.; Stern, R.; Triggs-Raine, B. L., A mouse model of human

mucopolysaccharidosis IX exhibits osteoarthritis. *Human Molecular Genetics* **2008,** *17* (13), 1904-1915.

27. Jadin, L.; Wu, X.; Ding, H.; Frost, G. I.; Onclinx, C.; Triggs-Raine, B.; Flamion, B., Skeletal and hematological anomalies in HYAL2-deficient mice: a second type of mucopolysaccharidosis IX? *The FASEB Journal* **2008,** *22* (12), 4316-4326.
28. Gushulak, L.; Hemming, R.; Martin, D.; Seyrantepe, V.; Pshezhetsky, A.; Triggs-Raine, B., Hyaluronidase 1 and β-Hexosaminidase Have Redundant Functions in Hyaluronan and Chondroitin Sulfate Degradation. *Journal of Biological Chemistry* **2012,** *287* (20), 16689-16697.
29. Atmuri, V.; Martin, D. C.; Hemming, R.; Gutsol, A.; Byers, S.; Sahebjam, S.; Thliveris, J. A.; Mort, J. S.; Carmona, E.; Anderson, J. E.; Dakshinamurti, S.; Triggs-Raine, B., Hyaluronidase 3 (HYAL3) knockout mice do not display evidence of hyaluronan accumulation. *Matrix Biology* **2008,** *27* (8), 653-660.
30. Clarke, L. A., The mucopolysaccharidoses: a success of molecular medicine. *Expert Reviews in Molecular Medicine* **2008,** *10*, null-null.
31. Gandhi, N. S.; Mancera, R. L., The Structure of Glycosaminoglycans and their Interactions with Proteins. *Chemical Biology & Drug Design* **2008,** *72* (6), 455-482.
32. Varki, A., *Essentials of glycobiology*. Cold Spring Harbor Laboratory Press: Cold Spring Harbor, N.Y., 2009.
33. Necas, J.; Bartosikova, L.; Brauner, P.; Kolar, J., Hyaluronic acid (hyaluronan): a review. *Veterinarni Medicina* **2008,** *53* (8), 397-411.
34. Volpi, N.; Schiller, J.; Stern, R.; Soltes, L., Role, Metabolism, Chemical Modifications and Applications of Hyaluronan. *Current Medicinal Chemistry* **2009,** *16* (14), 1718-1745.
35. Rodgers, L. S.; Lalani, S.; Hardy, K. M.; Xiang, X.; Broka, D.; Antin, P. B.; Camenisch, T. D., Depolymerized Hyaluronan Induces Vascular Endothelial Growth Factor, a Negative Regulator of Developmental Epithelial-to-Mesenchymal Transformation. *Circulation Research* **2006,** *99* (6), 583-589.

36. Hascall, V. C.; Majors, A. K.; de la Motte, C. A.; Evanko, S. P.; Wang, A.; Drazba, J. A.; Strong, S. A.; Wight, T. N., Intracellular hyaluronan: a new frontier for inflammation? *Biochimica et Biophysica Acta (BBA) - General Subjects* **2004,** *1673* (1–2), 3-12.

37. Kobayashi, N.; Miyoshi, S.; Mikami, T.; Koyama, H.; Kitazawa, M.; Takeoka, M.; Sano, K.; Amano, J.; Isogai, Z.; Niida, S.; Oguri, K.; Okayama, M.; McDonald, J. A.; Kimata, K.; Taniguchi, S. i.; Itano, N., Hyaluronan Deficiency in Tumor Stroma Impairs Macrophage Trafficking and Tumor Neovascularization. *Cancer Research* **2010,** *70* (18), 7073-7083.

38. Camenisch, T. D.; Spicer, A. P.; Brehm-Gibson, T.; Biesterfeldt, J.; Augustine, M. L.; Calabro, A., Jr.; Kubalak, S.; Klewer, S. E.; McDonald, J. A., Disruption of hyaluronan synthase-2 abrogates normal cardiac morphogenesis and hyaluronan-mediated transformation of epithelium to mesenchyme. *The Journal of Clinical Investigation* **2000,** *106* (3), 349-360.

39. Bai, K.-J.; Spicer, A. P.; Mascarenhas, M. M.; Yu, L.; Ochoa, C. D.; Garg, H. G.; Quinn, D. A., The Role of Hyaluronan Synthase 3 in Ventilator-induced Lung Injury. *American Journal of Respiratory and Critical Care Medicine* **2005,** *172* (1), 92-98.

40. Arranz, A. M.; Perkins, K. L.; Irie, F.; Lewis, D. P.; Hrabe, J.; Xiao, F.; Itano, N.; Kimata, K.; Hrabetova, S.; Yamaguchi, Y., Hyaluronan Deficiency Due to Has3 Knock-Out Causes Altered Neuronal Activity and Seizures via Reduction in Brain Extracellular Space. *The Journal of Neuroscience* **2014,** *34* (18), 6164-6176.

41. Stern, R.; Jedrzejas, M. J., Hyaluronidases: Their Genomics, Structures, and Mechanisms of Action. *Chemical Reviews* **2006,** *106* (3), 818-839.

42. Kim, E.; Baba, D.; Kimura, M.; Yamashita, M.; Kashiwabara, S.-i.; Baba, T., Identification of a hyaluronidase, Hyal5, involved in penetration of mouse sperm through cumulus mass. *Proceedings of the National Academy of Sciences of the United States of America* **2005,** *102* (50), 18028-18033.

43. Csoka, A. B.; Frost, G. I.; Stern, R., The six hyaluronidase-like genes in the human and mouse genomes. *Matrix Biology* **2001,** *20* (8), 499-508.

44. Frost, G. I.; Csóka, T. B.; Wong, T.; Stern, R., Purification, Cloning, and Expression of Human Plasma Hyaluronidase. *Biochemical and Biophysical Research Communications* **1997,** *236* (1), 10-15.

45. Rai, S. K.; Duh, F.-M.; Vigdorovich, V.; Danilkovitch-Miagkova, A.; Lerman, M. I.; Miller, A. D., Candidate tumor suppressor HYAL2 is a glycosylphosphatidylinositol (GPI)-anchored cell-surface receptor for jaagsiekte sheep retrovirus, the envelope protein of which mediates oncogenic transformation. *Proceedings of the National Academy of Sciences* **2001,** *98* (8), 4443-4448.

46. Vigdorovich, V.; Miller, A. D.; Strong, R. K., Ability of Hyaluronidase 2 To Degrade Extracellular Hyaluronan Is Not Required for Its Function as a Receptor for Jaagsiekte Sheep Retrovirus. *Journal of Virology* **2007,** *81* (7), 3124-3129.

47. Lepperdinger, G.; Müllegger, J.; Kreil, G., Hyal2 — less active, but more versatile? *Matrix Biology* **2001,** *20* (8), 509-514.

48. Chowdhury, B.; Hemming, R.; Hombach-Klonisch, S.; Flamion, B.; Triggs-Raine, B., Murine Hyaluronidase 2 Deficiency Results in Extracellular Hyaluronan Accumulation and Severe Cardiopulmonary Dysfunction. *Journal of Biological Chemistry* **2013,** *288* (1), 520-528.

49. Hemming, R.; Martin, D. C.; Slominski, E.; Nagy, J. I.; Halayko, A. J.; Pind, S.; Triggs-Raine, B., Mouse Hyal3 encodes a 45- to 56-kDa glycoprotein whose overexpression increases hyaluronidase 1 activity in cultured cells. *Glycobiology* **2008,** *18* (4), 280-289.

50. Myles, D. G.; Primakoff, P., Why did the sperm cross the cumulus? To get to the oocyte. Functions of the sperm surface proteins PH-20 and fertilin in arriving at, and fusing with, the egg. *Biology of Reproduction* **1997,** *56* (2), 320-327.

51. Lin, Y.; Mahan, K.; Lathrop, W. F.; Myles, D. G.; Primakoff, P., A hyaluronidase activity of the sperm plasma membrane protein PH-20 enables sperm to penetrate the cumulus cell layer surrounding the egg. *The Journal of Cell Biology* **1994,** *125* (5), 1157-1163.

52. Baba, D.; Kashiwabara, S.-i.; Honda, A.; Yamagata, K.; Wu, Q.; Ikawa, M.; Okabe, M.; Baba, T., Mouse Sperm Lacking Cell Surface Hyaluronidase PH-20 Can Pass

through the Layer of Cumulus Cells and Fertilize the Egg. *Journal of Biological Chemistry* **2002,** *277* (33), 30310-30314.

53. Chatel, A.; Hemming, R.; Hobert, J.; Natowicz, M. R.; Triggs-Raine, B.; Merz, D. C., The C. elegans hyaluronidase: A developmentally significant enzyme with chondroitin-degrading activity at both acidic and neutral pH. *Matrix Biology* **2010,** *29* (6), 494-502.
54. Kaneiwa, T.; Mizumoto, S.; Sugahara, K.; Yamada, S., Identification of human hyaluronidase-4 as a novel chondroitin sulfate hydrolase that preferentially cleaves the galactosaminidic linkage in the trisulfated tetrasaccharide sequence. *Glycobiology* **2010,** *20* (3), 300-309.
55. Longas, M. O.; Meyer, K., Sequential hydrolysis of hyaluronate by beta-glucuronidase and beta-n-acetylhexosaminidase. *Biochemical Journal* **1981,** *197* (2), 275-282.
56. Sango, K.; McDonald, M. P.; Crawley, J. N.; Mack, M. L.; Tifft, C. J.; Skop, E.; Starr, C. M.; Hoffmann, A.; Sandhoff, K.; Suzuki, K.; Proia, R. L., Mice lacking both subunits of lysosomal [beta]-hexosaminidase display gangliosidosis and mucopolysaccharidosis. *Nat Genet* **1996,** *14* (3), 348-352.
57. Suzuki, K.; Sango, K.; Proia, R. L.; Langaman, C., Mice deficient in all forms of lysosomal beta-hexosaminidase show mucopolysaccharidosis-like pathology. *Journal of Neuropathology and Experimental Neurology* **1997,** *56* (6), 693-703.
58. Vogler, C.; Birkenmeier, E. H.; Sly, W. S.; Levy, B.; Pegors, C.; Kyle, J. W.; Beamer, W. G., a murine model of mucopolysaccharidosis-vii - gross and microscopic findings in beta-glucuronidase-deficient mice. *American Journal of Pathology* **1990,** *136* (1), 207-217.
59. Zhou, B.; Weigel, J. A.; Fauss, L.; Weigel, P. H., Identification of the Hyaluronan Receptor for Endocytosis (HARE). *Journal of Biological Chemistry* **2000,** *275* (48), 37733-37741.
60. Prevo, R.; Banerji, S.; Ferguson, D. J. P.; Clasper, S.; Jackson, D. G., Mouse LYVE-1 Is an Endocytic Receptor for Hyaluronan in Lymphatic Endothelium. *Journal of Biological Chemistry* **2001,** *276* (22), 19420-19430.

61. Isacke, C. M.; Yarwood, H., The hyaluronan receptor, CD44. *The International Journal of Biochemistry & Cell Biology* **2002,** *34* (7), 718-721.

62. UNDERHILL, C., CD44: The hyaluronan receptor. *Journal of Cell Science* **1992,** *103* (2), 293-298.

63. Culty, M.; Nguyen, H. A.; Underhill, C. B., the hyaluronan receptor (cd44) participates in the uptake and degradation of hyaluronan. *Journal of Cell Biology* **1992,** *116* (4), 1055-1062.

64. Schmits, R.; Filmus, J.; Gerwin, N.; Senaldi, G.; Kiefer, F.; Kundig, T.; Wakeham, A.; Shahinian, A.; Catzavelos, C.; Rak, J.; Furlonger, C.; Zakarian, A.; Simard, J. J. L.; Ohashi, P. S.; Paige, C. J.; Gutierrez-Ramos, J. C.; Mak, T. W., *CD44 Regulates Hematopoietic Progenitor Distribution, Granuloma Formation, and Tumorigenicity*. 1997; Vol. 90, p 2217-2233.

65. Gordon, E. J.; Gale, N. W.; Harvey, N. L., Expression of the hyaluronan receptor LYVE-1 is not restricted to the lymphatic vasculature; LYVE-1 is also expressed on embryonic blood vessels. *Developmental Dynamics* **2008,** *237* (7), 1901-1909.

66. Jackson, D. G., The Lymphatics Revisited: New Perspectives from the Hyaluronan Receptor LYVE-1. *Trends in Cardiovascular Medicine* **2003,** *13* (1), 1-7.

67. Gale, N. W.; Prevo, R.; Espinosa, J.; Ferguson, D. J.; Dominguez, M. G.; Yancopoulos, G. D.; Thurston, G.; Jackson, D. G., Normal Lymphatic Development and Function in Mice Deficient for the Lymphatic Hyaluronan Receptor LYVE-1. *Molecular and Cellular Biology* **2007,** *27* (2), 595-604.

68. Pandey, M. S.; Weigel, P. H., Hyaluronic Acid Receptor for Endocytosis (HARE)-mediated Endocytosis of Hyaluronan, Heparin, Dermatan Sulfate, and Acetylated Low Density Lipoprotein (AcLDL), but Not Chondroitin Sulfate Types A, C, D, or E, Activates NF-κB-regulated Gene Expression. *Journal of Biological Chemistry* **2014,** *289* (3), 1756-1767.

69. Stern, R., Devising a pathway for hyaluronan catabolism: are we there yet? *Glycobiology* **2003,** *13* (12), 105R-115R.

70. Kiani, C.; Chen, L.; Wu, Y. J.; Yee, A. J.; Yang, B. B., Structure and function of aggrecan. *Cell Res* **2002,** *12* (1), 19-32.

71. Holmes, M. W. A.; Bayliss, M. T.; Muir, H., Hyaluronic-acid in human articular-cartilage - age-related-changes in content and size. *Biochemical Journal* **1988,** *250* (2), 435-441.

72. Hiscock, D. R. R.; Caterson, B.; Flannery, C. R., Expression of hyaluronan synthases in articular cartilage. *Osteoarthritis and Cartilage* **2000,** *8* (2), 120-126.

73. Recklies, A. D.; White, C.; Melching, L.; Roughley, P. J., Differential regulation and expression of hyaluronan synthases in human articular chondrocytes, synovial cells and osteosarcoma cells. *Biochemical Journal* **2001,** *354*, 17-24.

74. Flannery, C. R.; Little, C. B.; Hughes, C. E.; Caterson, B., Expression and Activity of Articular Cartilage Hyaluronidases. *Biochemical and Biophysical Research Communications* **1998,** *251* (3), 824-829.

75. Hua, Q.; Knudson, C. B.; Knudson, W., Internalization of hyaluronan by chondrocytes occurs via receptor-mediated endocytosis. *Journal of Cell Science* **1993,** *106* (1), 365-375.

76. Knudson, C. B.; Knudson, W., Hyaluronan and CD44 - Modulators of chondrocyte metabolism. *Clinical Orthopaedics and Related Research* **2004,** (427), S152-S162.

77. Knudson, W.; Chow, G.; Knudson, C. B., CD44-mediated uptake and degradation of hyaluronan. *Matrix Biology* **2002,** *21* (1), 15-23.

78. Embry, J. J.; Knudson, W., G1 domain of aggrecan cointernalizes with hyaluronan via a CD44-mediated mechanism in bovine articular chondrocytes. *Arthritis & Rheumatism* **2003,** *48* (12), 3431-3441.

79. Morales, T. I.; Hascall, V. C., Correlated metabolism of proteoglycans and hyaluronic acid in bovine cartilage organ cultures. *Journal of Biological Chemistry* **1988,** *263* (8), 3632-3638.

80. Prince, C., Roles of hyaluronan in bone resorption. *BMC Musculoskeletal Disorders* **2004,** *5* (1), 12.

81. Bastow, E. R.; Byers, S.; Golub, S. B.; Clarkin, C. E.; Pitsillides, A. A.; Fosang, A. J., Hyaluronan synthesis and degradation in cartilage and bone. *Cellular and Molecular Life Sciences* **2008,** *65* (3), 395-413.

82. Boskey, A. L.; Dick, B. L., Hyaluronan interactions with Hydroxyapatite do not Alter In Vitro Hydroxyapatite Crystal Proliferation and Growth. *Matrix* **1991,** *11* (6), 442-446.

83. Midura, R. J.; Su, X.; Morcuende, J. A.; Tammi, M.; Tammi, R., Parathyroid Hormone Rapidly Stimulates Hyaluronan Synthesis by Periosteal Osteoblasts in the Tibial Diaphysis of the Growing Rat. *Journal of Biological Chemistry* **2003,** *278* (51), 51462-51468.

84. Adams, J. R. J.; Sander, G.; Byers, S., Expression of hyaluronan synthases and hyaluronidases in the MG63 osteoblast cell line. *Matrix Biology* **2006,** *25* (1), 40-46.

85. Clarke, B., Normal Bone Anatomy and Physiology. *Clinical Journal of the American Society of Nephrology* **2008,** *3* (Supplement 3), S131-S139.

86. Boyle, W. J.; Simonet, W. S.; Lacey, D. L., Osteoclast differentiation and activation. *Nature* **2003,** *423* (6937), 337-342.

87. Horiuchi, K.; Amizuka, N.; Takeshita, S.; Takamatsu, H.; Katsuura, M.; Ozawa, H.; Toyama, Y.; Bonewald, L. F.; Kudo, A., Identification and Characterization of a Novel Protein, Periostin, with Restricted Expression to Periosteum and Periodontal Ligament and Increased Expression by Transforming Growth Factor β. *Journal of Bone and Mineral Research* **1999,** *14* (7), 1239-1249.

88. Bord, S.; Horner, A.; Beavan, S.; Compston, J., Estrogen receptors α and β are differentially expressed in developing human bone. *Journal of Clinical Endocrinology and Metabolism* **2001,** *86* (5), 2309-2314.

89. Chang, H.; Knothe Tate, M. L., Concise Review: The Periosteum: Tapping into a Reservoir of Clinically Useful Progenitor Cells. *Stem Cells Translational Medicine* **2012,** *1* (6), 480-491.

90. Junqueira's Basic Histology Text and Atlas - 13th edition Mescher Anthony L Junqueira's Basic Histology Text and Atlas - 13th edition 544pp + CD-ROM 45.99 McGraw-Hill Professional 978 1 2590 7232 1 1259072320 Formula: see text. *Nursing standard (Royal College of Nursing (Great Britain) : 1987)* **2013,** *28* (16), 34-34.

91. Dwek, J., The periosteum: what is it, where is it, and what mimics it in its absence? *Skeletal Radiol* **2010,** *39* (4), 319-323.
92. Allen, M. R.; Hock, J. M.; Burr, D. B., Periosteum: biology, regulation, and response to osteoporosis therapies. *Bone* **2004,** *35* (5), 1003-1012.
93. Seeman, E., Bone Modeling and Remodeling. **2009,** *19* (3), 219-233.
94. Szulc, P.; Seeman, E., Thinking inside and outside the envelopes of bone. *Osteoporos Int* **2009,** *20* (8), 1281-1288.
95. Knudson, C. B.; Knudson, W., Cartilage proteoglycans. *Seminars in Cell & Developmental Biology* **2001,** *12* (2), 69-78.
96. Tremoleda, J.; Khalil, M.; Gompels, L.; Wylezinska-Arridge, M.; Vincent, T.; Gsell, W., Imaging technologies for preclinical models of bone and joint disorders. *EJNMMI Research* **2011,** *1* (1), 11.
97. Martin, D. C.; Atmuri, V.; Hemming, R. J.; Farley, J.; Mort, J. S.; Byers, S.; Hombach-Klonisch, S.; Csoka, A. B.; Stern, R.; Triggs-Raine, B. L., A mouse model of human mucopolysaccharidosis IX exhibits osteoarthritis (vol 17, pg 1904, 2008). *Human Molecular Genetics* **2008,** *17* (18), 2919-2919.
98. Feldkamp, L. A.; Davis, L. C.; Kress, J. W., Practical cone-beam algorithm. *J. Opt. Soc. Am. A* **1984,** *1* (6), 612-619.
99. Lorensen, W. E.; Cline, H. E., Marching cubes: A high resolution 3D surface construction algorithm. *SIGGRAPH Comput. Graph.* **1987,** *21* (4), 163-169.
100. Kim, Y. J.; Henkin, J., Micro-Computed Tomography Assessment of Human Alveolar Bone: Bone Density and Three-Dimensional Micro-Architecture. *Clinical Implant Dentistry and Related Research* **2013**, n/a-n/a.
101. Lee, J. H.; Chun, K. J.; Kim, H. S.; Kim, S. H.; Han, P.; Jun, Y.; Lim, D., Alteration patterns of trabecular bone microarchitectural characteristics induced by osteoarthritis over time. *Clinical Interventions in Aging* **2012,** *7*, 303-312.
102. Brandi, M. L., Micro architecture, the key to bone quality. *Rheumatology* **2009,** *48*, IV3-IV8.
103. Bouxsein, M. L.; Boyd, S. K.; Christiansen, B. A.; Guldberg, R. E.; Jepsen, K. J.; Müller, R., Guidelines for assessment of bone microstructure in rodents using

micro–computed tomography. *Journal of Bone and Mineral Research* **2010,** *25* (7), 1468-1486.

104. Botter, S. M.; van Osch, G. J. V. M.; Waarsing, J. H.; Day, J. S.; Verhaar, J. A. N.; Pols, H. A. P.; van Leeuwen, J. P. T. M.; Weinans, H., Quantification of subchondral bone changes in a murine osteoarthritis model using micro-CT. *Biorheology* **2006,** *43* (3-4), 379-388.
105. Yang, S.; Hollister, A.; Orchard, E.; Chaudhery, S.; Ostanin, D.; Lokitz, S.; Mathis, J., Quantification of bone changes in a collagen-induced arthritis mouse model by reconstructed three dimensional micro-CT. *Biological Procedures Online* **2013,** *15* (1), 8.
106. Lee, J. H.; Chun, K. J.; Kim, H. S.; Kim, S. H.; Lee, K.-Y.; Kim, D. J.; Lim, D., Changes in microarchitectural characteristics at the tibial epiphysis induced by collagen-induced rheumatoid arthritis over time. *Clinical Interventions in Aging* **2012,** *7*, 373-382.
107. Mohan, G.; Perilli, E.; Kuliwaba, J. S.; Humphries, J. M.; Parkinson, I. H.; Fazzalari, N. L., Application of in vivo micro-computed tomography in the temporal characterisation of subchondral bone architecture in a rat model of low-dose monosodium iodoacetate-induced osteoarthritis. *Arthritis Research & Therapy* **2011,** *13* (6).
108. Kohler, T.; Beyeler, M.; Webster, D.; Muller, R., Compartmental bone morphometry in the mouse femur: Reproducibility and resolution dependence of microtomographic measurements. *Calcified Tissue International* **2005,** *77* (5), 281-290.
109. Seeman, E., The periosteum—a surface for all seasons. *Osteoporos Int* **2007,** *18* (2), 123-128.
110. Altun, B. U. u., Periosteum: Resorption or Formation Area? *Turkish Journal of Endocrinology and Metabolism* **2008**.
111. Seeman, E., Periosteal Bone Formation — A Neglected Determinant of Bone Strength. *New England Journal of Medicine* **2003,** *349* (4), 320-323.

112. Wilson, S.; Hashamiyan, S.; Clarke, L.; Saftig, P.; Mort, J.; Dejica, V. M.; Brömme, D., Glycosaminoglycan-Mediated Loss of Cathepsin K Collagenolytic Activity in MPS I Contributes to Osteoclast and Growth Plate Abnormalities. *The American Journal of Pathology* **2009,** *175* (5), 2053-2062.

113. Chang, E.-J.; Kim, H. J.; Ha, J.; Kim, H. J.; Ryu, J.; Park, K.-H.; Kim, U.-H.; Lee, Z. H.; Kim, H.-M.; Fisher, D. E.; Kim, H.-H., Hyaluronan inhibits osteoclast differentiation via Toll-like receptor 4. *Journal of Cell Science* **2007,** *120* (1), 166-176.

114. van der Kraan, P. M.; van den Berg, W. B., Osteophytes: relevance and biology. *Osteoarthritis and Cartilage* **2007,** *15* (3), 237-244.

115. Borlot, F.; Arantes, P. R.; Quaio, C. R.; da Silva Franco, J. F.; Lourenço, C. M.; Bertola, D. R.; Kim, C. A., New insights in mucopolysaccharidosis type VI: Neurological perspective. *Brain and Development 36* (7), 585-592.

116. Liu, H.; Feng, W.; Yimin; Cui, J.; Lv, S.; Hasegawa, T.; Sun, B.; Li, J.; Oda, K.; Amizuka, N.; Li, M., Histological Evidence of Increased Osteoclast Cell Number and Asymmetric Bone Resorption Activity in the Tibiae of Interleukin-6-Deficient Mice. *Journal of Histochemistry & Cytochemistry* **2014,** *62* (8), 556-564.

117. Power, J.; Loveridge, N.; Rushton, N.; Parker, M.; Reeve, J., Evidence for bone formation on the external "periosteal" surface of the femoral neck: a comparison of intracapsular hip fracture cases and controls. *Osteoporos Int* **2003,** *14* (2), 141-145.

118. Tolar, J.; Grewal, S. S.; Bjoraker, K. J.; Whitley, C. B., Shapiro, E. G.; Charnas, L; Orchard, P. J., Combination of enzyme replacement and hematopoietic stem cell transplantation as therapy for Hurler syndrome. *Bone Marrow Transplant* **2007**, *41*, 531-535.

119. Sillence, D.; Waters, K.; Donaldson, S.; Shaw, P. J.; Ellaway, C., Combined enzyme replacement therapy and hematopoietic stem cell transplantation in mucopolysaccharidosis Type VI. *JIMD Reports-Case and Research Reports* **2012,** 103-106.

120. Valayannopoulos, V.; Wijburg, F. A., Therapy for the mucopolysaccharidoses. *Rheumatology* **2011**, *50*, 49-59.

121. Hounsfield, G. N., Computerized transverse axial scanning (tomography).1. Description of system. *British Journal of Radiology* **1973,** *46*, 1016-1022.

122. Elliott, J. C.; Dover, S. D., X-ray microtomography. *Journal of Microscopy* **1982,** *126***,** 211-213.

123. Neugebauer, V.; Han, J.; Adwanikar, H.; Fu, Y.; Ji, G., Techniques for assessing knee joint pain in arthritis. *Molecular Pain* **2007,** *3*, 8.

124. Fang, H.; Beier, F., Mouse models of osteoarthritis: modelling risk factors and assessing outcomes. *Nat Rev Rheumatol* **2014,** *10*, 413-421.

125. Lim, Y. W.; van Riet, R. P.; Mittal, R.; Bain, G. I., Pattern of osteophyte distribution in primary osteoarthritis of the elbow. *Journal of Shoulder and Elbow Surgery* **2008**, *17*, 963-966.

Appendix A

Images for the selection of VOI from trabecular and cortical bone of femur:

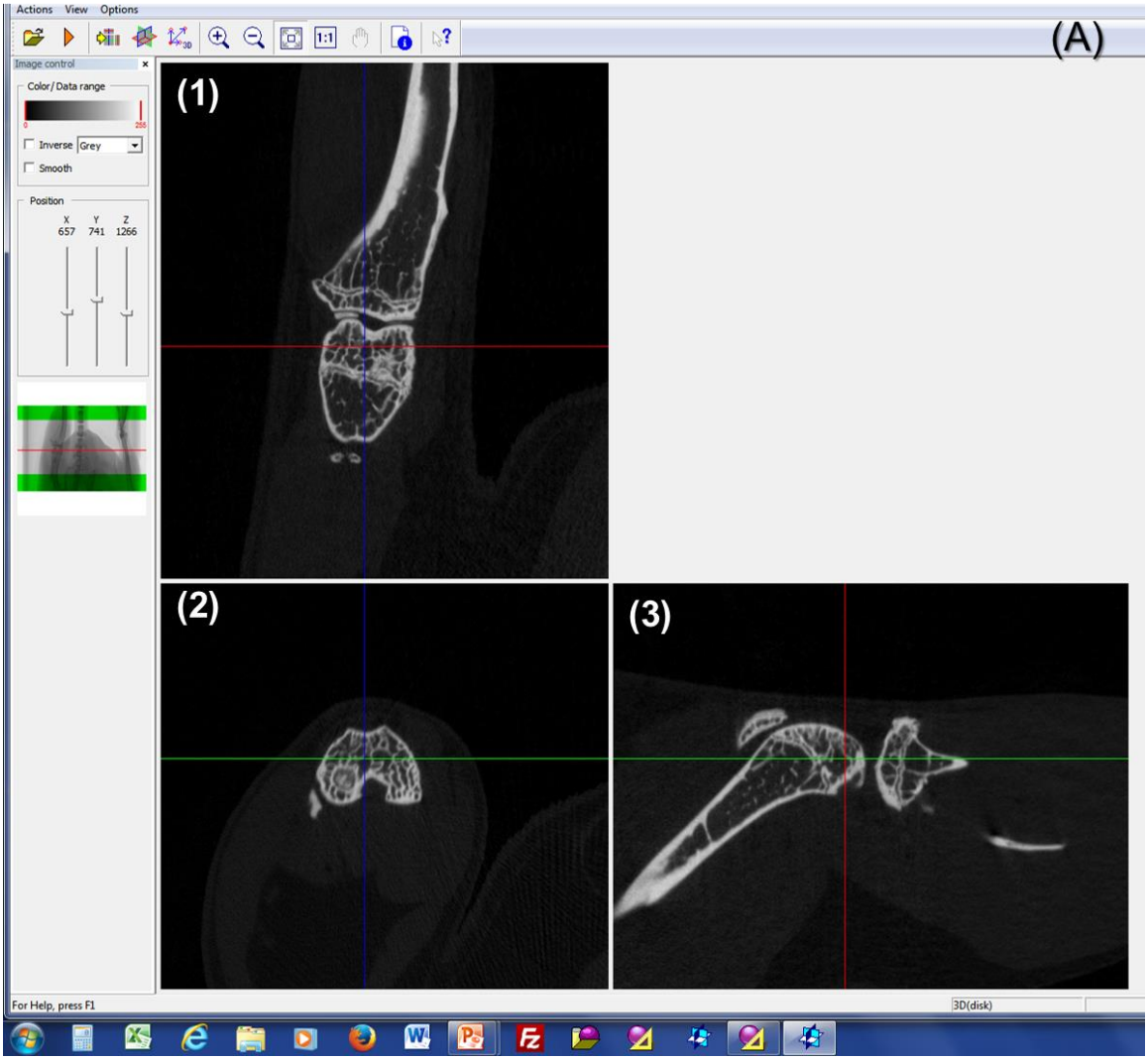

Figure A. Main window of data viewer software: Loaded dataset of the femur shown in (1) coronal (2) transaxial and (3) sagittal planes.

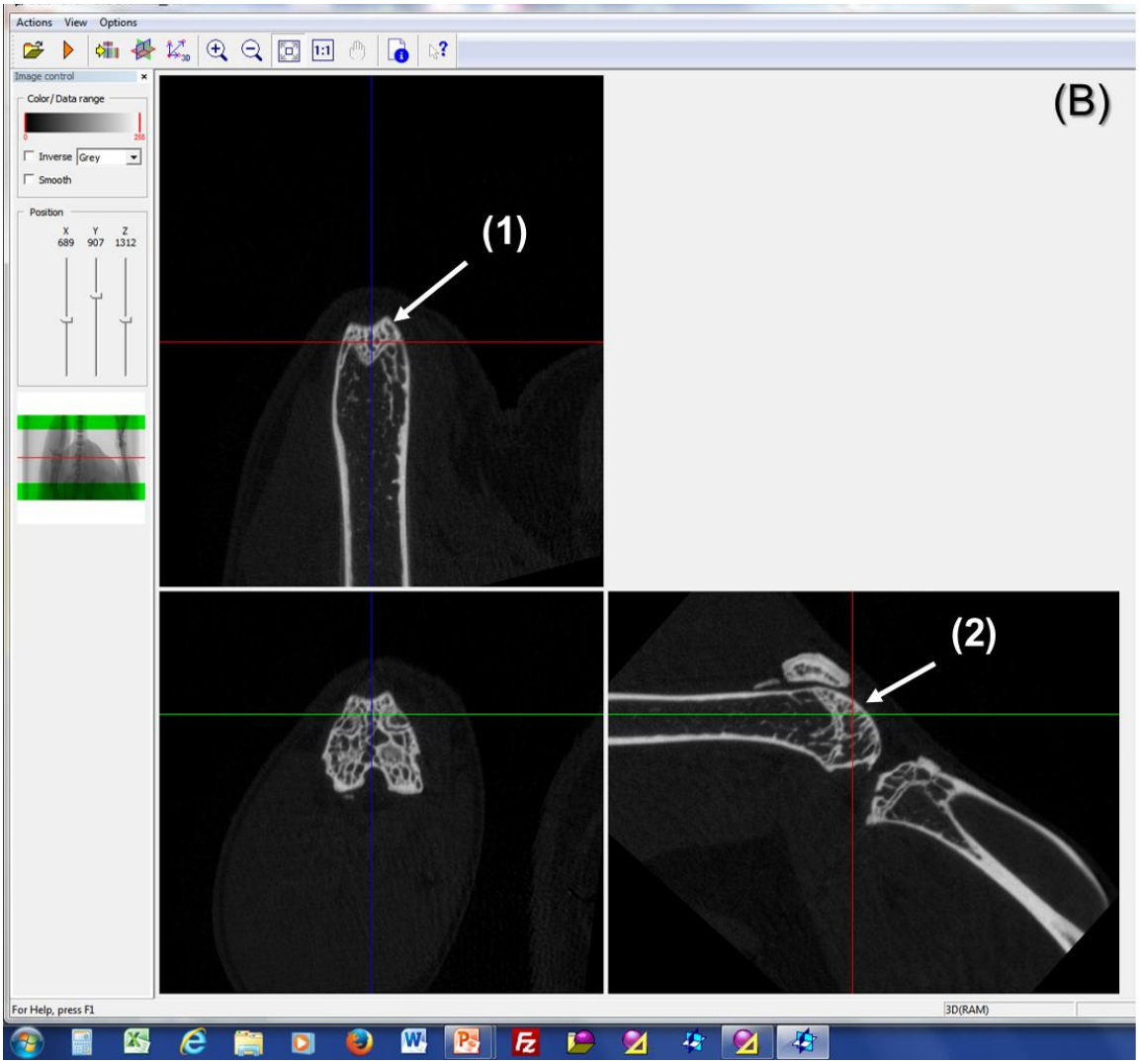

Figure B. Main window of data viewer software: Image of femur after orientation. (1) and (2) show the straightened femur in coronal and sagittal planes. Straightening the image in the coronal and sagittal planes, orients the transaxial mage automatically. After the image is oriented, the straightened transaxial image is saved as a separate dataset in different folder.

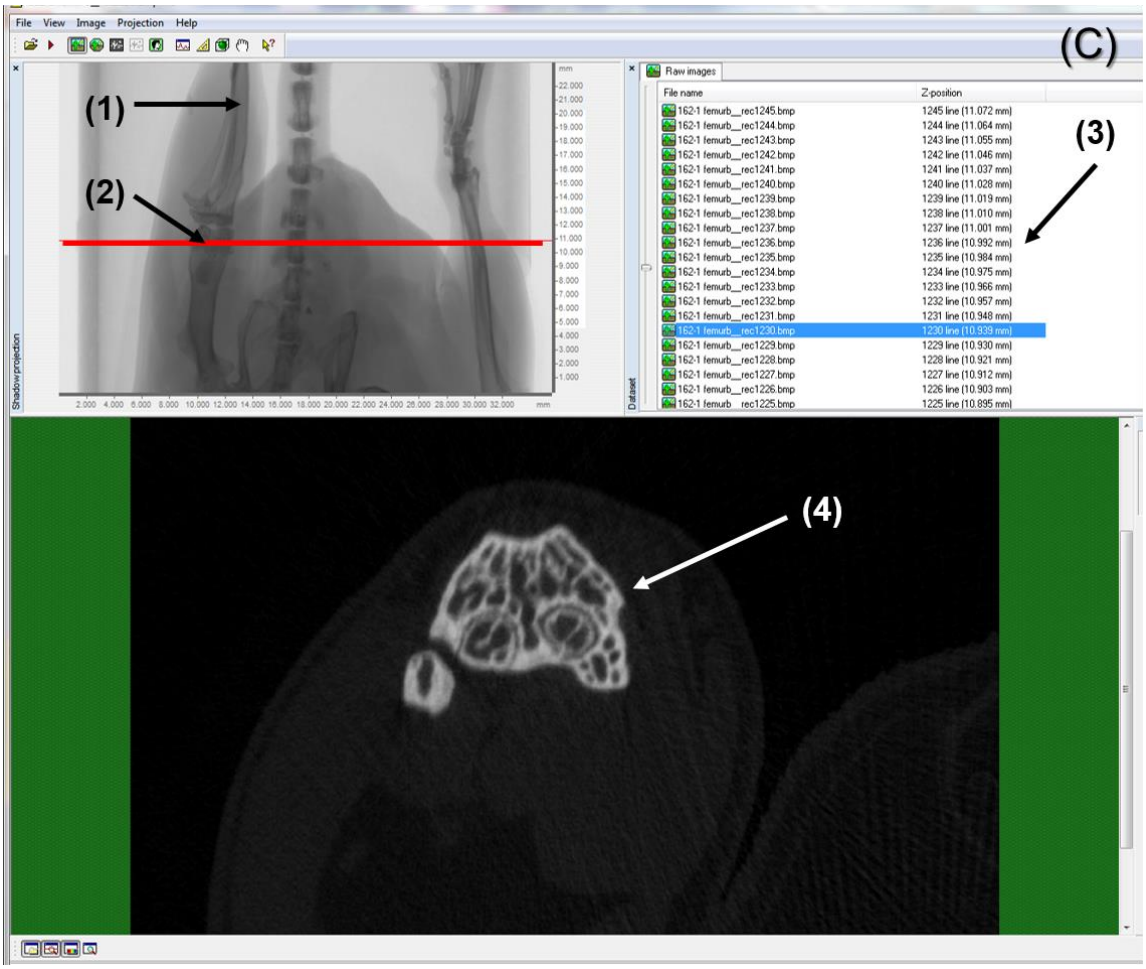

Figure C. Main Window of CT-Analyser software: Oriented image saved from data viewer is then opened in CT-Analyser software for further processing. (1) Shadow projection image, (2) Red line shows the position of the growth plate in the shadow projection image (3) Raw image file, (4) Cross-section image of the growth plate which is identified as reference point.

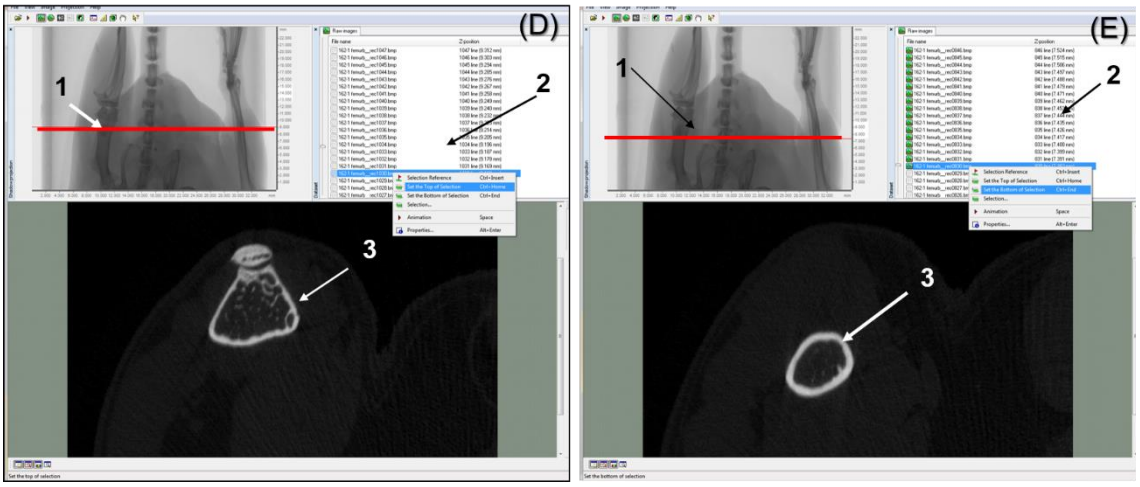

Figure D. Identification of metaphysis for trabecular bone analysis: (1) Red line shows the slice in metaphysis region of femur from where the VOI for trabecular bone begins, (2) The selection of this slice in the raw file image, (3) Cross section of the slice from metaphysis region. **Figure E. Identification of diaphysis for cortical bone analysis:** (1) Red line shows the slice in diaphysis region of femur from where the VOI for cortical bone begins, (2) The selection of this slice in the raw file image, (3) Cross section of the slice from metaphysis region.

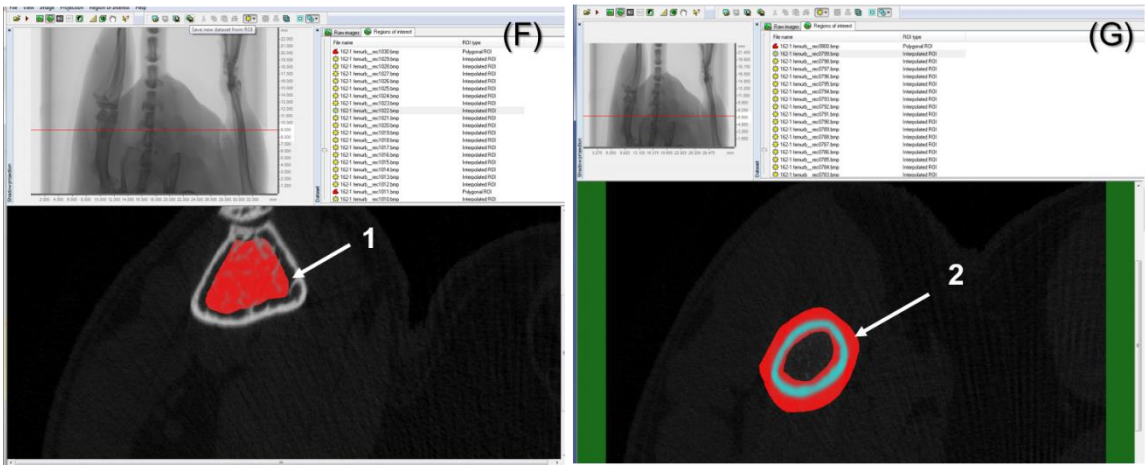

Figure F. Region of interest: (1) Manual drawing of region of interest (ROI) for trabecular bone in the metaphysis region of femur. **Figure G**. (2) Manual drawing of region of interest (ROI) for cortical bone in the diaphysis region of femur

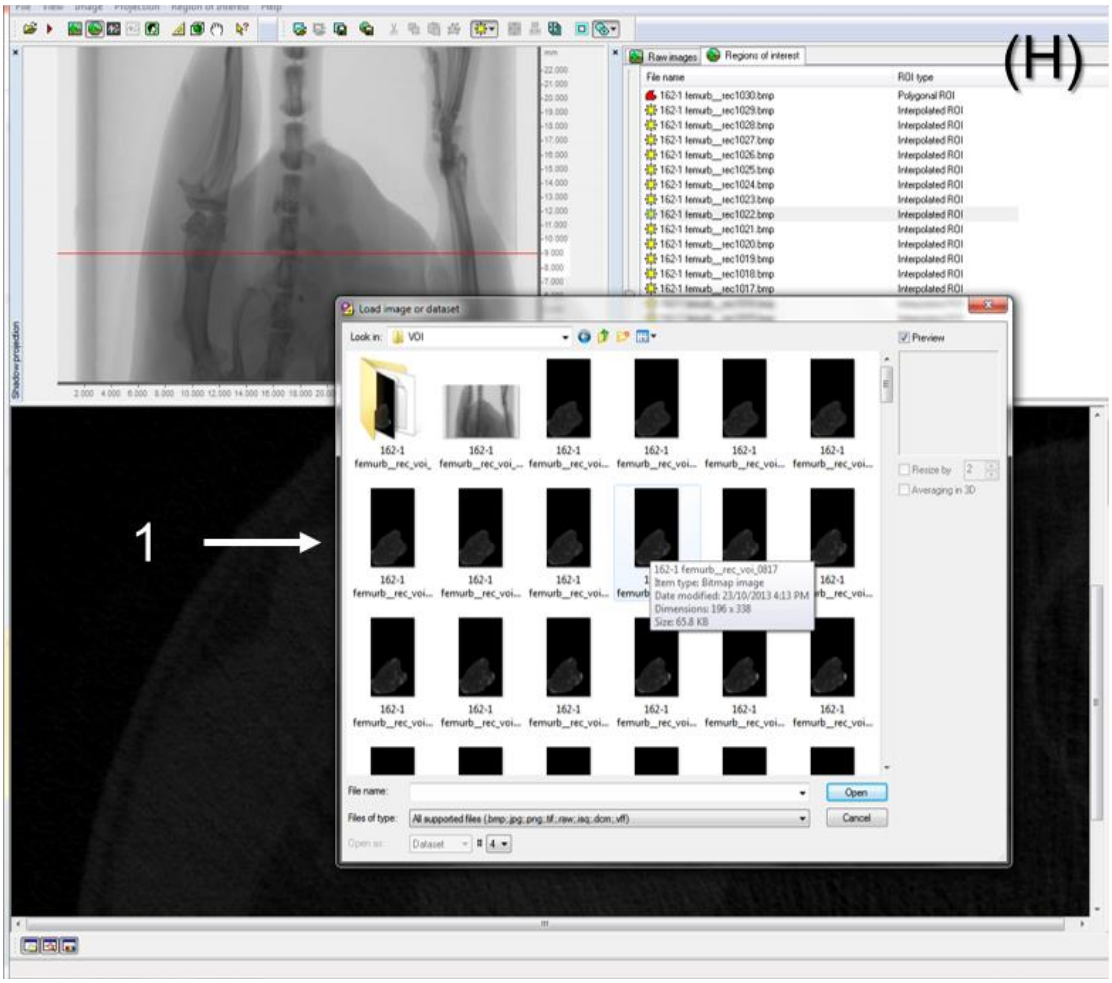

Figure H. Volume of interest: A set of consecutive ROIs together are saved as a dataset that forms a volume of interest from metaphysis region for trabecular bone and from diaphysis for cortical bone. (1) Saving new dataset in a separate folder.

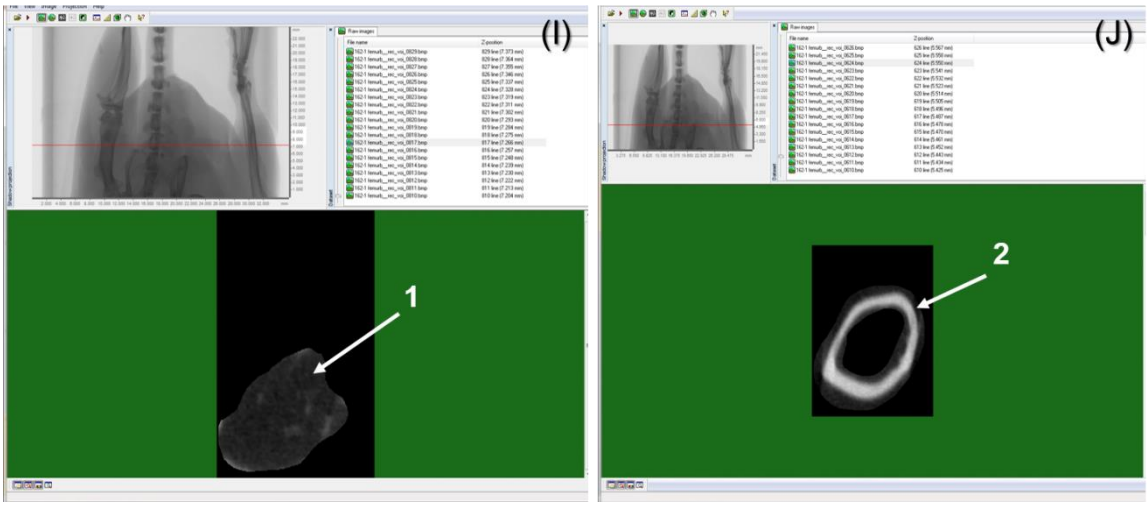

Figure I: New dataset: Opening the new dataset for trabecular bone (1) in the CT-Analyser window. **Figure J**. Opening the new dataset for cortical bone (2) in the CT-Analyser window.

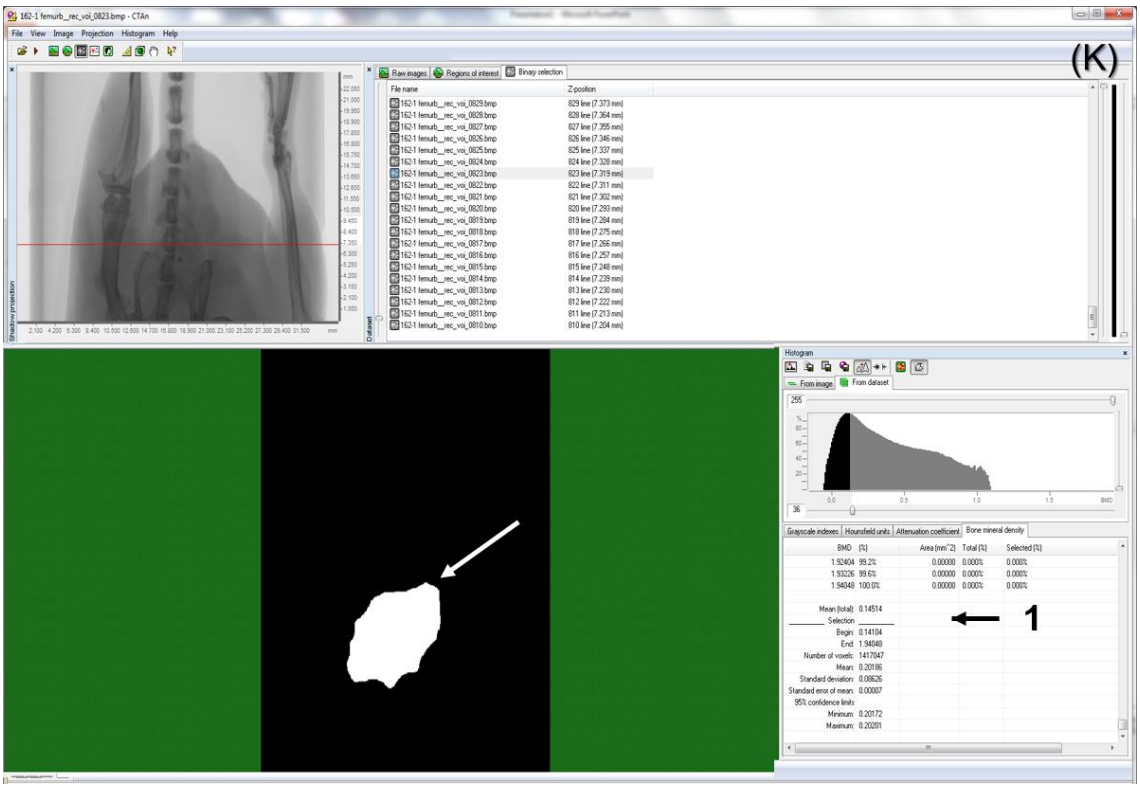

Figure K. Trabecular bone BMD calculation: White arrow shows the non-segmented image of trabecular bone. (1) Display of BMD from the trabecular bone region

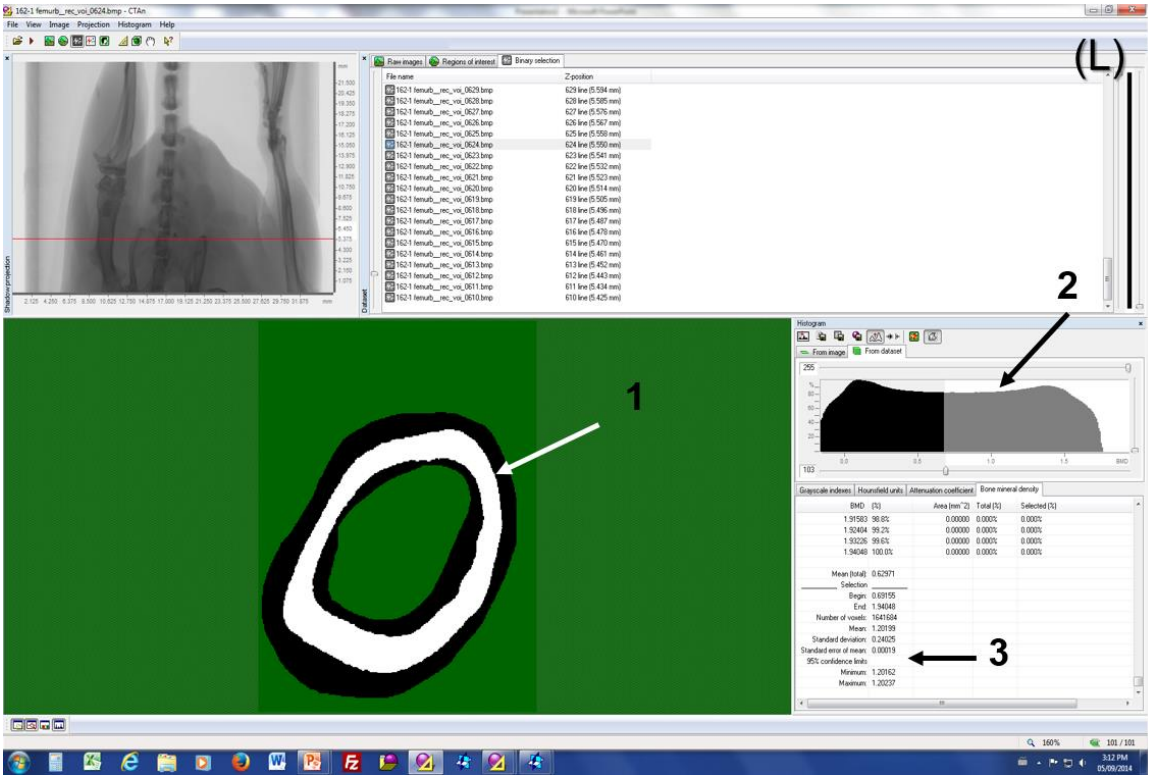

Figure L. Cortical bone BMD calculation: (1) Segmented image of cortical bone where white shows the mineralized bone and black as soft tissue. (2) Graph where the threshold is adjusted manually. Highest value is always kept 255 and lowest value as the one which give best presentation of original cross-sectional image. (3) Display of calculated bone mineral density of cortical bone.